Chapter 4
Rogue Waves in Waters of Infinite and Finite Depths

The most widely investigated rogue wave events are those due to modulational instability or dispersive focusing mechanisms. So far, the nonlinear terms of the equations have been neglected, hence in this chapter attention is paid to rogue wave occurrence when nonlinear effects are taken into account. This chapter—which is mainly devoted to modeling and simulating the physics of rogue wave events in the deep sea—addresses finite depth situations to some extent, too.

First, we present the modulational instability of water waves within the framework of the fully nonlinear equations and weakly nonlinear approximate approach in Sect. 4.1. From a deterministic viewpoint, it is the so-called Benjamin-Feir instability: a carrier wave is unstable in terms of sideband perturbations provided their respective wavenumbers are sufficiently close. From a statistical view point it is known as spectral instability, which is the random version of the Benjamin-Feir instability: a random narrowband wave train is unstable in terms of sideband perturbations provided the width of the spectrum is sufficiently narrow.

The widely-used nonlinear Schrödinger equation and related approximate theory for the Benjamin-Feir instability are presented in Sect. 4.2. Generation of rogue waves due to the nonlinear-dispersive focusing is investigated with the help of the inverse scattering approach. Breathing exact solutions of this model are described.

Section 4.3 is devoted to the occurrence of rogue waves in the deep sea when fully nonlinear equations are used. The High Order Spectral Method (HOSM) and the Boundary Integral Equation Method (BIEM), which are used to simulate numerically rogue waves due to modulational instability and dispersive focusing, are briefly presented with and without wind forcing. Sections 4.2 and 4.3 are devoted to deterministic description of the rogue-wave occurrence, while Sect. 4.4 concerns a statistical description of these giant waves.

Some laboratory experiments on rogue waves are presented in Sect. 4.5 with and without wind action.

Section 4.6 is aimed at presenting 3D aspects of the freak-wave occurrence.

Instrumental registrations of rogue waves give the possibility to fit elaborate theories with natural phenomena. Some approaches to understanding the nature of freak waves are presented in Sect. 4.7.1. They exhibit significant nonlinear (and modulational) effects when rogue waves occur. Results of statistical processing of huge wave in-situ records are collected in Sect. 4.7.2.

C. Kharif et al., *Rogue Waves in the Ocean*, Advances in Geophysical and Environmental Mechanics and Mathematics, DOI 10.1007/978-3-540-88419-4_5,

4.1 The Modulational Instability

The generation of extreme wave events can be simply obtained from the Benjamin-Feir instability (or modulational instability) of uniformly traveling trains of Stokes waves in water of infinite and finite depths. Stokes' wave trains are unstable in terms of various perturbations. Among these instabilities is the Benjamin-Feir instability (a long-wave instability). The latter dominates for small values of the amplitude. Various researchers discovered the existence of modulational instability of Stokes waves at the same time. Lighthill (1965) provided a geometric condition for wave instability in deep water. Later, Benjamin and Feir (1967) demonstrated the result analytically. Using a Hamiltonian approach, Zakharov (1968) derived the same instability result. Furthermore, in the context of modulated water waves, he obtained the famous Nonlinear Schrödinger equation. It would have been more appropriate to call the modulational instability the BFLZ instability instead of BF instability. Benney and Roskes (1969) extended the study to finite depth and derived what is now called the Davey-Stewartson system (Davey and Stewartson 1974). Both Zakharov (1968) and Benney and Roskes (1969), for infinite depth and finite depth, respectively, investigated the stability with 3D perturbations. Dysthe (1979) pursued the perturbation analysis one step further, to fourth-order in wave steepness, and found that the wave-induced mean flow significantly influences the growth rate of the modulational instability. Later on, Stiassnie and Shemer (1984) used a powerful approximate equation—the Zakharov equation free of the narrow band assumption—to investigate the stability of Stokes waves. Note that the Dysthe equation was derived from the Zakharov equation by Stiassnie (1984) under the assumption of narrow band wave field. Furthermore, with the Zakharov equation it is possible to consider perturbations different from modulational type. Later on, numerical computations based on fully nonlinear equations, allowed researchers to go beyond the modulational instability. The main advantage is that there is no restriction on the length of perturbations and amplitude of the basic wave. Longuet-Higgins (1978a,b) investigated 2D instabilities, whereas McLean et al. (1981) and McLean (1982a,b) considered 3D instabilities of 2D Stokes waves. More recently, Francius and Kharif (2006) extended the linear stability analysis of finite-amplitude periodic progressive gravity waves to steeper waves and shallower water. The method used by McLean to study the stability of Stokes wave trains, within the framework of the fully nonlinear equations, is presented in Sect. 4.1.1, followed by a brief presentation of the obtained main results. See the papers by Kharif and Ramamonjiarisoa (1988) and Dias and Kharif (1999), too.

4.1.1 Within the Framework of the Fully Nonlinear Equations

In this section, a general presentation of surface wave instabilities is given, based on the fully nonlinear equations (2.13), (2.28), (2.30), and (2.31). More precisely, we consider the linear stability of a Stokes' wave train of arbitrary wave steepness.

Let $\eta = \bar{\eta} + \eta'$ and $\phi = \bar{\phi} + \phi'$ be the perturbed elevation and perturbed velocity potential, where $(\bar{\eta}, \bar{\phi})$ and (η', ϕ') correspond to the unperturbed Stokes wave (basic wave) and infinitesimal perturbative motion $(\eta' \ll \bar{\eta}, \phi' \ll \bar{\phi})$, respectively. Following Longuet-Higgins (1985), the Stokes wave of wavenumber K_0 is computed iteratively. Substituting these decompositions in the boundary conditions linearized about the unperturbed motion $(\bar{\eta}, \bar{\phi})$, and using the following forms with p and q arbitrary real numbers (see McLean 1982b),

$$\eta' = e^{-i\sigma T} \exp\left[i\left(pK_0X + qK_0Y\right)\right] \sum_{j=-\infty}^{\infty} A_j e^{ijK_0X}, \tag{4.1}$$

$$\phi' = e^{-i\sigma T} \exp\left[i\left(pK_0X + qK_0Y\right)\right] \sum_{j=-\infty}^{\infty} B_j e^{ijK_0X} \frac{\cosh\left[\sqrt{(p+j)^2+q^2}K_0\left(Z+D\right)\right]}{\cosh\left[\sqrt{(p+j)^2+q^2}K_0D\right]}, \tag{4.2}$$

yields a complex eigenvalue problem for σ, with eigenvector $\mathbf{u} = (A_j, B_j)^t$

$$(\mathbf{A} - i\sigma\mathbf{B})\mathbf{u} = 0, \tag{4.3}$$

where $\mathbf{A}$ and $\mathbf{B}$ are complex matrices depending on the wave steepness of the basic wave and the arbitrary real numbers pK_0 and qK_0 corresponding to the longitudinal and transverse wavenumbers of the perturbation, respectively. The physical disturbance that corresponds to the real part of expressions (4.1) and (4.2) has periods $2\pi/pK_0$ and $2\pi/qK_0$ in X- and Y-directions, respectively. The terms corresponding to the sums in (4.1) and (4.2) have the spatial periodicity of the basic Stokes waves. Hence, forms (4.1) and (4.2) express that the perturbations feel the presence of the Stokes waves. Instability corresponds to $\mathrm{Im}(\sigma) \neq 0$. The spectrum is easy to compute when $\bar{\eta}(X,T) = 0$. In the moving frame with the basic wave, one finds that the eigenvalues are

$$\begin{aligned} &\sigma_n = -(p+n)\sqrt{gK_0\tanh\left(K_0D\right)} \pm \sqrt{gK_n\tanh\left(K_nD\right)}, \\ &k_n^2 = (p+n)^2 + q^2, \quad K_n = K_0k_n. \end{aligned} \tag{4.4}$$

The eigenvalues are real, hence the state corresponding to $\bar{\eta} = 0$ is spectrally stable. As the wave steepness of the Stokes wave increases, the eigenvalues move. MacKay and Saffman (1986) derived a necessary condition for a Stokes wave to lose spectral stability corresponding to the collision of eigenvalues of opposite Krein signature (Krein 1955), or a collision of eigenvalues at zero (see MacKay and Saffman 1986).

$$\sigma_{n_1}^{\pm}(p,q) = \sigma_{n_2}^{\pm}(p,q) \tag{4.5}$$

The instabilities are separated into two classes: class I when the collisions occur between modes with $n = m$ and $n = -m$, and class II when the collisions occur between modes with $n = m$ and $n = -m-1$. The corresponding instabilities are

called class I and class II instabilities. Class I (m) corresponds to $(2m+2)$-wave interactions, whereas class II (m) corresponds to $(2m+3)$-wave interactions:
Class I (m)

$$\begin{aligned} &\mathbf{k}_1 = (m+p,q), \quad \mathbf{k}_2 = (m-p,-q), \\ &\sigma_m^+(p,q) = \sigma_{-m}^-(p,q), \\ &\Omega_1 + \Omega_2 = 2m\Omega_0. \end{aligned} \tag{4.6}$$

Class II (m)

$$\begin{aligned} &\mathbf{k}_1 = (m+p,q), \quad \mathbf{k}_2 = (1+m-p,-q), \\ &\sigma_m^+(p,q) = \sigma_{-m-1}^-(p,q), \\ &\Omega_1 + \Omega_2 = (2m+1)\Omega_0, \end{aligned} \tag{4.7}$$

with

$$\begin{aligned} &\Omega_n = \sqrt{gK_n \tanh(K_n D)}, \quad n = 0,1,2, \\ &\mathbf{K}_n = K_0 \mathbf{k}_n, \quad K_n = K_0 k_n, \quad n = 1,2. \end{aligned} \tag{4.8}$$

The collision of eigenvalues may be interpreted as wave-wave resonant interactions satisfying the following conditions

$$\mathbf{K}_1 + \mathbf{K}_2 = N\mathbf{K}_0, \quad \Omega_1 + \Omega_2 = N\Omega_0, \quad N \geq 2, \tag{4.9}$$

where even values of $N(=2m)$ correspond to Class I (m), and odd values of $N(=2m+1)$ correspond to Class II (m), respectively.

Class I (m) instabilities correspond to resonant interactions between the basic mode $\mathbf{K}_0 = (1,0)K_0$ counted $2m$ times and the satellites $\mathbf{K}_1 = (m+p,q)K_0$ and $\mathbf{K}_2 = (m-p,-q)K_0$, whereas class II ($m$) instabilities correspond to resonant interactions between the basic mode $\mathbf{K}_0 = (1,0)K_0$ counted $2m+1$ times and two satellites $\mathbf{K}_1 = (m+p,q)K_0$, $\mathbf{K}_2 = (1+m-p,-q)K_0$. For instance, $N=2$ corresponds to quartet resonant interactions, and $N=3$ responds to quintet resonant interactions, etc.

The BF instability belongs to class I instability with $m=1$ and corresponds to small values of the wavenumber p. Class I ($m=1$) generalizes the BF instability and includes modulational instabilities.

In water of infinite depth ($K_0 D \to \infty$), the 2D ($q=0$) modulational instability is dominant for small to moderate values of the wave steepness, whereas for larger values, 3D instabilities of class II ($m=1$) become dominant. The latter instability may lead to the formation of horseshoe patterns while modulational instability evolves into a series of modulation-demodulation cycles (Fermi-Pasta-Ulam recurrence).

In finite depth, McLean (1982b) considered three depths—one greater ($K_0 D = 2$) and two smaller ($K_0 D = 1$ and 0.5) than $K_0 D = 1.363$, which is a critical depth (see the next section). He confirmed the stabilization of 2D long-wave perturbations ($p \ll 1$) for $K_0 D < 1.363$ as predicted by Whitham (1967). For $K_0 D = 2$, he found

that the dominant instability still belongs to class I ($m = 1$) when the wave steepness is small or moderate. Unlike the deep water case, the modulational instability is now 3D ($q \neq 0$). For steeper waves, 3D instabilities of class II ($m = 1$) crescent-shaped form become dominant. For $K_0D = 1$, 2D long-wave perturbations ($p \ll 1$) of class I ($m = 1$) are stable for small wave steepness. However, this class is dominated by 3D unstable perturbations ($q \neq 0$). For steeper waves, it is the crescent-shaped instability of class II ($m = 1$) that is dominant. The shallowest case ($K_0D = 0.5$) that McLean considered is most unstable for small wave steepness, to a 2D perturbation of class I ($m = 1$) with a wavenumber comparable to K_0, in contrast to the familiar 2D long-wave perturbations that are the dominant instabilities in deep water. For small-amplitude waves, this result was rediscovered by Francius and Kharif (2006) for $K_0D < 0.5$. Two-dimensional long-wave perturbations are stable at these depths. For moderate steepness, the dominant instability shifts to the 3D one and is still associated with class I ($m = 1$). For sufficiently steep waves, class II ($m = 1$) dominates and the most unstable perturbation is three-dimensional.

4.1.2 Within the Framework of the Nonlinear Schrödinger (NLS) Equation

The evolution equations describing wave propagation over deep or shallow waters may straightforwardly be derived heuristically (Kharif and Pelinovsky 2006). One of the common ways to rigorously derive these equations is based on the asymptotic technique of Engelbrecht et al. (1988). Slowly modulated weakly nonlinear water waves may thus be described with the help of approximate asymptotic equations for wave modulations. The Nonlinear Schrödinger (NLS) equation represents the simplest equation of this kind, first obtained by Zakharov (1968). The detail of its derivation may be found, for example, in Johnson (1997).

4.1.2.1 The Davey-Stewartson and Nonlinear Schrödinger Equations

Let us consider unidirectional wave propagation on the sea surface of arbitrary constant depth; the geometry of the problem is the same as used in Chap. 2 (see Fig. 2.1). The system of governing equations is given by the Laplace equation (2.13), boundary conditions on the free surface (2.28) and (2.30), and the sea bottom condition (2.46).

We will restrict our interest to the narrow-band wave fields (long-wave modulations) so that the solution to the problem may be sought in the form of perturbation expansions similar to (2.33) and (2.34):

$$\phi(X,Y,Z,T) = \sum_{n=0}^{\infty} \varepsilon^{n+1} \phi_n(X,Y,Z,T), \tag{4.10}$$

$$\eta(X,Y,Z,T) = \sum_{n=0}^{\infty} \varepsilon^{n+1} \eta_n(X,Y,Z,T), \tag{4.11}$$

where

$$\phi_n = \sum_{m=-\infty}^{\infty} \phi_{n,m} E^m, \tag{4.12}$$

$$\eta_n = \sum_{m=-\infty}^{\infty} \eta_{n,m} E^m, \tag{4.13}$$

$$E^m = \begin{cases} 1, & m = 0 \\ 1/2 \exp\left[im\left(K_0 X - \Omega_0 T\right)\right], & m \neq 0 \end{cases}.$$

For the sake of simplicity, we choose the direction of wave propagation along the OX axis so that the carrier (fundamental) wave has wave vector $\mathbf{K}_0 = (K_0, 0), K_0 > 0$, and cyclic frequency $\Omega_0 > 0$; ε is a small parameter that will be specified later. Relations $\phi_{n,-m} = \phi^*_{n,m}$ and $\eta_{n,-m} = \eta^*_{n,m}$ should be satisfied to provide real values of the surface displacement and the velocity potential. The asterisk denotes the complex conjugate.

With the help of Taylor expansion at the still water level (2.35), the boundary conditions on the sea surface read

$$\eta_T + \eta_X \sum_{j=0}^{\infty} \frac{\eta^j \partial_Z^j \phi_X}{j!} + \eta_Y \sum_{j=0}^{\infty} \frac{\eta^j \partial_Z^j \phi_Y}{j!} - \phi \sum_{j=0}^{\infty} \frac{\eta^j \partial_Z^{j+1} \phi}{j!} = 0 \text{ on } Z = 0, \tag{4.14}$$

$$\sum_{j=0}^{\infty} \frac{\eta^j \partial_Z^j \phi_T}{j!} + \frac{1}{2}\left(\sum_{j=0}^{\infty} \frac{\eta^j \partial_Z^j \phi_X}{j!}\right)^2 + \frac{1}{2}\left(\sum_{j=0}^{\infty} \frac{\eta^j \partial_Z^j \phi_Y}{j!}\right)^2 + \frac{1}{2}\left(\sum_{j=0}^{\infty} \frac{\eta^j \partial_Z^{j+1} \phi}{j!}\right)^2 + g\eta = 0 \text{ on } Z = 0. \tag{4.15}$$

We introduce slow coordinates X_1 and Y_1, and multiple slow times T_1 and T_2 as

$$\frac{\partial}{\partial X} \Rightarrow \frac{\partial}{\partial X_0} + \varepsilon \frac{\partial}{\partial X_1}, \tag{4.16}$$

$$\frac{\partial}{\partial Y} \Rightarrow \frac{\partial}{\partial Y_0} + \varepsilon \frac{\partial}{\partial Y_1}, \tag{4.17}$$

$$\frac{\partial}{\partial T} \Rightarrow \frac{\partial}{\partial T_0} + \varepsilon \frac{\partial}{\partial T_1} + \varepsilon^2 \frac{\partial}{\partial T_2} + \ldots. \tag{4.18}$$

The main contribution in the series (4.12) and (4.13) corresponds to the first harmonic ($m = \pm 1$), so that we put $\varphi_{0,m} = 0$ for $|m| > 1$ and $\eta_{0,m} = 0$ for $m \neq \pm 1$. The term $\varphi_{0,0}$ is responsible for the nonlinear induced flow (see Johnson 1997), and is also a zero-order term. Substituting series (4.16), (4.17), and (4.18) into Eqs. (4.14) and (4.15), and collecting terms of similar harmonic component (power of E) and of similar order (power of ε), one comes to a set of equations that may be resolved.

In particular, the Laplace equation (2.13) results in

$$L_m \phi_{n,m} + 2imK_0 \partial_{X_1} \phi_{n-1,m} + \partial_{X_1}^2 \phi_{n-2,m} = 0, \quad L_m = \partial_Z^2 - m^2 K_0^2. \tag{4.19}$$

The consecutive order-by-order solution of Eq. (4.19) provides the modal (vertical) structure of the surface waves. The leading order mode of the 2D carrier wave is given by (2.47).

Terms with ($n = 0$, $m = 1$) give the dispersion relation (2.52) and the relation between the surface disturbance and the velocity potential:

$$\eta_{0,1} = i\frac{\Omega_0}{g}\phi_{0,1}. \tag{4.20}$$

This relation was also obtained in Chap. 2 (see Eqs. (2.47) and (2.48)). The next order ($n = 1$, $m = 1$) leads to the equation

$$\frac{\partial \eta_{0,1}}{\partial T_1} + C_{gr}\frac{\partial \eta_{0,1}}{\partial X_1} = 0, \tag{4.21}$$

where C_{gr} is the group velocity (2.54), which is given by

$$C_{gr} = \frac{\partial \Omega}{\partial K} = \frac{g}{2\Omega_0}\left[\tilde{d} + K_0 D\left(1 - \tilde{d}^2\right)\right], \quad \tilde{d} \equiv \tanh\left(K_0 D\right). \tag{4.22}$$

To obtain the next order evolution equation, the neighboring harmonic components should be considered ($m = 0, 1, 2$). So, the zeroth and the second harmonics contribute to the carrier wave at this level of accuracy. These orders, solved jointly, give the following equations (Johnson 1997):

$$-i\frac{\partial \eta_{0,1}}{\partial T_2} + \beta_{11}\frac{\partial^2 \eta_{0,1}}{\partial X_1^2} + \beta_{22}\frac{\partial^2 \eta_{0,1}}{\partial Y_1^2} + \alpha_{11}\left|\eta_{0,1}\right|^2 \eta_{0,1} + \alpha_{12}\eta_{0,1}\frac{\partial \phi_{0,0}}{\partial X_1} = 0, \tag{4.23}$$

$$s_1\frac{\partial^2 \phi_{0,0}}{\partial X_1^2} + s_2\frac{\partial^2 \phi_{0,0}}{\partial Y_1^2} = \gamma\frac{\partial \left|\eta_{0,1}\right|^2}{\partial X_1}. \tag{4.24}$$

The summation of Eqs. (4.21) and (4.23), supplemented by (4.24), gives the closed system of equations involving terms of two orders of accuracy:

$$-i\left(\frac{\partial A}{\partial T} + C_{gr}\frac{\partial A}{\partial X}\right) + \beta_{11}\frac{\partial^2 A}{\partial X^2} + \beta_{22}\frac{\partial^2 A}{\partial Y^2} + \alpha_{11}\left|A\right|^2 A + \alpha_{12}A\frac{\partial B}{\partial X} = 0, \tag{4.25}$$

$$s_1\frac{\partial^2 B}{\partial X^2} + s_2\frac{\partial^2 B}{\partial Y^2} = \Gamma\frac{\partial \left|A\right|^2}{\partial X}, \tag{4.26}$$

where $A \equiv \eta_{0,1}$ and $B \equiv \phi_{0,1}$. The small parameter ε used for the derivation of the model, actually defines two small quantities. They are the wave steepness (used when writing the Taylor expansions (4.14) and (4.15)) and spectral bandwidth (see (4.16), (4.17), and the series (4.12) and (4.13)). In the present approach, these quantities are supposed to be of the same order of smallness. The field of the surface displacement and velocity potential are defined according to (4.12), (4.13), and (4.20) as

$$\eta = \mathrm{Re}\left(A\exp\left[i\left(K_0X - \Omega_0T\right)\right]\right), \tag{4.27}$$

$$\phi = \frac{g}{\Omega_0}\,\mathrm{Im}\left(A\exp\left[i\left(K_0X - \Omega_0T\right)\right]\right). \tag{4.28}$$

The systems (4.25) and (4.26) were found by Benney and Roskes (1969) and Davey and Stewartson (1974) and are usually referred to as the Davey-Stewartson system or equation (DS). The two first terms in the LHS of Eq. (4.25) support wave propagation with linear group velocity. The four first terms in the LHS of Eq. (4.25) represent the linear dispersive part. Besides the strict asymptotic calculations, the linear dispersive contribution may easily be obtained heuristically from the dispersion relation (2.57) by using a Taylor expansion about the wave vector of the carrier, $\mathbf{K}_0 = (K_0, 0)$

$$\begin{aligned}\Omega\left(K_0 + K_X, K_Y\right) \approx\ & \Omega\left(K_0, 0\right) \\ & + K_X\left.\frac{\partial\Omega}{\partial K_X}\right|_{(K_0,0)} + \frac{1}{2}K_X^2\left.\frac{\partial^2\Omega}{\partial K_X^2}\right|_{(K_0,0)} + \frac{1}{2}K_Y^2\left.\frac{\partial^2\Omega}{\partial K_Y^2}\right|_{(K_0,0)},\end{aligned} \tag{4.29}$$

where the derivatives give the coefficients of the linear part of Eq. (4.25),

$$C_{gr} = \frac{\partial\Omega}{\partial K}, \quad \beta_{11} = -\frac{1}{2}\frac{\partial^2\Omega}{\partial K^2}, \quad \beta_{22} = -\frac{C_{gr}}{2K_0}. \tag{4.30}$$

The group velocity in (4.30) is given by (4.22). It may be easily seen from Fig. 2.3 that the second derivative of the frequency with respect to the wave number (which is equal to the derivative $C_{gr}{}'(K)$) is negative for all depths, and therefore the coefficient β_{11} is always positive, whereas β_{22} is negative.

The other coefficients in the DS system (4.25) and (4.26) are

$$\begin{aligned}\alpha_{11} &= \frac{g^2\Omega_0}{16C_{ph}^4}\left(1 + 9\tilde{d}^{-2} - 13\left(1 - \tilde{d}^2\right) - 2\tilde{d}^4\right), \\ \alpha_{12} &= \frac{\Omega_0}{2C_{ph}^2}\left(2C_{ph} + C_{gr}\left(1 - d^2\right)\right), \\ s_1 &= C_{LW}^2 - C_{gr}^2, \quad s_2 = C_{LW}^2, \quad \Gamma = -\alpha_{12}\frac{g^2}{2\Omega_0}.\end{aligned} \tag{4.31}$$

The long-wave speed C_{LW} in (4.31) is defined as

$$C_{LW} = \sqrt{gD}. \tag{4.32}$$

Coefficients s_1, s_2, α_{11}, and α_{12} are always positive.

The nonlinear part in Eq. (4.25) includes the effect of nonlinear induced flow (the Stokes flow), described by Eq. (4.26). In the deep-water limit, $s_1 \to \infty$ and $s_2 \to \infty$; therefore, the contribution of the mean flow velocity potential B vanishes, and (4.25) and (4.26) become

$$-i\left(\frac{\partial A}{\partial T}+C_{gr}\frac{\partial A}{\partial X}\right)+\frac{\Omega_0}{8K_0^2}\frac{\partial^2 A}{\partial X^2}-\frac{\Omega_0}{4K_0^2}\frac{\partial^2 A}{\partial Y^2}+\frac{\Omega_0 K_0^2}{2}|A|^2 A=0, \tag{4.33}$$

where

$$\Omega_0=\sqrt{gK_0},\quad C_{gr}=\frac{\Omega_0}{2K_0}. \tag{4.34}$$

Eq. (4.33) is the 2D (2D+1) NLS equation valid for the case of deep water (infinite depth).

The DS system (4.25) and (4.26) transforms into one evolution equation describing waves in the *OXZ* plane when the transverse dynamic is disregarded. Then, the DS equation results in the 1D NLS equation (Zakharov 1968, Hasimoto and Ono 1972), written as follows

$$-i\left(\frac{\partial A}{\partial T}+C_{gr}\frac{\partial A}{\partial X}\right)+\beta\frac{\partial^2 A}{\partial X^2}+\alpha|A|^2 A=0, \tag{4.35}$$

$$\beta=\beta_{11},\quad \alpha=\alpha_{11}+\alpha_{12}\frac{\Gamma}{s_1}. \tag{4.36}$$

Contrary to the deep-water limit, the term of induced flow becomes very important in shallow water, although on deep water $\alpha>0$, it becomes negative when the normalized depth of the basin is less than a critical value $KD=1.363$. This bifurcation value corresponds to a significant change in the nonlinear wave dynamics. For $KD\approx 1.363$, the nonlinear coefficient in Eq. (4.35) turns to zero, and thus, the nonlinear effects appear at higher levels, and may be taken into account through a modified asymptotic scheme (see Johnson 1977, Kakutani and Michihiro 1983, Sedletsky 2003, and Slunyaev 2005).

To conclude this section, we would like to state here two important remarks about the NLS equation. First, the coefficients in the evolution equations turn out to be functions of the carrier wave frequency Ω_0 (or wavenumber K_0). The meaning of this result is illustrated by the expansion (4.29). When deriving the NLS equation, the linear dispersion relation $\Omega(K)$ is approximated by a parabolic function in the vicinity of the carrier wavenumber. Hence, to derive the DS system or NLS-like equation, it is first necessary to define the mean frequency (or wavenumber) of the waves. Although some regular methods of the mean frequency definition exist—for instance, via the spectral moments (see Sect. 2.2.2)—the result is not always robust if the waves are not sufficiently narrow-band. Secondly, the derivation of Eqs. (4.25) and (4.26) supposes two weak effects: (i) nonlinearity, of which the smallness serves for expansions (4.10), (4.11) and the expressions of the boundary conditions in the Taylor expansions (4.14) and (4.15); and (ii) weak modulation (the narrowband approximation) that is employed when considering different harmonics and introducing the slow coordinates (4.16), (4.17). In the derived equations, it is assumed that these effects are of the same order of strength. Otherwise, it is necessary to include additional terms in the evolution equation (Trulsen 2006).

4.1.2.2 The Benjamin-Feir Instability

The Benjamin-Feir instability discussed in the previous section can be studied within the framework of the NLS equation, too. Let us consider the linear stability of a plane wave of real constant amplitude A_0, frequency Ω, and wavenumber K. The solution of the NLS equation (4.35) is sought in the following form

$$A(X,T) = A_0(1+a)\exp[i(KX-\Omega T)], \tag{4.37}$$

where a is a complex function of X and T, so that $|a| \ll A_0$, and $A(X,T)$ is the exact solution of (4.35) when $a \equiv 0$ (which implies that $\Omega = C_{gr}K - \beta K^2 + \alpha A_0^2$). Then, the wave modulation a may exponentially grow with time when the following condition is satisfied:

$$\alpha\beta > 0. \tag{4.38}$$

This classical result can be found in Newell (1981), Johnson (1997), and Dias and Kharif (1999) and is true when $K_0 D > 1.363$. The long perturbations of wavenumber ΔK satisfying

$$0 < \Delta K < \Delta K_{BF}, \quad \Delta K_{BF} = A_0\sqrt{\frac{2\alpha}{\beta}} \tag{4.39}$$

are unstable, while the growth rate is given by

$$\sigma_{BF} = |\Delta K|\sqrt{2\alpha\beta A_0^2 - \beta^2\Delta K^2}, \tag{4.40}$$

where $\sigma_{BF} \equiv -\mathrm{Im}(\sigma)$. The subscript "BF" refers to the Benjamin-Feir instability. The maximum growth rate

$$\sigma_{BF\,\max} = \alpha A_0^2 \tag{4.41}$$

is achieved for wavenumber

$$\Delta K_{BF\,\max} = A_0\sqrt{\frac{\alpha}{\beta}}. \tag{4.42}$$

Let us consider a plane wave with carrier wave vector $\mathbf{K}_0 = (K_0, 0)$, perturbed by a disturbance of wave vector $\Delta\mathbf{K} = (\Delta K_X, \Delta K_Y)$. It is convenient to deal with the deep-water 2D NLS equation (4.33) (or, similarly, the DS system when the constant water case is considered) along the perturbation direction. Hence, the analysis is similar to the 1D case and results in formulas (4.38), (4.39), (4.40), (4.41) and (4.42), where the coefficients should be chosen as

$$\alpha = \frac{\Omega_0 K_0^2}{2}, \quad \beta = \frac{\Omega_0}{8K_0^2}\frac{\Delta K_X^2 - 2\Delta K_Y^2}{\Delta K_X^2 + \Delta K_Y^2}, \tag{4.43}$$

and $\Delta K_X^2 + \Delta K_Y^2 = \Delta K^2$. Instability occurs for long wave perturbations with wave vectors lying in an angular domain bounded by angles $\pm$ atan$(2^{-1/2})$ (it is about $\pm$ 35°).

The analysis for the DS system (4.25) and (4.26) is trickier, but still may be completed analytically (Slunyaev et al. 2002). The DS system for weak 2D modulation of type (4.37) may be reduced to the form (4.35) with coefficients

$$\alpha = \left[\alpha_{11} + \alpha_{12}\frac{\Gamma}{s_1} + \alpha_{11}\frac{s_2}{s_1}\left(\frac{\Delta K_Y}{\Delta K_X}\right)^2\right]\cdot\left[1+\frac{s_2}{s_1}\left(\frac{\Delta K_Y}{\Delta K_X}\right)^2\right]^{-1},$$
$$\beta = \left[\beta_{11} + \beta_{22}\left(\frac{\Delta K_Y}{\Delta K_X}\right)^2\right]\cdot\left[1+\left(\frac{\Delta K_Y}{\Delta K_X}\right)^2\right]^{-1}, \qquad (4.44)$$

which should be substituted into Eqs. (4.38), (4.39), (4.40), (4.41), and (4.42) to derive the stability analysis.

The instability diagram depends on the water depth and direction of propagation of the perturbation with wave vector $\Delta\mathbf{K} = (\Delta K_X, \Delta K_Y)$, which is defined by the tangent of $\Delta K_Y/\Delta K_X$. The instability diagrams in the $(\Delta K_X, \Delta K_Y)$-plane are given in Fig. 4.1 for various depths. The value of the growth rate σ_{BF} varies from zero (black) to maximum (white). For $K_0D < 1.363$, the longitudinal perturbations

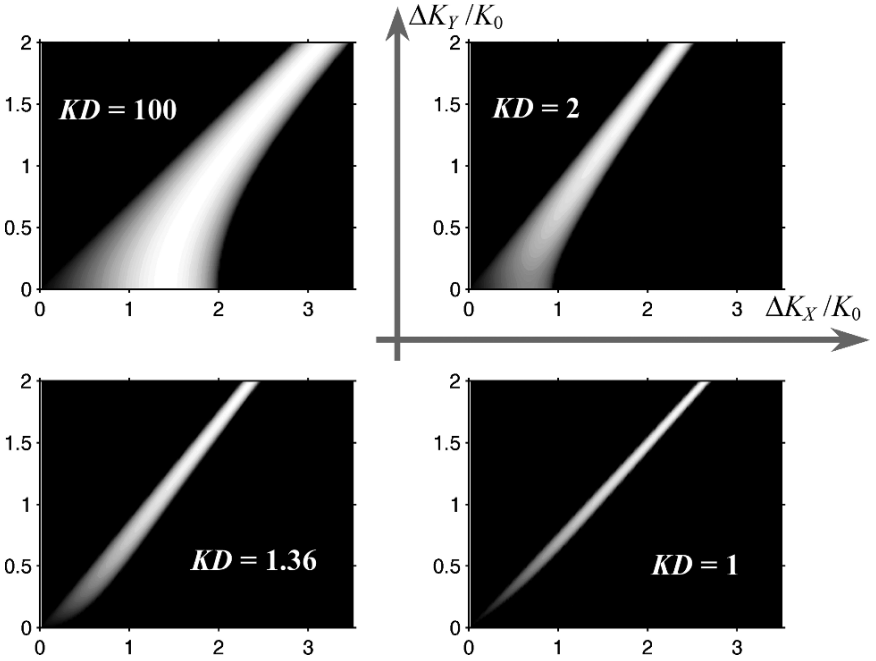

Fig. 4.1 Instability diagrams in the plane of dimensionless perturbation vectors for a plane wave with amplitude $A_0 = 1$ within the framework of the Davey-Stewartson system. Four dimensionless water depths are considered as examples: $K_0D = 100$ (deep water), $K_0D = 2$ (moderately deep water), $K_0D = 1.363$ (cancellation of the nonlinear term in the evolution equation), and $K_0D = 1$ (finite depth close to shallow water)

become stable. Only oblique perturbations develop modulational instability. For $K_0D < 0.5$, the region of instability becomes very narrow, and the instability does not exist practically.

Formulas (4.38), (4.39), (4.40), (4.41), (4.42), (4.43), and (4.44) are valid for the weakly nonlinear theory and are based on a narrowband wave-field approximation. That is why the instability diagram has to be improved by using higher-order models (Trulsen et al. 2000).

The figure shows stability diagrams for various depths from $K_0D = 100$ (deep water) to $K_0D = 1$ (finite depth). As it has been already noted, only oblique perturbations suffer from modulational instability when $K_0D < 1.363$. Generally, the instability regions become smaller when improved models are considered (see Trulsen et al. 2000). The nonlinear stage of BF instability was thoroughly investigated analytically, numerically, and experimentally (see Dias and Kharif 1999).

The Benjamin-Feir instability is one of several other possible unstable wave configurations—i.e., weak perturbations of a uniform plane wave. Other wave systems and structures may be analyzed with respect to stability (nonlinear wave packets, short-crested and bound waves), as reviewed in papers by Roskes (1976), Dhar and Das (1991), Shukla et al. (2006), and Onorato et al. (2006a). This analysis is trickier technically, less evident, and needs further research. Moreover, only the *linear* stability analysis was performed, but nonlinear instabilities are possible as well.

The nonlinear coefficient α for unidirectional waves described by (4.35) vanishes at depth $K_0D = 1.363$ and becomes negative in shallower water; the longitudinal perturbations become stable. Oblique perturbations remain unstable, although the areas of instability shrink. This degeneration of the coefficient due to the specific geometry changes the parity of nonlinear and dispersive terms and requires consideration of higher-order asymptotic expansions, briefly considered just above, to have explicit nonlinear terms included in the evolution equation. The corresponding equation was first derived by Johnson (1977). The equation has the form

$$-i\left(\frac{\partial A}{\partial T}+C_{gr}\frac{\partial A}{\partial X}\right)+\beta\frac{\partial^2 A}{\partial X^2}+\alpha|A|^2A-i\gamma_1|A|^2\frac{\partial A}{\partial X}-i\gamma_2A^2\frac{\partial A^*}{\partial X}+\alpha_2|A|^4A=0, \tag{4.45}$$

where γ_1 and γ_2 relate to the nonlinear-dispersion contribution, and α_2 is the nonlinear coefficient of a higher (fifth) order. Considering the plane wave solution with amplitude A_0 and wavenumber K_0, the condition of possible BF instability excitation is modified when compared with (4.38) and is

$$\beta\alpha+\beta(K-K_0)(\gamma_2-\gamma_1)+A_0^2\left(2\beta\alpha_2-\frac{1}{2}\gamma_2^2\right)>0. \tag{4.46}$$

Hence, the instability diagram for this marginal case is affected by the wave amplitude and the frequency offset, and qualitatively depends on the combination of coefficients in (4.46). The coefficients were first obtained by Johnson (1977), later by Kakutani and Michihiro (1983) and Slunyaev (2005), and partly by Sedletsky (2003). The complexity of the computation of high-order asymptotic expansions results in a difference of the coefficients, so that the analysis of the modulational

instability in the cited papers differs quantitatively, and even sometimes qualitatively. Johnson (1977) concludes that the marginal depth when the BF instability disappears is even larger than $K_0 D \approx 1.363$, owing to the nonlinear corrections (the last summand on the LHS of (4.46)). Results obtained by Kakutani and Michihiro (1983) and Slunyaev (2005) point at the opposite conclusion: the marginal depth becomes shallower. Sedletsky (2006) undertook a further theoretical study of modulational instability within an improved generalized envelope equation theory.

4.1.2.3 The Spectral Instability of Benjamin-Feir Type

In the real sea, the wave field always suffers from random disturbances, which calls statistical considerations. Alber and Saffman (1978) and Alber (1978) derived an equation describing the evolution of the wave envelope of a random wave train. Their analysis started from the DS system, and resulted in a transport equation (see Chap. 2). Using a more general approximate equation, the Zakharov equation (Crawford et al. 1980) investigated the evolution of a random inhomogeneous field of nonlinear deep-water gravity waves. Following Alber and Saffman (1978), they considered the stability of a narrow-band homogeneous spectrum to inhomogeneous perturbations in the limiting cases of the 1D and 2D NLS equations. Using a more realistic spectrum, they obtained results that agree qualitatively with those of Alber and Saffman—namely, they found that the effect of randomness characterized by the spectral bandwidth is to reduce the growth rate and the extent of the instability.

Let us stay now within the framework of the deep-water limit of the 1D version of the NLS equation (4.33). The instability growth rate in the presence of randomness is given by Alber (1978) by

$$\frac{\sigma_{BF}}{\Omega_0} = \frac{1}{8}\frac{\Delta K}{K_0}\left[\sqrt{16\,(K_0 A_{rms})^2 - \left(\frac{\Delta K}{K_0}\right)^2} - \frac{2\sigma_r}{K_0}\right], \tag{4.47}$$

when random waves are distributed according to the Gaussian function and σ_r^2 is the variance that characterizes randomness effects. Variable A_{rms} denotes the root mean-square wave amplitude of the Gaussian random process (if one identifies $A_0 = 2^{1/2} A_{rms}$, then in the limit $\sigma_r \to 0$ (4.47) coincides with (4.39)). The waves are stable with respect to the BF instability if

$$\frac{\sigma_r}{K_0} > 2 A_{rms} K_0. \tag{4.48}$$

In general, the effect of increasing randomness is to restrict the instability criterion, to delay the onset of instability, and to reduce the amplification rate of the modulation. The correlation length scale in the system is defined by σ_r^{-1}, and hence decorrelation of the waves (small correlation length or large σ_r) leads to stabilization of the wavetrain according to the relation

$$\frac{modulation\ length}{correlation\ length} \propto \frac{\sigma_r}{\Delta K_{BF\max}} \propto \frac{\sigma_r K_0}{A_{rms} K_0}. \tag{4.49}$$

In fact, Alber (1978) estimated that the typically measured sea wave parameters result in stable wave trains, although they are close to the neutral stability condition.

When breaking is neglected, wave damping is usually not taken into account considering sea wave dynamics. Nevertheless, loss of energy is always observed in experiments and motivates researchers to argue whether the BF instability is relevant for real waves in the ocean. Generalizations of the NLS equation have been suggested to take into account the effects of wave dissipation and bottom friction in a simple way. Dissipative effects can be introduced in the NLS equation through a linear term with coefficient δ_{dis}

$$-i\left(\frac{\partial A}{\partial T} + C_{gr}\frac{\partial A}{\partial X}\right) + \beta\frac{\partial^2 A}{\partial X^2} + \alpha|A|^2 A - i\delta_{dis}A - i\delta_{fric}|A|^{\gamma}A = 0. \tag{4.50}$$

Voronovich et al. (2008) considered the effect of bottom friction that brought a more sophisticated term into the NLS equation (with coefficient δ_{fric} in (4.50)).

In Eq. (4.50), the parameter $\delta_{dis} \geq 0$ characterizes the effect of linear dissipation. δ_{fric} is a complex number manifesting both the stress at the bottom and the phase lag between the stress and orbital velocity. The power γ is estimated in Voronovich et al. (2008) as $\gamma \approx 0.48$. At first sight, it seems easier to determine the values of the parameters δ_{dis}, δ_{fric}, and γ from experimental data rather than from theoretical developments.

Segur et al. (2005) reported that the plane wave solution becomes linearly and nonlinearly stable when small dissipation δ_{dis} is taken into account. The term of linear dissipation in Eq. (4.50) may be illuminated after the following change

$$A(X,T) = Q(X,T)\exp(-\delta_{dis}T). \tag{4.51}$$

Then Eq. (4.50) becomes

$$-i\left(\frac{\partial Q}{\partial T} + C_{gr}\frac{\partial Q}{\partial X}\right) + \beta\frac{\partial^2 Q}{\partial X^2} + \alpha e^{-2\delta_{dis}T}|Q|^2 Q = 0, \tag{4.52}$$

where we set $\delta_{fric} = 0$ to restrict our interest to effects of linear dissipation only. The exponent in (4.52) reduces the nonlinear effect. It is obvious that if the timescale of the dissipation is much larger than other timescales of the problem, then formulas (4.38), (4.39), (4.40), (4.41), and (4.42) are asymptotically valid. The resulting growth rate of perturbations is

$$\sigma_{BF} = -\delta_{dis} + |\Delta K|\sqrt{2\alpha\beta e^{-2\delta_{dis}T}A_0^2 - \beta^2\Delta K^2}. \tag{4.53}$$

The study of Segur et al. (2005) confirms that the radical expression in Eq. (4.53) defines the onset of the modulational instability. The instability is always cancelled when the time interval becomes sufficiently long. The energy transfer from the carrier wave to the sidebands is still possible and may be substantial if

$$\alpha |A_0|^2 >> \delta_{dis}. \tag{4.54}$$

Nevertheless, the spectral satellites grow for a limited time, and its increase is halted due to the dissipation.

Considering the case of nonlinear wave damping due to bottom friction only ($\delta_{dis} = 0$), the amplitude of the carrier wave decays in a power-law way in contrast to Eq. (4.51). The exponential growth rate has a rather complicated form, but the instability condition is defined by the following expression (one may compare this expression with the radical in Eq. (4.53))

$$\beta \Delta K^2 \left(2\alpha A_0^2 + F_1\right) - \beta^2 \Delta K^4 - F_2 > 0, \tag{4.55}$$

where α and β are given by Eq. (4.44) for the general three-dimensional case; F_1 and F_2 relate to the action of the bottom stress and are functions of the complex parameter δ_{fric}, and wave amplitude A_0. The dissipation hampers the development of instability and shrinks the corresponding instability domain. The longitudinal perturbations turn out to be the most susceptible to be influenced by bottom friction. Voronovich et al. (2008) estimate that the longitudinal perturbations become stable when the nonlinear term in Eq. (4.50) becomes less than the frictional one

$$\alpha |A_0|^{2-\gamma} <\approx \left|\delta_{fric}\right|. \tag{4.56}$$

Since the velocity components decay exponentially at large depths (see formulas (2.58), (2.59), and (2.60)), the bottom friction produces a significant contribution only when the dimensionless depth $K_0 D$ is not large, and becomes unimportant in the deep-water case. For intermediate depths ($K_0 D \sim 1.5$), realistic estimations foresee that the modulational growth may be seriously suppressed by the nonlinear bottom friction or even cancelled at all.

4.2 Rogue Wave Phenomenon within the Framework of the NLS Equation

In what follows, it is convenient to use the dimensionless form of the NLS equation

$$iq_t + q_{xx} + 2|q|^2 q = 0, \tag{4.57}$$

which results from Eq. (4.35) under the following transformations

$$t = \frac{1}{2}\Omega_0 T,\ x = 2K_0 \left(X - C_{gr} T\right), \quad q = \frac{1}{\sqrt{2}} K_0 A^*. \tag{4.58}$$

Eq. (4.57) corresponds to the deep-water case; it is often called the focusing NLS equation with inherent property that the signs between the nonlinear and the dispersive terms are same. Condition (4.38) is satisfied by Eq. (4.57), and hence, modulational instability is possible in this system.

4.2.1 General Solution of the Cauchy Problem

Equation (4.57) is known to be integrable as it was demonstrated by Zakharov and Shabat (1972) with the help of the Inverse Scattering Transform (IST) (see Novikov et al. 1984, Drazin and Johnson 1989). This technique has attributes of the classic Fourier method (spectrum and eigenfunctions) and allows the determination of some explicit exact solutions and an analytical description of model cases. Nevertheless, from the viewpoint of computations it is trickier than the Fourier transform. Two formulations of the IST exist, suggested by Zakharov and Shabat (1972) and Ablowitz et al. (1974), respectively. We will hereafter follow the latter, usually referred to as the Ablowitz-Kaup-Newell-Segur (AKNS) scheme.

Following the AKNS approach, the initial value problem associated with the focusing NLS equation (4.57) is written as follows:

$$\begin{cases} \dfrac{\partial \Psi}{\partial x} = \begin{pmatrix} \lambda & q \\ -q^* & -\lambda \end{pmatrix} \Psi, \\ \dfrac{\partial \Psi}{\partial t} = \begin{pmatrix} a & a_{12} \\ a_{21} & -a \end{pmatrix} \Psi, \end{cases} \tag{4.59}$$

where

$$\Psi = \begin{pmatrix} \Psi_1 \\ \Psi_2 \end{pmatrix}, \quad \begin{cases} a = i|q|^2 + 2i\lambda^2 \\ a_{12} = iq_x + 2i\lambda q \\ a_{21} = iq_x^* - 2i\lambda q^* \end{cases}.$$

The eigenvalues λ are independent of time and constitute the spectrum. The first matrix equation in (4.59) defines the spatial dependence of the eigenfunctions $\Psi(x,t)$, while the second one defines their time dependence. The solution of the initial value problem consists of determining the spectrum for the initial perturbation $q(x,t=0)$ (the direct scattering transform), and then restoring the wave field on the basis of the permanent spectrum and known time-dependent eigenfunctions (the IST).

The spatially localized eigenfunctions correspond to the discrete spectrum, while the others form the continuous spectrum. The discrete spectrum is responsible for the existence of solitary waves discovered first for the Korteweg-de Vries equation by Zabusky and Kruskal (1965) and later found in many important equations and observed in different physical problems. The solitons are localized nonlinear solutions that interact elastically with other solitons and quasilinear waves, preserving their energy and shape. Considering the Cauchy problem on the infinite interval with $q \to 0$ when $x \to \pm\infty$, any initial perturbation evolves into a set of solitons (they correspond to the discrete spectrum) and a spreading due to dispersive oscillatory tail (described by the continuous spectrum). Since the system is conservative, the spreading waves decay in amplitude over time, so the solitons represent the asymptotic solution of the initial value problem for the integrable equation such as the NLS equation.

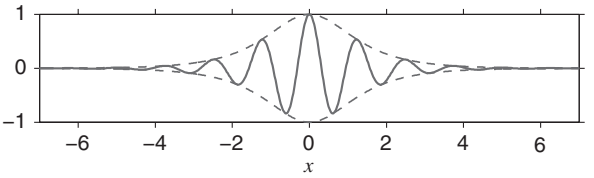

Fig. 4.2 The envelope soliton solution (4.60) with $A_{es} = 1$ and $V_{es} = 10$. The real part of the solution is given by the *solid line*, while the *dashed lines* show $\pm|q_{es}|$

A solitary wave of the NLS equation is represented by the nonlinear envelope as follows

$$q_{es}(x,t) = A_{es} \frac{\exp\left[i\left(xV_{es}/2 - \left(\left(V_{es}/2\right)^2 - A_{es}^2\right)t\right)\right]}{\cosh\left(A_{es}\left(x - V_{es}t\right)\right)}, \tag{4.60}$$

where A_{es} is the amplitude, and V_{es} is the speed of the envelope soliton. The envelope soliton (4.60) is plotted in Fig. 4.2.

The part of the wave field corresponding to the continuous spectrum tends to the following solution when $t \to \infty$

$$q_{tail}(x,t) = \frac{Q}{\sqrt{t}} \exp\left[i\left(\frac{x^2}{4t} + 2Q^2 \ln t + \Theta\right)\right], \tag{4.61}$$

where Q and Θ are functions of the ratio x/t (Ablowitz and Segur 1979).

The multisoliton solution may be found analytically, but even the two-soliton expression (a bi-soliton) has a rather complicated form (see Peregrine 1983, Akhmediev and Ankiewicz 1997). That is why the numerical solution of the NLS equation (4.57) is often used as the less laborious way of analysis. The nonlinear combinations of solitons (4.60) with background waves will be discussed in Sect. 4.2.3.

4.2.2 Nonlinear-Dispersive Formation of a Rogue Wave

The problem, which is at the heart of our attention in this section, is "How can normal waves evolve into a rogue wave?" Let us draw the reader's attention to the fact that the change $q \to q^*$ in the NLS equation (4.57) is equivalent to the time inversion: $t \to -t$. This property becomes understood from relation (4.20), where the complex conjugation corresponds to inversion of the velocity, which should result in time inversion. Due to this symmetry, instead of considering the process of freak wave generation, the opposite evolution may be investigated. Suppose we know the rogue wave profile. What are the waves resulting from its disintegration? Hence, the problem of seeking the wave combinations causing rogue waves is transformed into an initial value problem for a probable rogue wave shape.

We choose the expected freak wave $q(x)$ having a pulse-like shape. It should be understood, however, that the NLS equation is valid for weakly modulated wave

trains, and thus an impulse field $q(x)$ corresponds to a wave group $\eta(X)$ with carrier wavenumber K_0 on the sea surface.

The initial value problem for the NLS equation (4.57) for some shapes of the impulse disturbances was studied by Satsuma and Yajima (1974), Burzlaff (1988), Kaup and Malomed (1995), Desaix et al. (1996), Clarke et al. (2000), and Slunyaev (2001). They provide qualitatively and quantitatively similar results. A particular shape of the expected freak wave

$$q_{fr} = A_p \operatorname{sech}\left(\frac{x}{L}\right), \tag{4.62}$$

where A_p and L are real positive values, will be considered. The initial value problem (4.59) for the potential (4.62) was solved by Satsuma and Yajima (1974), and the discrete eigenvalues are defined by the expression

$$\lambda_n L = \frac{M}{\pi} - n + \frac{1}{2}, \quad n = 1, 2, ..., N_s, \tag{4.63}$$

where the number of discrete eigenvalues is given by

$$N_s = \left[\frac{M}{\pi} + \frac{1}{2}\right]. \tag{4.64}$$

The bracket $[f]$ in (4.64) denotes the integer part of f. The parameter M is the "mass" of the initial wave shape

$$M = \int_{-\infty}^{\infty} |q_{fr}|\, dx, \tag{4.65}$$

which is equal to $M = \pi A_p L$ for a freak wave having the shape of the *sech* function (4.62). Discrete eigenvalues emerge only when the mass exceeds the threshold value $M \geq M_{th}$ where

$$M_{th} = \frac{\pi}{2}. \tag{4.66}$$

Every eigenvalue λ corresponds to an envelope soliton (4.60) with parameters defined by the relation

$$\lambda = \frac{1}{2} A_{es} + i \frac{1}{4} V_{es}. \tag{4.67}$$

Therefore, the integer number N_s is often called the soliton number.

Actually, besides the *sech*-like initial pulse, the solution (4.63) and (4.64) is valid for a variety of real shapes $q_{fr}(x)$ (see Satsuma and Yajima 1974, Burzlaff 1988, Kaup and Malomed 1995, Desaix et al. 1996, Clarke et al. 2000, and Slunyaev 2001). The number M is a convenient parameter of the Cauchy problem since it corresponds to the ratio of nonlinearity with respect to dispersion in Eq. (4.57). This ratio is

$$\frac{q|q|^2}{q_{xx}} \propto |q|^2 L^2 \propto M^2 \tag{4.68}$$

(L is the characteristic length scale) and shows the significance of nonlinear effects compared with dispersive effects. Note that one envelope soliton has "mass"

$$M_{es} = \pi, \tag{4.69}$$

that is twice the threshold value in Eq. (4.66). When the number of discrete eigenvalues N_s is large (and M is large, too) then formula (4.64) with M defined by Eq. (4.65) agrees with the quantization rule of Bohr and Sommerfeld (Landau and Lifshitz 1980) for the scattering problem defined by the first equation in (4.59).

Now, two states of the wave evolution may be compared: the expected freak wave and the result of its evolution over time. When solitons emerge, their amplitudes satisfy Eq. (4.67). The maximum amplitude of the solitary part of the field is equal to $A_{max} = 2\lambda_1$. Applying the formal definition of a rogue wave (I.1), as $A_p/A_{max} \geq 2$, one may easily obtain the necessary condition for the freak wave occurrence from (4.63)

$$M \leq \frac{2\pi}{3} \approx 2.1. \tag{4.70}$$

Condition (4.70) allows the existence of no more than one envelope soliton in the wave field (see (4.64)), which may give birth to a freak wave. If $M < M_{th}$, the wave field does not contain solitons at all. Thus, solitons are not necessary for the formation of a freak wave; and what is more important, rogue waves in the form of very nonlinear (with large M) pulse-like wave packets cannot be formed. An intensive dispersive tail is most important in this process. Its asymptotic form is given by (4.61).

4.2.2.1 Case of a Small Mass Parameter

In the limit $M \to 0$, solitons do not appear (actually, when $M < \pi/2, N_s = 0$). Hence, only spreading decaying wave trains may occur as the result of the Cauchy problem. The problem may be considered in the linear approach as a first approximation. The linear wave grouping due to dispersion has been considered in Chap. 3. The evolution of the Gaussian pulse in the linear limit is described by the exact solution (3.27).[1] In the deep-water case, the dispersion law results in quadratic wavenumber modulation, optimal for the dispersive focusing. Other shapes of the expected rogue waves correspond to other distributions of the energy and phases in the dispersive train, although the quadratic phase modulation remains optimal and becomes apparent over time. Note that solution (4.61) has quadratic phase modulation if Q and Θ are taken as constant. In fact, these functions correct the optimal phase modulation, but such a correction becomes less important if t is large. Formula (3.23), describing the asymptotic behavior of the wave field stemming from the linear disintegration of a rogue wave in the form of the delta-function, does not contain these corrections.

In a more complicated case, the expected freak wave profile may be represented by the Gaussian shape with quadratic phase modulation, specified by the parameter β,

$$q_{fr} = A_p \exp\left[-\left(x/L\right)^2\right] \exp\left(-i\beta x^2\right). \tag{4.71}$$

[1] Note that here there is a temporal wave evolution, while in Chap. 3 it is the spatial one.

Kaup and Malomed (1995) showed that the squared modulation leads to a growth of the thresholds of the emerging soliton (4.66); the discrete eigenvalues move along the real axis closer to zero. This result agrees with simple estimations made in (Slunyaev et al. 2002). Thus, a freak wave, expected as a modulated impulse (4.71), is the result of an even lower number of solitons (i.e., one or none).

4.2.2.2 Competition of the Self-Modulation and Dispersive Effects

When a wave train has both amplitude and phase modulation, the effects of dispersive and nonlinear self-focusing will compete with each other. We illustrate this case with the help of a numerical simulation of the NLS equation (4.57). The initial condition is taken in the following form

$$q(x,t=0) = A_0\,(1+\varepsilon\cos(x/L_{BF}))\exp\left(ix^2/L_{disp}^2\right), \tag{4.72}$$

where $A_0 = 0.043$, $\varepsilon = 0.1$ (it is a small parameter specifying the strength of the amplitude modulation), $L_{BF} = 28$, and L_{disp} varies. Length scales L_{BF} and L_{disp} are responsible for the amplitude and wavenumber modulation, respectively. Results of the numerical simulation of the evolution of the envelope are presented in Fig. 4.3

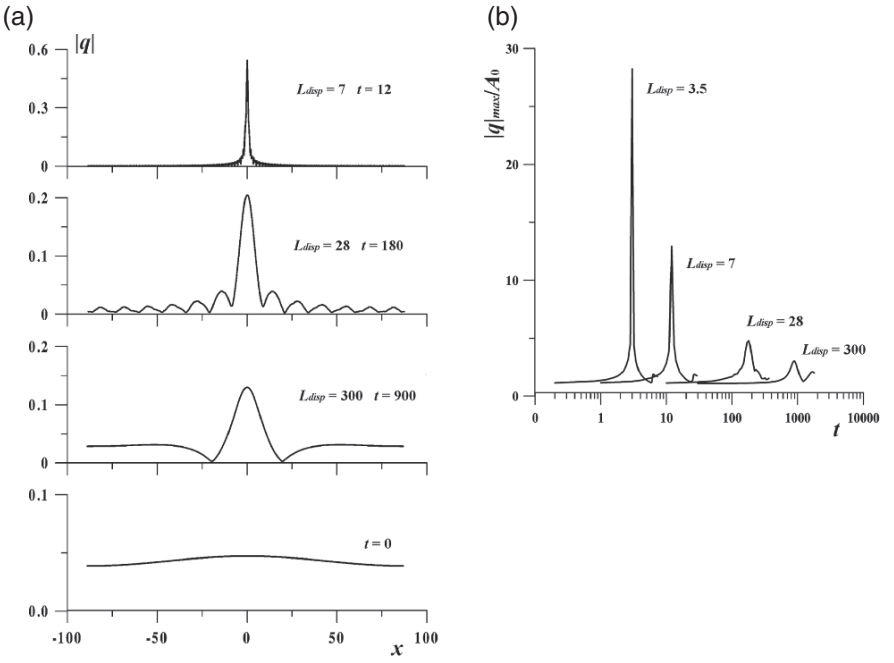

Fig. 4.3 Numerical simulations of the wave train with amplitude and phase modulation (4.72) within the NLS model. (**a**) The initial profile and the amplified wave envelopes for different values of the parameter of phase modulation L_{disp}. (**b**) The maxima of the wave field envelope versus time, corresponding to the cases shown in panel (**a**)

for different values of L_{disp}. Focusing due to the phase modulation (small L_{disp}) happens rapidly and for short time scales, while modulational growth due to the Benjamin-Feir instability (large L_{disp}) occurs for longer time scales. When the modulational instability starts, the growth is exponential and then saturates (see Kharif et al. 2001 and Slunyaev et al. 2002). The dispersive focusing exhibits a power-law dependence and has a sharp maximum (see Sect. 3.2).

4.2.3 Solitons on a Background and Unstable Modes

In the previous section, the Cauchy problem on infinite intervals with zero conditions at infinity has been considered, and the dispersive quasi-linear waves could spread and decay. The case of non-zero background waves, as well as the periodic problem, leads to the nonlinear interaction of the waves of the discrete spectrum with quasi-linear waves that cannot be neglected.

4.2.3.1 Exact Solutions

The so-called "breather" solutions[2] of the NLS equation represent nonlinear interactions of an envelope soliton with a background plane wave. These basic solutions were first obtained by Kuznetsov (1977), Kawata and Inoue (1978), and Ma (1979), and completed later in Peregrine (1983), Akhmediev et al. (1985, 1987), Nakamura and Hirota (1985), Tajiri and Watanabe (1998), Dysthe and Trulsen (1999), Calini and Schober (2002), and Slunyaev et al. (2002). The simplest case of a breather is represented by a single eigenvalue of the modified associated scattering problem when the solution tends to a plane wave at infinity ($x \to \pm\infty$). Except the different boundary conditions, other details of the approach are similar to the classical one given by (4.59). From this point of view, a breather may be called a soliton (usually called Ma soliton) or the superposition of a classical envelope soliton of the NLS equation with a plane wave. Naturalness and richness of this interpretation will be demonstrated below. We will use the general form of this solution, obtained directly from the inverse scattering problem in Slunyaev et al. (2002) and through the Hirota method in Tajiri and Watanabe (1998). For the dimensionless NLS equation (4.57), the solution with a single eigenvalue λ is given by

$$q_{br}(x,t) = e^{2it} \times \\ \times \frac{\cos\mu\cos\left(2\gamma(x-vt)+2i\psi\right) - \cosh\psi\cosh\left(2\Gamma\left(x-V_{br}t\right)+2i\mu\right)}{\cos\mu\cos\left(2\gamma(x-vt)\right) - \cosh\psi\cosh\left(2\Gamma\left(x-V_{br}t\right)\right)}, \qquad (4.73a)$$

[2] Note that this name for solutions of this kind is not generally accepted. For instance, Akhmediev and Ankiewicz (1997) refer to the specific collision of two solitons with equal speeds localized at the same place as a "breather."

where

$$\begin{aligned} \Gamma &= -\sinh\psi\cos\mu, \quad \gamma = \cosh\psi\sin\mu, \\ V_{br} &= -\frac{\cosh 2\psi \sin 2\mu}{\sinh\psi\cos\mu}, \quad v = \frac{\sinh 2\psi\cos 2\mu}{\cosh\psi\sin\mu}, \\ \lambda &= \cos(\mu + i\psi). \end{aligned} \tag{4.73b}$$

Here, V_{br} is the speed of the plane wave perturbation that is traveling as a group. The speed and parameters v, γ, and Γ are defined through the eigenvalue. Solution (4.73) is scaled with respect to the amplitude of the surrounding plane wave ($q_{br}(x,t) \to \exp(2it)$ when $x \to \pm\infty$).

While evolving, the perturbations of the plane wave oscillate with the period

$$T_{br} = \frac{\pi}{\cos 2\mu \sinh 2\psi} \tag{4.74}$$

and stay within the interval

$$\left|A_{br} - A_{pw}\right| \le |q_{br}| \le \left|A_{br} + A_{pw}\right|, \tag{4.75}$$

where

$$A_{br} = 2\cosh\psi\cos\mu, \quad A_{pw} = 1 \tag{4.76}$$

(A_{pw} denotes the amplitude of the plane wave). The following relations between the breather's and eigenvalue properties may be straightforwardly found from (4.73):

$$\lambda = \frac{A_{br}}{2} - i\sin\mu\sinh\psi \quad \text{and} \quad V_{br} = 4\ \mathrm{Im}\ (\lambda)\,\frac{1+\coth^2\psi}{2}. \tag{4.77}$$

V_{br} is the breather velocity defined in (4.73b), and A_{br} plays the role of the breather amplitude.

Solution (4.73) may look differently, like a pulsating disturbance (Fig. 4.4a) or like a propagating group of the plane wave perturbations (Fig. 4.4b). It is straightforward to see that in the case $\lambda \in \Re$ the solution (4.73) tends to the time-periodic Ma soliton when $\lambda > 1$,

$$q_{br}(x,t) = e^{2it+i\varphi_0} \times \frac{\cos(\omega_{br}t - 2i\psi) - \cosh\psi\cosh(2\Gamma(x-x_0))}{\cos(\omega_{br}t) - \cosh\psi\cosh(2\Gamma(x-x_0))}, \tag{4.78}$$

where

$$\Gamma = -\sinh\psi,\ \omega_{br} = \frac{2\pi}{T_{br}}, \quad \lambda = \cosh\psi.$$

Solution (4.78) does not propagate, since $V_{br} = 0$. When $0 < \lambda < 1$, the solution (4.73) is reduced to the Akhmediev et al. (1985) solution[3]

[3] Akhmediev et al. (1987) also found a double periodic (in time and space) solution.

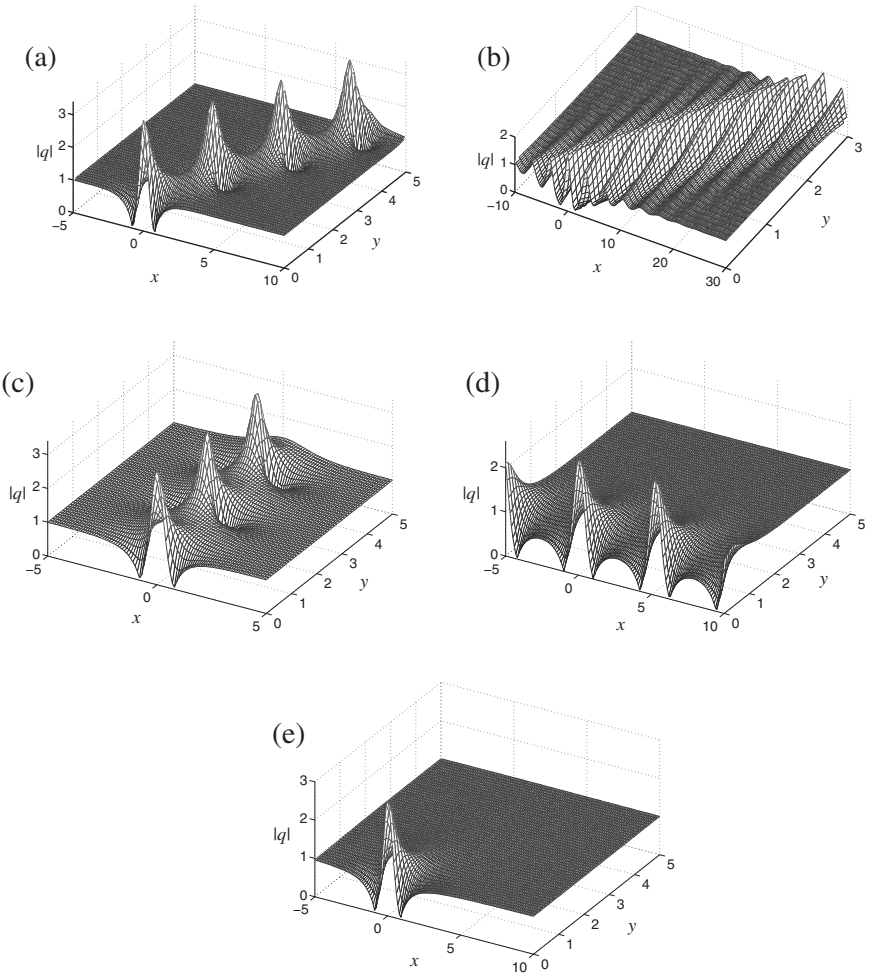

Fig. 4.4 Breather solutions (4.73) of the NLS equation. (**a**) A traveling Ma soliton-like solution ($\lambda = 1.2+0.2i$). (**b**) A traveling envelope-like solution ($\lambda = 0.5+0.2i$). (**c**) The time-periodic Ma soliton ($\lambda = 1.2$). (**d**) The space-periodic Akhmediev solution ($\lambda = 0.8$). (**e**) The rational solution of Peregrine ($\lambda = 1$)

$$q_{br}(x,t) = e^{2it+i\varphi_0} \times \frac{\cos\mu\cos\left(2\gamma(x-x_0)\right) - \cosh\left(\sigma t - 2i\mu\right)}{\cos\mu\cos\left(2\gamma(x-x_0)\right) - \cosh\left(\sigma t\right)}, \tag{4.79}$$

where

$$\gamma = \sin\mu, \quad \sigma = 2\sin\left(2\mu\right), \quad \lambda = \cos\mu.$$

The solution (4.79) does not propagate; it is space-periodic and breathes once. The so-called Peregrine (1983) solution is the limit of Eq. (4.73) when $\lambda \to 1$ is imposed:

$$q_{br}(x,t) = e^{2it+i\varphi_0}\left(1 - \frac{4(1+4it)}{1+4(x-x_0)^2+16t^2}\right). \tag{4.80}$$

Nakamura and Hirota (1985) called this rational solution the explode-decay solitary wave. The examples of the particular solutions (4.78), (4.79), and (4.80) are shown in Fig. 4.4c–e.

Peregrine (1983) pointed out that the Kuznetsov-Ma soliton tends to a usual envelope soliton solution of the NLS equation when its amplitude is much larger than the plane wave amplitude ($A_{br} \gg A_{pw}$). According to formula (4.75), the behavior of the general breathing wave (4.73) may evidently be interpreted in some sense as a linear superposition of a nonlinear envelope with its own amplitude A_{br} and a plane wave with amplitude A_{pw}.

Let us now suppose that the soliton has run away from the region of interaction with the plane wave and is propagating over the zero background (see illustration in Fig. 4.5). Since the nonlinear spectrum λ is conserved, the breather's eigenvalue will be related to the envelope soliton parameters by Eq. (4.67). Comparing Eq. (4.77) with Eq. (4.67), one may conclude how the collision with a plane wave affects a soliton: the envelope preserves its amplitude in the interaction, $A_{br} = A_{es}$, but it accelerates (compare the speeds defined by Eqs. (4.67) and (4.77) for the same value of λ). Figure 4.6 illustrates how combinations of envelope and plane wave parameters result in different kinds of breathing waves. Horizontal curves on the

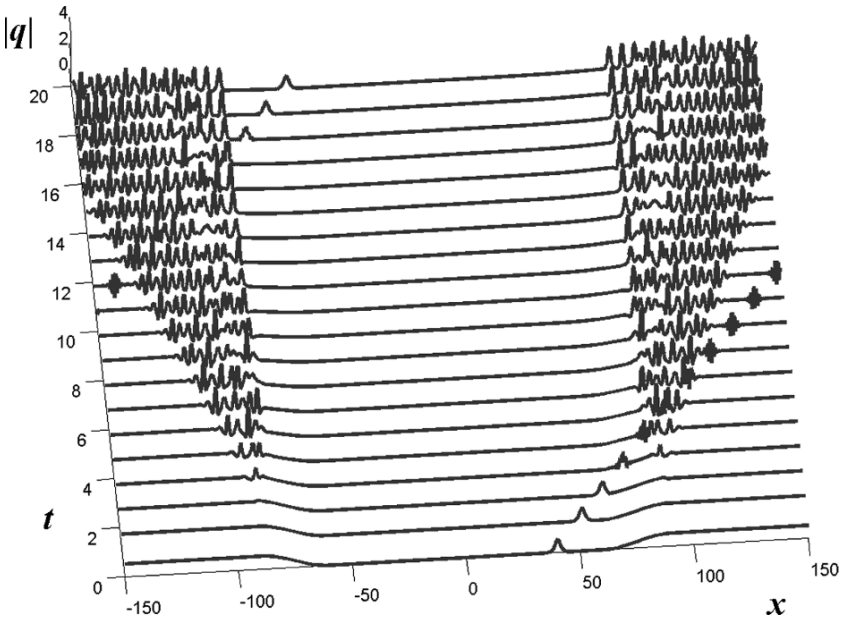

Fig. 4.5 Numerical simulation of an envelope soliton-plane wave collision. The soliton is originally located at the zero background and has rightward velocity, while the plane wave solution ($|x| > 75$) does not move in the chosen frame of reference. Periodic boundary conditions are employed. It is readily seen how the soliton climbs up the plane wave and restores its original shape

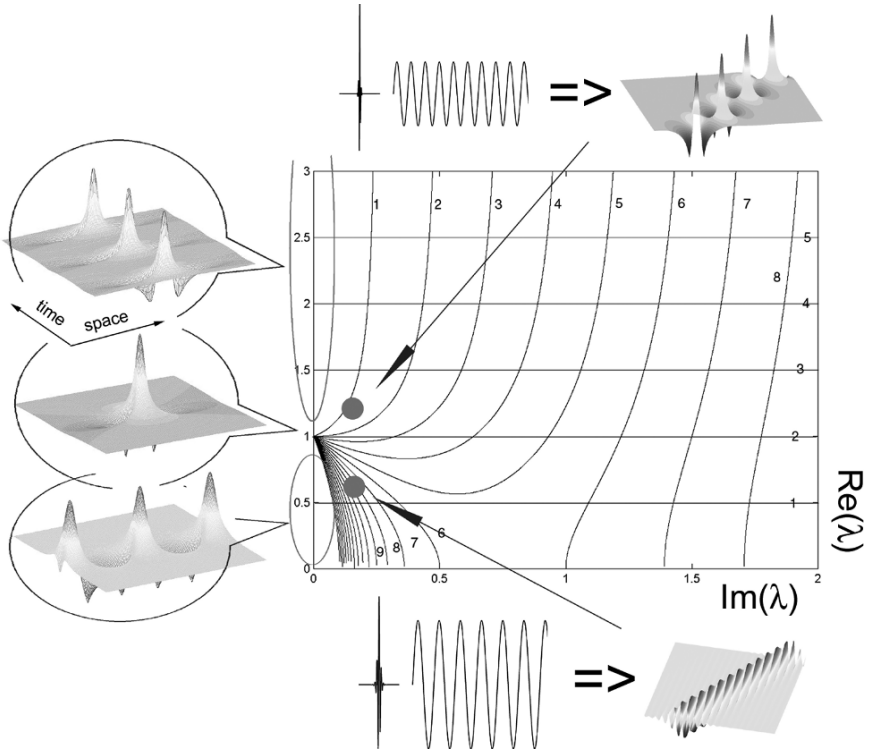

Fig. 4.6 The λ-plane of an envelope soliton over background and corresponding solutions. Left column of images, from *top* to *bottom*: the time-periodic Ma solution ($\lambda > 1$), the limiting Peregrine solution ($\lambda = 1$), and the space-periodic Akhmediev solution ($\lambda < 1$). Horizontal lines on the plane denote dimensionless soliton amplitudes, and bent curves show the isovelocity lines

λ-plane show the isoamplitude lines (the amplitude values are given by numbers); bent curves represent the isovelocity lines (numbers indicate corresponding values of V_{br}). The traveling solution is less influenced by the plane wave when A_{es} is large and/or the difference between the speeds of the soliton and the plane wave is large (Slunyaev 2006).

It follows from formula (4.75) that when an envelope soliton interacts with the background plane wave, the maximum wave field is just the linear superposition of the amplitudes of the soliton and the background wave. The maximum wave amplification that can be achieved in this process (3 times) is obtained with the Peregrine soliton (4.80) (Fig. 4.4e) that presents a single oscillation of one localized perturbation of the plane wave. This solution corresponds to the case $A_{es}/A_{pw} = 2$.

4.2.3.2 Chaotic Behavior of the Wave Modulations

When several breathing waves interact (they may be called multibreathers) more complex solutions have been considered (see Calini and Schober 2002). Besides

the complexity of the analytical description (and comprehension of the dynamics by eye), the case of interacting breathers ("solitonic turbulence;" see Zakharov et al. 2006a,b) is sensitive with respect to any kind of perturbations. This is due to the fact that the NLS breathers are homoclinic orbits of the equation—thus, small perturbations (for example, such as the round-off errors of numerical computations) may result in chaotic behavior of the wave modulations (see Ablowitz and Herbst 1990, Ablowitz et al. 2000, 2001). The integrable NLS equation possesses the Fermi-Pasta-Ulam recurrence (Newell 1981), although its approximate models may lose this property. Therefore, the detailed description of real modulations of sea waves obviously fails, if the cases of many breathers or evolution over time are considered. The statistical approach given in Sect. 4.4 may turn out to be more successful, although the soliton and breather conceptions are often very useful for the understanding of particular wave dynamics.

It is straightforward to show that the Akhmediev solution (4.79) provides an exponential growth, which is equal to the modulational growth rate (4.40) (here values $\alpha = 2, \beta = 1, A_0 = 1, \Delta K = 2\gamma$ should be employed). Hence, the breather solutions indeed describe the development of the Benjamin-Feir instability. The wavenumber corresponding to the maximum growth rate (4.41) results in the length scale $\gamma = 1/\sqrt{2}$, hence, $\mu = \pi/4$. This corresponds to the breather amplitude (4.76) $A_{br} = \sqrt{2}$. The amplification factor achieved by solution (4.79) is then obtained using (4.75) and reads

$$\frac{\max(|q_{br}|)}{A_{pw}} = \frac{A_{br} + A_{pw}}{A_{pw}} = 1 + \sqrt{2} \approx 2.4, \tag{4.81}$$

which is smaller than the result of the Peregrine solution (3 times) but still agrees with the rogue wave criterion (I.1).

In such a way the breathing solutions are closely linked with the modulational instability. They are often associated with *unstable modes* that can be revealed in the wave field with the help of the IST and then used to describe the modulational properties of the waves. Osborne et al. (2005) suggested this approach on the basis of the scattering problem on a periodic domain (long before, the IST was applied by Osborne and Petti (1994) to analyze shallow water laboratory waves). The unstable modes were also studied by Islas and Schober (2005); another way to use the IST to analyze real sea waves was suggested and developed in papers by Slunyaev et al. (2005, 2006) and will be considered in Sect. 4.7.1.

When the statistical description is concerned, the effects of nonlinear instabilities do influence the probability distribution functions. These effects are beyond the bound nonlinear wave corrections and certainly result from the dynamics described in this section. Some recent results on sea wave probabilistic descriptions that involve nonlinear wave-wave interactions and the bridge to the dynamical aspect will be discussed further in Sect. 4.4.

To conclude this section, we briefly present some results on chaos and modulational instabilities that go beyond the NLS equation. Solving the Zakharov equation numerically, Caponi et al. (1982) discovered that owing to the modulational

instability the Stokes wave train evolves into a chaotic system. They called this phenomenon *confined chaos*. Later, Yasuda and Mori (1997) simulated numerically the long-term evolution of a perturbed Stokes wave by modulational instabilities using the fully nonlinear equations. They showed that the evolution of the perturbed Stokes wave trains into Fermi-Pasta-Ulam recurrence or chaos depends on the number of Fourier modes within the unstable range, the initial steepness of the Stokes waves and the nonlinear coupling between the fundamental modes and higher harmonics of the modulation. By means of high-order modeling with sufficiently many degrees of freedom, they demonstrated that Stokes wave trains evolve into chaotic systems. The numerical method used by Yasuda and Mori is due to Dommermuth and Yue (1987) and is presented in the next section.

4.3 Rogue Wave Simulations within the Framework of the Fully Nonlinear Equations

In the previous section, the dynamics of rogue waves have been investigated within the framework of weakly nonlinear theories. The validity of these models can become questionable in accurately describing rogue waves that are strongly nonlinear water waves. The approximate models may be inaccurate when the extreme wave event is occurring. Hence, to have a more realistic description of this phenomenon, it is necessary to use the fully nonlinear equations (2.13), (2.28), (2.30), and (2.31) with initial and boundary values for the potential and elevation. In constant depth and infinite depth, the bottom condition is given by Eqs. (2.46) and (2.61), respectively. Most of the time, these equations are solved numerically. Different numerical methods are available for the spatio-temporal evolution of water-wave groups. Among the many papers devoted to extreme wave events due to modulational instability and dispersive or directional focusing, one can cite the following list, which is not exhaustive: Henderson et al. (1999), Bateman et al. (2001), Clamond and Grue (2002), Touboul et al. (2006), Clamond et al. (2006), Fochesato et al. (2007), Dyachenko and Zakharov (2005), and Kharif et al. (2008). Among the different kinds of numerical methods used commonly to simulate unsteady evolution of strongly nonlinear free surface flows due to modulational instability and dispersive or directional focusing, we present here a High-Order Spectral Method (HOSM) and a Boundary Integral Equation Method (BIEM).

4.3.1 A High-Order Spectral Method

We consider the case of infinite depth and introduce the following dimensionless variables into Eqs. (2.13), (2.28), (2.29), and (2.61): $x = K_0X, y = K_0Y, z = K_0Z, \zeta = K_0\eta, \varphi = \phi \cdot (g/K_0^3)^{-1/2}, p = P/(\rho g/K_0)$, where K_0 is a reference wavenumber. Hence, the kinematic and dynamic boundary conditions become

$$\frac{\partial \zeta}{\partial t}+\frac{\partial \varphi}{\partial x}\frac{\partial \zeta}{\partial x}+\frac{\partial \varphi}{\partial y}\frac{\partial \zeta}{\partial y}-\frac{\partial \varphi}{\partial z}=0 \quad \text{on} \quad z=\zeta, \tag{4.82}$$

$$\frac{\partial \varphi}{\partial t}+\frac{1}{2}\nabla\varphi\cdot\nabla\varphi+p_a+z=0 \quad \text{on} \quad z=\zeta. \tag{4.83}$$

Following Zakharov (1968), we introduce the velocity potential at the free surface $\varphi^s(x,y,z,t)=\varphi(x,y,z=\zeta(x,y,t),t)$ into Eqs. (4.82) and (4.83)

$$\frac{\partial \zeta}{\partial t}=-\nabla\varphi^s\cdot\nabla\zeta+w\left[1+(\nabla\zeta)^2\right], \tag{4.84}$$

$$\frac{\partial \varphi^s}{\partial t}=-\zeta-\frac{1}{2}\nabla\varphi^s\cdot\nabla\varphi^s+\frac{1}{2}w^2\left[1+(\nabla\zeta)^2\right]-p_a, \tag{4.85}$$

with

$$w=\frac{\partial \varphi}{\partial z}\left(x,y,z=\zeta\left(x,y,t\right),t\right). \tag{4.86}$$

The main difficulty is the computation of the vertical velocity at the free surface, w. Following Dommermuth and Yue (1987), the potential $\varphi(x,y,z,t)$ is written as a finite perturbation series up to a given order M

$$\varphi\left(x,y,z,t\right)=\sum_{m=1}^{M}\varphi^{(m)}\left(x,y,z,t\right). \tag{4.87}$$

The term $\varphi^{(m)}$ is of $O(\varepsilon^m)$ where ε, a small parameter, is a measure of the wave steepness. Then, expanding each $\varphi^{(m)}$ evaluated at $z=\zeta$ in a Taylor series about $z=0$, we obtain

$$\varphi^s\left(x,y,t\right)=\sum_{m=1}^{M}\sum_{l=0}^{M-m}\frac{\zeta^l}{l!}\frac{\partial^l}{\partial z^l}\varphi^{(m)}\left(x,y,z=0,t\right). \tag{4.88}$$

At a given instant of time, φ^s and ζ are known so that from Eq. (4.88), we can calculate $\varphi^{(m)}$ at each order:

$$O(1)\text{: }\varphi^{(1)}\left(x,y,z=0,t\right)=\varphi^s\left(x,y,t\right), \tag{4.89}$$

$$O(m)\text{: }\varphi^{(m)}\left(x,y,z=0,t\right)=-\sum_{l=1}^{m-1}\frac{\zeta^l}{l!}\frac{\partial^l}{\partial z^l}\varphi^{(m-l)}\left(x,y,z=0,t\right). \quad m\geq 2. \tag{4.90}$$

These boundary conditions, with the Laplace equations $\Delta\varphi^{(m)}(x,y,z,t)=0$ to be solved in the domain occupied by the water, define a series of Dirichlet problems for $\varphi^{(m)}$.

For 2π-periodic conditions in (x,y) in deep water, $\varphi^{(m)}$ can be written as follows

$$\varphi^{(m)}\left(x,y,z,t\right)=\sum_{j=0}^{\infty}\sum_{l=0}^{\infty}\varphi_{jl}^{(m)}\left(t\right)\exp\left(k_{jl}z\right)\exp\left[i\left(jx+ly\right)\right], \tag{4.91}$$

where $k_{jl}=\sqrt{j^2+l^2}$.

Note that $\varphi^{(m)}(x,y,z,t)$ automatically satisfies the Laplace equation and the condition $\lim \nabla\varphi^{(m)}(x,y,z,t) \to 0$ as $z \to -\infty$.

For constant finite depth d, an alternative decomposition must be used, namely

$$\varphi^{(m)}(x,y,z,t) = \sum_{j=0}^{\infty}\sum_{l=0}^{\infty} \varphi_{jl}^{(m)}(t)\,\frac{\cosh\left[k_{jl}(z+d)\right]}{\cosh\left(k_{jl}d\right)}\exp\left[i(jx+ly)\right]. \tag{4.92}$$

Substitution of (4.91) into the set of Eqs. (4.89) and (4.90) gives the modes $\varphi_{jl}^{(m)}(t)$. The vertical velocity at the free surface is then

$$w = \sum_{m=1}^{M}\sum_{l=0}^{M-m} \frac{\zeta^l}{l!}\frac{\partial^{l+1}}{\partial z^{l+1}}\varphi^{(m)}(x,y,z=0,t). \tag{4.93}$$

Substitution of Eq. (4.93) into the boundary conditions (4.84) and (4.85) yields the evolution equations for φ^s and ζ.

The numerical method used to solve the evolution equations (4.84) and (4.85) is similar to that developed by Dommermuth and Yue (1987). Equations (4.84) and (4.85) are integrated using a pseudo-spectral treatment with $N = JL$ wave modes, where $J = max(j)$ and $L = max(l)$ and retaining nonlinear terms up to order M. Once the surface elevation $\zeta(x,y,t)$ and the potential at the free surface $\varphi^s(x,y,z,t)$ at time t are known, the modal amplitudes may be computed. The spatial derivatives of $\varphi^{(m)}$, φ^s, ζ, and w are calculated in the spectral space, while nonlinear terms are evaluated in the physical space at a discrete set of collocation points (x_j, y_l). Fast Fourier Transforms (FFTs) are used to link spectral and physical spaces. Equations. (4.89) and (4.90) are solved in the spectral space. Evolution equations for φ^s and ζ are integrated in time using a fourth-order Runge-Kutta integrator with constant time step. The calculation accuracy depends on several sources of errors due to truncation in the number of modes J and L, and order M, aliasing phenomenon, numerical time integration, etc. Numerical convergence tests can be found in Dommermuth and Yue (1987) and Skandrani et al. (1996).

Another version of HOSM developed by West et al. (1987) can also be used. The difference between both methods lies in the way we compute w from $\varphi^{(m)}$. West et al. (1987) assume a power series for w as

$$w(x,y,t) = \sum_{m=1}^{M} w^{(m)}, \tag{4.94}$$

where

$$w^{(m)} = \sum_{l=0}^{m-1} \frac{\zeta^l}{l!}\frac{\partial^{l+1}}{\partial z^{l+1}}\varphi^{(m-l)}(x,y,z=0,t). \tag{4.95}$$

The treatment of nonlinear terms in the latter method is useful for comparisons between the truncated fully nonlinear equation and approximate models, such as the Zakharov equation.

4.3.2 A Boundary Integral Equation Method

In this section, we describe a 2D numerical wave tank based on a boundary integral equation method applied to rogue waves due to energy focusing in a small area. The computational domain is defined as a volume of fluid bounded by a bottom, two lateral walls, a paddle, and the free surface (Fig. 4.7). The boundary corresponding to the bottom, lateral walls, and paddle is denoted by $\partial\Omega_{SB}$ while the free surface is denoted by $\partial\Omega_{FS}$. The Laplace equation (2.13) is solved within this domain. The no-flux condition along the solid boundaries $\partial\Omega_{SB}$ is

$$\frac{\partial\varphi}{\partial n} = \mathbf{v}_{SB}\cdot\mathbf{n}, \tag{4.96}$$

where $\mathbf{v}_{SB}$ is the velocity of the rigid boundaries set equal to zero on the bottom and vertical walls and equal to the velocity of the paddle located at the beginning of the numerical wave tank. The unit normal to the boundaries is $\mathbf{n}$.

On the free surface, $\partial\Omega_{FS}$, the potential $\varphi(x,z,t)$ satisfies the kinematic boundary condition written in the following form

$$\frac{\mathrm{D}\mathbf{r}}{\mathrm{D}t} = \nabla\varphi, \tag{4.97}$$

with $\mathbf{r} = (x,z)^t$. The dynamic boundary condition (2.29) is rewritten as

$$\frac{\mathrm{D}\varphi}{\mathrm{D}t} = \frac{1}{2}\nabla\varphi\cdot\nabla\varphi - gz - p_a. \tag{4.98}$$

Hence the set of equations to be solved is the Laplace equation $\Delta\varphi = 0$ in the fluid domain, Eq. (4.96) on the rigid boundaries and Eqs. (4.97) and (4.98) on the free surface. These equations are solved numerically using a boundary integral equation method (BIEM) and a mixed Euler-Lagrange (MEL) time marching scheme. Green's second identity transforms the Laplace equation into the following boundary integral equation for φ

$$\int_{\partial\Omega}\varphi(P)\frac{\partial G}{\partial n}(P,Q)\,d\partial\Omega - \int_{\partial\Omega}\frac{\partial\varphi}{\partial n}(P)\,G(P,Q)\,d\partial\Omega = \alpha(Q)\,\varphi(Q), \tag{4.99}$$

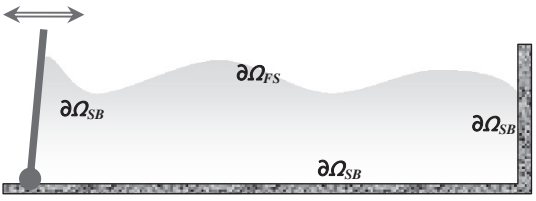

Fig. 4.7 Sketch of the computational domain for the numerical wave tank

where the integration includes both the solid and free surfaces $\partial\Omega = \partial\Omega_{SB} \cup \partial\Omega_{FS}$, G is the 2D free-space Green's function, P and Q denote two points of the fluid domain, and $\mathbf{n}$ is the outward unit vector normal to the boundary. The angle $\alpha(Q)$ is defined as follows: $\alpha(Q) = 0$ or -2π when Q is outside or inside the fluid domain, respectively, and $\alpha(Q) = \theta$ when Q is on the boundary. The angle θ is the inner angle with respect to the fluid domain at point Q along the boundary.

Eq. (4.99) can be written in a more explicit form.

For the free surface $Q \in \partial\Omega_{FS}$:

$$\theta\varphi - \int_{\partial\Omega_{FS}} \varphi(P) \frac{\partial G}{\partial n}(P,Q)\, d\partial\Omega + \int_{\partial\Omega_{SB}} \frac{\partial \varphi}{\partial n}(P)\, G(P,Q)\, d\partial\Omega$$

$$= \int_{\partial\Omega_{SB}} \varphi(P) \frac{\partial G}{\partial n}(P,Q)\, d\partial\Omega - \int_{\partial\Omega_{FS}} \frac{\partial \varphi}{\partial n}(P)\, G(P,Q)\, d\partial\Omega, \qquad (4.100)$$

For the solid boundaries $Q \in \partial\Omega_{SB}$:

$$\int_{\partial\Omega_{FS}} \varphi(P) \frac{\partial G}{\partial n}(P,Q)\, d\partial\Omega + \int_{\partial\Omega_{SB}} \frac{\partial \varphi}{\partial n}(P)\, G(P,Q)\, d\partial\Omega$$

$$= \theta\varphi + \int_{\partial\Omega_{SB}} \varphi(P) \frac{\partial G}{\partial n}(P,Q)\, d\partial\Omega - \int_{\partial\Omega_{FS}} \frac{\partial \varphi}{\partial n}(P)\, G(P,Q)\, d\partial\Omega. \qquad (4.101)$$

The unknowns are $\partial\varphi/\partial n$ on $\partial\Omega_{FS}$ and φ on $\partial\Omega_{SB}$. The above equations, that are assumed to be satisfied at a discrete set of points on the boundary of the fluid domain, are transformed into a linear system of algebraic equations for a finite number of unknowns (for more details see the Appendix). Equations (4.97) and (4.98) are integrated in time using a fourth-order Runge-Kutta integrator.

4.3.3 Numerical Simulation of Rogue Waves Due to Modulational Instability

Henderson et al. (1999) investigated the time evolution of a 2D almost uniform wave train with a small growing modulation. They performed numerical experiments—it was observed that energy focuses into a short group of steep waves, called steep wave events (SWE). Details about the numerical code used to study water wave modulations can be found in Dold (1992). It was found that the breather solutions of the NLS equation fit numerical SWEs rather well. These SWEs are considered to be rogue waves. Hence, the rogue-wave mechanism due to the Benjamin-Feir instability is confirmed in fully nonlinear computations. Later, Clamond and Grue (2002) and Clamond et al. (2006) performed fully nonlinear numerical simulations of lengthy evolution of a 2D localized long-wave packet. The numerical method used is a fast converging iterative solution of the Laplace equation. One part of the solution is obtained by FFT, while another part is highly nonlinear and consists of

integrals with kernels that decay quickly in space (see Clamond and Grue 2001). The result showed how interacting solitary wave groups that emerge from the long wave packet can produce rogue wave events (see Sect. 4.3.5). Dyachenko and Zakharov (2005) and Zakharov et al. (2006b) claimed that rogue wave events are due to solitonic turbulence emerging from modulational instability of Stokes waves. This scenario seems similar to that suggested by Clamond and Grue (2002) and Clamond et al. (2006). Their simulation was based on a numerical method using a conformal mapping of the fluid domain to the lower half plane. More generally, this quasi-solitonic turbulence can appear as a result of the instability of narrow spectral distributions of gravity waves. More details on solitonic turbulence can be found in Zakharov et al. (2006a).

Until now, studies on rogue waves have not taken into account the action of wind. Previous works on rogue waves have not considered the direct effect of wind on their dynamics. It was assumed that they occur independently of wind action, far away from storm areas where wind wave fields are formed. Kharif et al. (2008) considered wind above rogue waves, both numerically and experimentally. Two kinds of mechanisms yielding rogue waves were investigated. In this subsection, we present numerical experiments showing how a rogue event can arise from the modulational instability of a Stokes' wave train with and without wind.

In different situations, several authors have experimentally investigated the influence of wind on the evolution of mechanically generated gravity-water waves. Bliven et al. (1986), Li et al. (1987), and Waseda and Tulin (1999) studied the influence of wind on Benjamin-Feir instability. Contrary to results reported by Bliven et al. (1986) and Li et al. (1987), Waseda and Tulin (1999) found that wind did not suppress the sideband instability. Banner and Song (2002) numerically studied the onset of wave breaking in nonlinear wave groups in the presence of wind forcing. Here, we investigate how wind forcing modifies unforced extreme wave events due to modulational instability.

The generation of extreme wave events can be simply obtained from the Benjamin-Feir instability (or modulational instability) of uniformly traveling trains of Stokes' waves in deep water. It is well-known that these trains are subject to sideband instability producing amplitude and frequency modulations. This instability corresponds to a quartet interaction between the fundamental component (the carrier) $\mathbf{K}_0 = K_0(1,\ 0)$ counted twice, and two satellites $\mathbf{K}_1 = K_0(1+p,q)$ and $\mathbf{K}_2 = K_0(1-p,-q)$, where pK_0 and qK_0 are the longitudinal wavenumber and transversal wavenumber of the modulation, respectively.

As was emphasized in Sect. 4.1.1, the dominant instability of a uniformly-traveling train of Stokes' waves in deep water is the 2D modulational instability (class I) provided that its steepness is less than $s = 0.30$. For higher values of the wave steepness, 3D instabilities (class II) become dominant, phase locked to the unperturbed wave. First we shall focus on the 2D nonlinear evolution of a Stokes' wave train suffering modulational instability without wind action, and then with wind action. Two series of numerical simulations that can be found in Kharif et al. (2008) are presented. They correspond to two wave trains of five and nine waves, respectively.

4.3.3.1 Rogue Waves without Wind Action

A series of 2D rogue-wave simulations in deep water, obtained when using the numerical method described in Sect. 4.3.1, is presented. The wind effect on the water-wave dynamics is neglected, hence the atmospheric pressure, p_a, is set equal to zero in Eq. (4.83).

First, we consider the case of wave trains of five waves. The initial condition is a Stokes wave train of steepness $s = 0.11$, disturbed by its most unstable perturbation, which corresponds to $p \approx 1/5$. The fundamental wavenumber of the Stokes wave is chosen so that integer numbers of the sideband perturbation (satellites) can be fit into the computational domain. For the considered case, the normalized[4] dimensionless fundamental wave harmonic of the Stokes' wave is $k_0 = 5$ and the dominant side bands are $k_1 = 4$ and $k_2 = 6$ for the subharmonic and superharmonic part of the perturbation, respectively. The wave parameters have been rescaled so that the wavelength of the perturbation is equal to 2π. There exist higher harmonics involved in the interactions, which are not presented here. The normalized amplitude of the perturbation relative to the Stokes wave amplitude is initially taken to be equal to 10^{-3}. The order of nonlinearity in the HOSM is $M = 6$; the number of mesh points is greater than $(M+1)k_{max}$, where k_{max} is the highest harmonic taken into account in the simulation. To compute the evolution length of the wave train, the time step is chosen to be equal to one hundredth of the fundamental period of the basic wave, T_0. In this way, the time step satisfies the Courant-Friedrichs-Levy (CFL) condition.

The time histories of the normalized amplitude of the carrier, lower sideband, and upper sideband of the most unstable perturbation are plotted in Fig. 4.8a. Another perturbation that was initially linearly stable becomes unstable in the vicinity of the maximum of modulation, resulting in the growth of the sidebands $k_3 = 3$ and $k_4 = 7$. The nonlinear evolution of the 2D wave train exhibits the Fermi-Pasta-Ulam recurrence phenomenon. This phenomenon is characterized by a series of modulation-demodulation cycles in which initially uniform wave trains become modulated and then demodulated until they are again uniform. Here, one cycle of modulation-demodulation is reported. At time $t \approx 360T_0$, the initial condition is more or less recovered.

At the maximum of modulation $t = 260T_0$, one can observe a temporary frequency (and wavenumber) downshifting since the subharmonic mode $k_1 = 4$ is dominant. At this stage, a very steep wave occurs in the group as it can be seen in Fig. 4.9a. Notice that the solid line represents the free surface without wind effect while the dotted line corresponds to the case with wind effect, which will be discussed later. Figure 4.9b–d shows the free surface profiles at several instants in time. The solid lines correspond to the case without wind action. We can emphasize that no breaking occurs during the numerical simulation. Dold and Peregrine (1986) have numerically studied the nonlinear evolution of various modulating wave trains towards breaking or recurrence. For a given number of waves in the wave train, breaking always occurs above a critical initial steepness, and below, a recurrence

[4] Note the wavenumbers in this Section are normalized in a different way than those in Sect. 4.2.

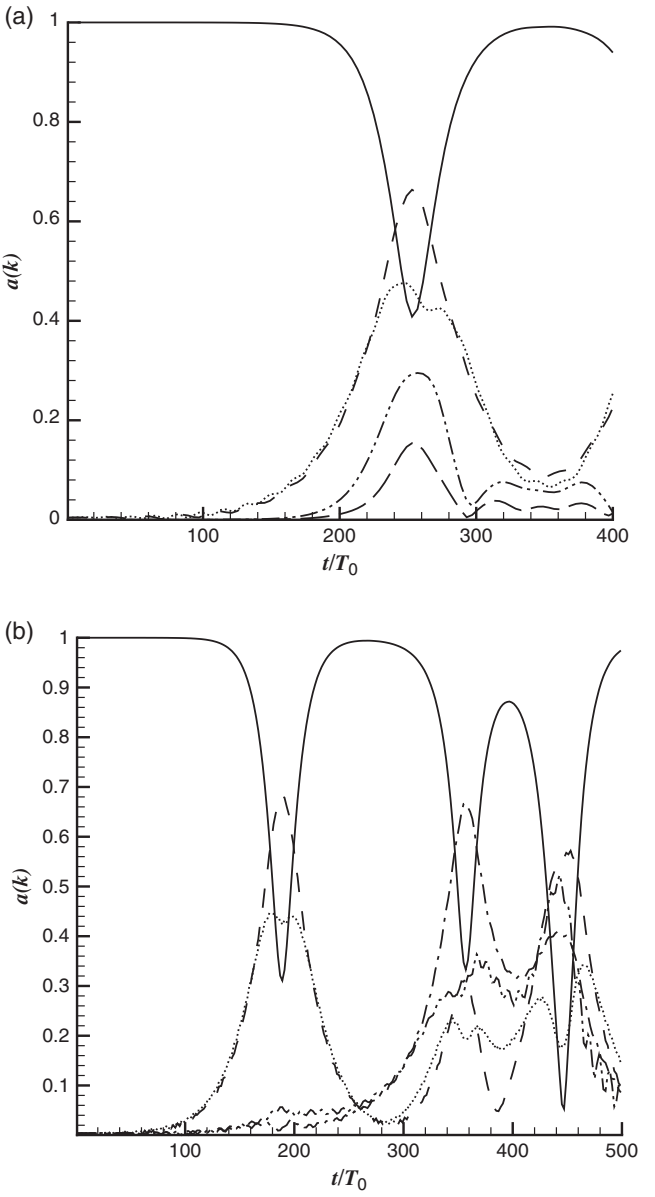

Fig. 4.8 Time histories of the amplitude of the main spectral modes for an evolving perturbed Stokes wave with fundamental wave period T_0, without wind action. (**a**) The fundamental mode $k_0 = 5$ (*solid line*), subharmonic mode $k_1 = 4$ (*dashed line*), superharmonic mode $k_2 = 6$ (*dotted line*). The initial wave steepness is $s = 0.11$. The two lowest curves (*dot-dot-dashed and dot-dashed lines*) correspond to the modes $k_3 = 3$ and $k_4 = 7$. (**b**) The fundamental mode $k_0 = 9$ (*solid line*), subharmonic modes, $k_1 = 7$ (*dashed line*) and $k_3 = 8$ (*dot-dashed line*), and superharmonic modes, $k_2 = 11$ (*dotted line*) and $k_4 = 10$ (*dot-dot-dashed line*). The initial wave steepness is $s = 0.13$

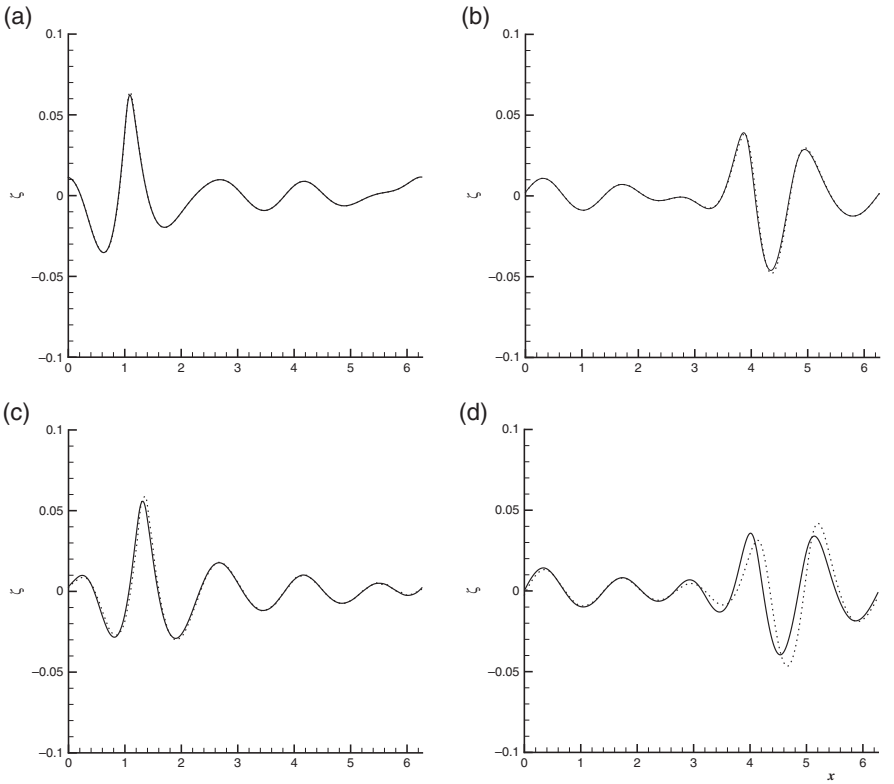

Fig. 4.9 Surface wave profiles at $t = 260T_0$ (**a**), $t = 265T_0$ (**b**), $t = 270T_0$ (**c**) and $t = 275T_0$ (**d**): without wind (*solid lines*) and with wind (*dotted lines*)

towards the initial wave group is observed. This problem was revisited by Banner and Tian (1998) who, however, did not consider the excitation at the maximum modulation of the perturbation corresponding to $p \approx 2/5$.

A second numerical simulation corresponding to the case of wave trains of nine waves is now considered. The initial condition is a Stokes wave of steepness $s = 0.13$, disturbed by its most unstable perturbation, which corresponds to $p \approx 2/9$. The unstable sideband perturbation corresponding to $p = 1/9$ is introduced, as well. Hence, we consider the nonlinear evolution of the wave train when two unstable modulations are now present, whereas in the previous case only one unstable modulation was introduced. The fundamental wave harmonic of the Stokes wave is now $k_0 = 9$, and the dominant sidebands are $k_1 = 7$ and $k_2 = 11$ for the subharmonic and superharmonic parts of the perturbation, respectively, while the satellites $k_3 = 8$ and $k_4 = 10$ are the sidebands of the unstable perturbation corresponding to $p = 1/9$. The time histories of the normalized amplitude of the carrier, lower sideband, and upper sideband of the two unstable perturbations are plotted in Fig. 4.8b. A kind of Fermi-Pasta-Ulam recurrence can be observed, which is stopped at $t \approx 500T_0$ by

the onset of breaking. Here, the onset of breaking is delayed by the presence of two unstable perturbations. This result is in agreement with those of Dold and Peregrine (1986) and Banner and Tian (1998). At $t = 192\ T_0$, $t = 360\ T_0$, and $t = 445\ T_0$, which correspond to the first, second, and third maxima of modulation, an extreme wave event occurs as shown in Fig. 4.10a (solid line), Fig. 4.10e,f. The subharmonic sideband, $k_1 = 7$, is dominant and a temporary frequency downshifting is observed.

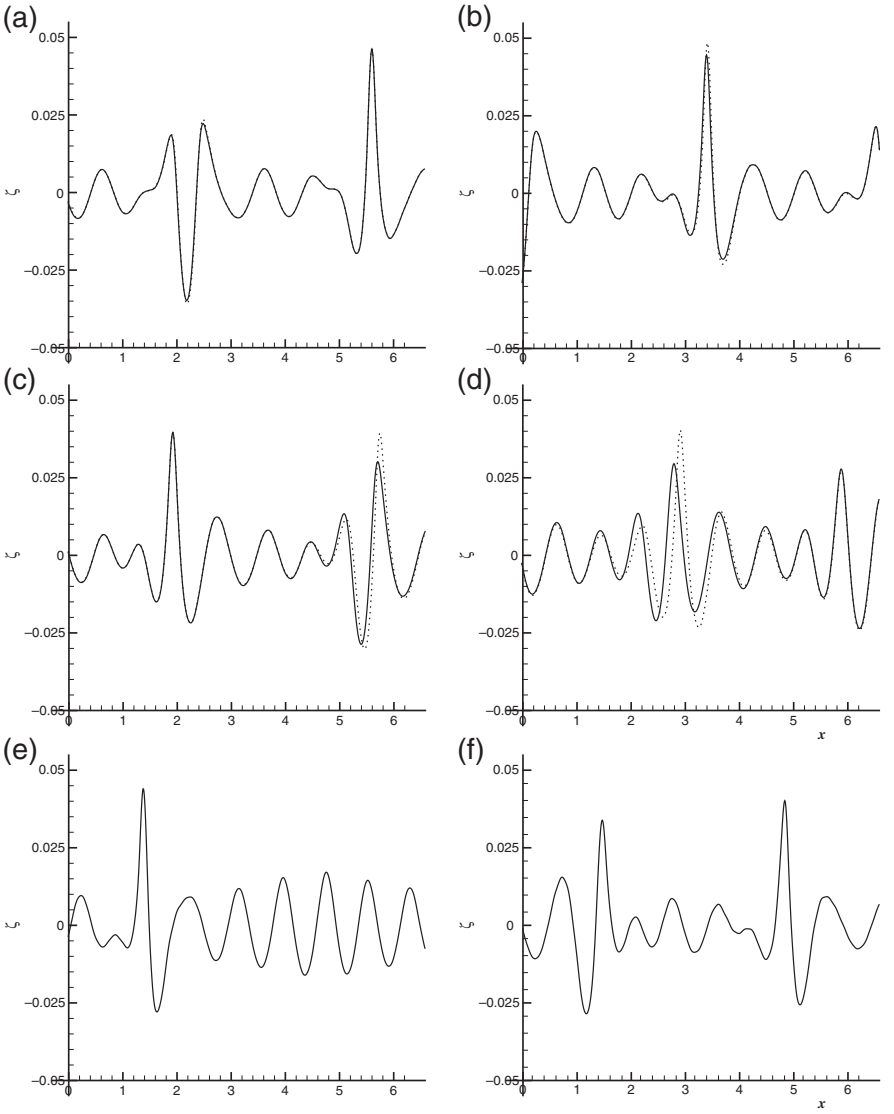

Fig. 4.10 Surface wave profiles at $t = 192\ T_0$ (**a**), $t = 195\ T_0$ (**b**), $t = 200\ T_0$ (**c**), $t = 210\ T_0$ (**d**), $t = 360\ T_0$ (**e**) and $t = 445\ T_0$ (**f**): without wind (*solid lines*) and with wind (*dotted lines*)

Figure 4.10b–d gives the profiles of the wave train at $t = 195\ T_0$, $t = 200\ T_0$, and $t = 210\ T_0$, respectively.

Owing to a mode competition between the satellites of the two unstable disturbances, it is now the subharmonic sideband, $k_3 = 8$, of the initially less unstable perturbation that is dominant at the second maximum of modulation.

4.3.3.2 Rogue Waves with Wind Action

Here, we investigate how wind forcing modifies unforced extreme wave events due to the modulational instability. The questions are: how do the extreme wave events due to the modulational instability under wind action evolve? How are the amplification and time duration of these waves under wind effect modified?

It was shown experimentally (Kharif et al. 2008) that steep wave events occurring in wave groups are accompanied by air flow separation. The experimental results are presented in Sect. 4.5. Jeffreys (1925) suggested that the energy transfer from wind to water waves was due to the form drag associated with the air flow separation occurring on the leeward side of the crests. The air flow separation produces a pressure asymmetry with respect to the wave crest resulting in a wave growth. However, this mechanism can be invoked only if the waves are sufficiently steep. For weak or moderate steepness of the waves, this phenomenon cannot apply and the Jeffreys sheltering mechanism becomes irrelevant. Hence, a modified sheltering effect has been suggested by Kharif et al. (2008). Following Jeffreys, the relationship between the pressure at the interface and the local wave slope is given by

$$P_a = \rho_a s_j \left(U_w - C_{ph}\right)^2 \frac{\partial \eta}{\partial X}, \tag{4.102}$$

where s_j is termed the sheltering coefficient, U_w is the wind speed, C_{ph} is the wave phase velocity, and ρ_a is the density of the air. Expression (4.102) is applied for only steep waves—i.e., when the local wave slope $\partial \eta / \partial X$ becomes larger than a given threshold $(\partial \eta / \partial X)_{c,}$ otherwise $P_a = 0$.

Figure 4.11a,b is similar to Fig. 4.8a,b, respectively, except that now water waves evolve under wind action. Wind forcing is applied over crests of the group of five waves of slopes larger than $(\partial \eta / \partial X)_c = 0.405$, while for the group of nine waves it is applied over crests of slopes steeper than 0.5125. These conditions are satisfied for $256\ T_0 < t < 270\ T_0$ for the first wave train, and for $187\ T_0 < t < 200\ T_0$ and $237\ T_0 < t < 240\ T_0$ for the second—that is, during the maximum of modulation that corresponds to the formation of the extreme wave event. When the values of the wind velocity are too high, the numerical simulations fail during the formation of the extreme wave event, owing to breaking. During the breaking wave process, the slope of the surface becomes infinite, leading numerically to a spread of energy into high wavenumbers. This local steepening is characterized by a numerical blow-up (for methods dealing with an Eulerian description of the flow). To avoid a wave breaking too early, the wind velocity U_w is fixed close to $1.75\ C_{ph}$. Owing to the weak effect of the wind on the kinematics of the crests on which it acts, the phase

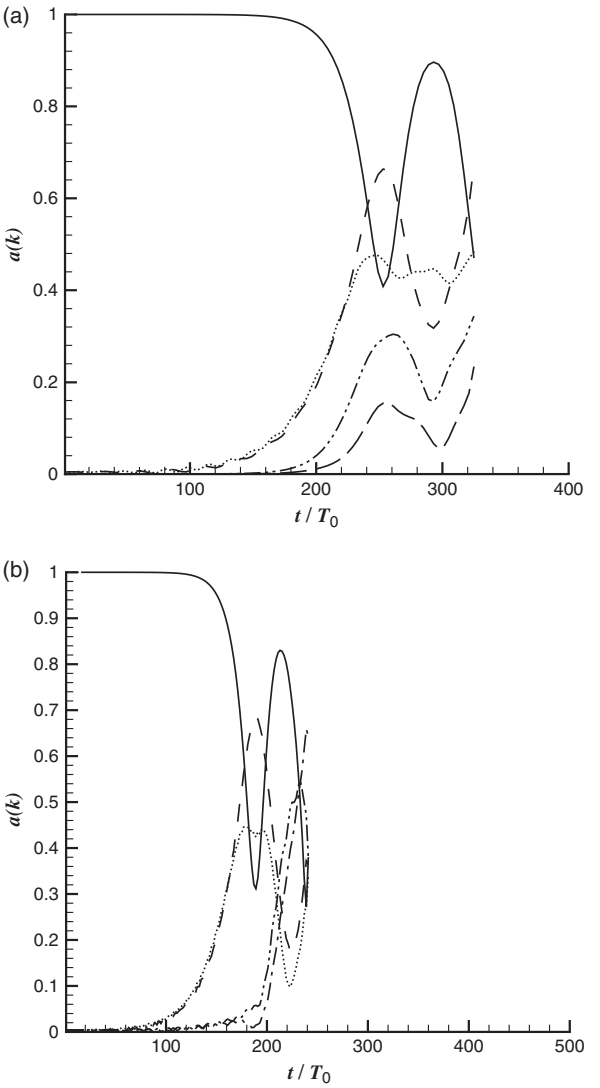

Fig. 4.11 Time histories of the amplitude of the main spectral modes for an evolving perturbed Stokes wave with fundamental wave period T_0, with wind action ($U_w = 1.75C_{ph}$). (**a**) The fundamental mode $k_0 = 5$ (*solid line*), subharmonic mode $k_1 = 4$ (*dashed line*), and superharmonic mode $k_2 = 6$ (*dotted line*). The initial wave steepness is $s = 0.11$. The two lowest curves (*dot-dot-dashed and dot-dashed lines*) correspond to the modes $k_3 = 3$ and $k_4 = 7$. (**b**) The fundamental mode $k_0 = 9$ (*solid line*), subharmonic modes, $k_1 = 7$ (*dashed line*) and $k_3 = 8$ (*dot-dashed line*), and superharmonic modes, $k_2 = 11$ (*dotted line*) and $k_4 = 10$ (*dot-dot-dashed line*). The initial wave steepness is $s = 0.13$

velocity, C_{ph}, is computed without wind. The effect of the wind significantly reduces the demodulation cycle and thus sustains extreme wave event.

This feature is clearly shown in Fig. 4.12a,b corresponding to the wave trains of five and nine waves, respectively. The amplification factor is stronger in the presence of wind, and the rogue wave criterion is satisfied during a longer period of time. In the presence of wind forcing, extreme waves evolve into breaking waves at

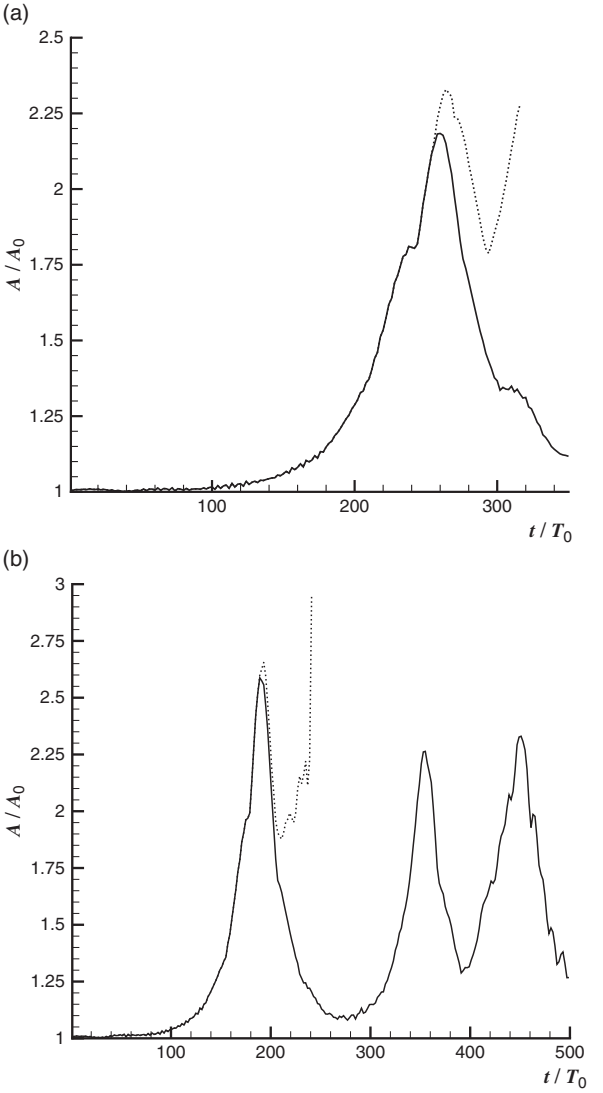

Fig. 4.12 Numerical amplification factor as a function of time without wind (*solid lines*) and with wind (*dotted lines*) for $U_w = 1.75C_{ph}$: (**a**) for the wave train of five waves, (**b**) for the wave train of nine waves

$t \approx 330\ T_0$ and $t \approx 240\ T_0$ (dotted lines in Fig. 4.12a,b) for wave trains of five and nine waves, respectively. For the case of a wave train of five waves, Fig. 4.9a–d display water wave profiles at different instants of time in the vicinity of the maximum of modulation with and without wind. The solid lines correspond to waves propagating without wind, whereas the dotted lines represent the wave profiles under wind action. These figures show that the wind does not modify the phase velocity of the very steep waves while it increases their height and duration. A similar behavior is shown in Fig. 4.10a–d corresponding to the group of nine waves.

We can conclude that extreme waves occurring under wind action in both wave trains present the same features. Furthermore, in the presence of local wind forcing, extreme waves evolve into breaking waves for initial wave trains of steepness $s = 0.11$ and $s = 0.13$ considered here. In another context, Banner and Song (2002) investigated numerically the onset and strength of breaking for deep water waves under wind forcing and surface shear. In their study, wind modeling is based on Miles' theory, which is different from Jeffreys' sheltering mechanism used in this chapter.

4.3.4 Numerical Simulation of Rogue Waves Due to Dispersive Focusing in the Presence of Wind and Current

As shown in Chap. 3, extreme wave events can be generated by means of dispersive enhancement of wave trains. This mechanism is based upon the dispersive nature of water waves. We consider a chirped wave packet with the leading waves having a higher frequency than trailing waves. For this purpose, the numerical wave tank described in Sect. 4.3.2 is used to produce an extreme wave event.

Within the framework of infinite depth and linear waves, the frequency imposed to the wavemaker located at $X = 0$ is given by formula (3.18), where X_f and T_f are the coordinates of the point of focus in the (X,T) plane. The coordinates of the focus point read

$$T_f = \Delta T \frac{f_{\max}}{f_{\max} - f_{\min}}, \tag{4.103}$$

$$X_f = \frac{g\Delta T}{4\pi} \frac{1}{f_{\max} - f_{\min}}, \tag{4.104}$$

where f_{max} and f_{min} are the maximum and minimum values of the frequency (note that the relation between the cyclic frequency Ω and the frequency f is $\Omega = 2\pi\ f$) imposed to the wavemaker during a period of time ΔT.

Within the framework of the linear theory, the focus points are singular points where the amplitude becomes infinite and behaves as $(T_f - T)^{-1/2}$ (see (3.19)). As it was shown by Touboul et al. (2006) and Kharif et al. (2008), when nonlinear effects are introduced, the rogue wave formation mechanism is not suppressed. In this case, the amplitude of the extreme wave event is finite. The frequency of the wavemaker

of the numerical wave tank is varied linearly from $f_{max} = 1.85\,\text{Hz}$ to $f_{min} = 0.8\,\text{Hz}$ during $\Delta T = 23.5\,\text{s}$. The focusing mechanism is investigated with and without wind as well (Touboul et al. 2006, Kharif et al. 2008). A series of numerical simulations has been run for two values of the wind velocity: $U_w = 0\,\text{m/s}$ and $U_w = 6\,\text{m/s}$. For each value of the wind velocity, the amplification factor A of the group between fetches X and 1 m is defined as follows

$$A\,(X, U_w) = \frac{H_{\max}\,(X, U_w)}{H_{ref}}, \tag{4.105}$$

similar to the abnormality index. In (4.105), $H_{max}(X, U_w)$ is the maximum height between two consecutive crests and troughs in the transient group, and the height H_{ref} of the quasi uniform wave train generated at the entrance of the tank is measured at 1 m. Figure 4.13 shows the experimental and computed surface elevation as a function of time at fetch $X = 1\,\text{m}$. The experimental results will be presented in detail in Sect. 4.5.

Using definition (4.105), Fig. 4.14 describes the spatial evolution of the numerically computed amplification factor. For a value of the threshold wave slope fixed to be equal to 0.3, a blow-up of the numerical simulation occurs owing to the onset of breaking. This threshold value is too low and the transfer of energy from the wind to the steep waves leads to wave breaking. The threshold value of the slope beyond which the wind forcing is applied has been increased and is 0.4. This value corresponds to a wave close to the limiting form for which the modified Jeffreys theory applies. The observed asymmetry between the focusing and defocusing regimes

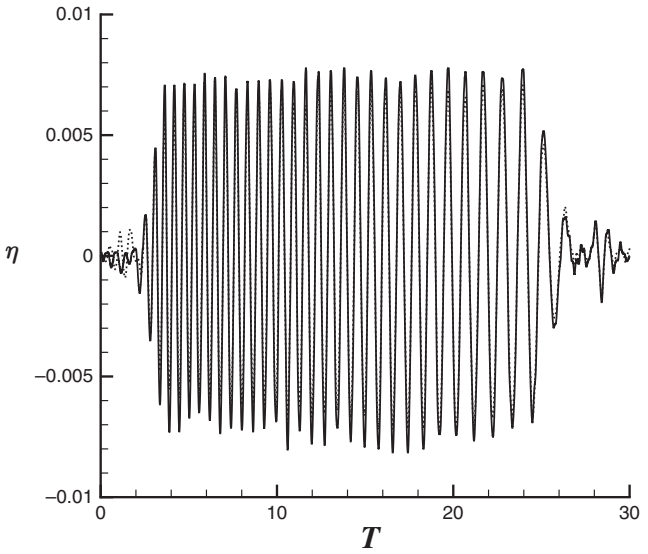

Fig. 4.13 Surface elevation as a function of time at fetch $X = 1\,\text{m}$: experiments (*solid line*) and numerical simulation (*dotted line*) within the framework of the spatio-temporal focusing

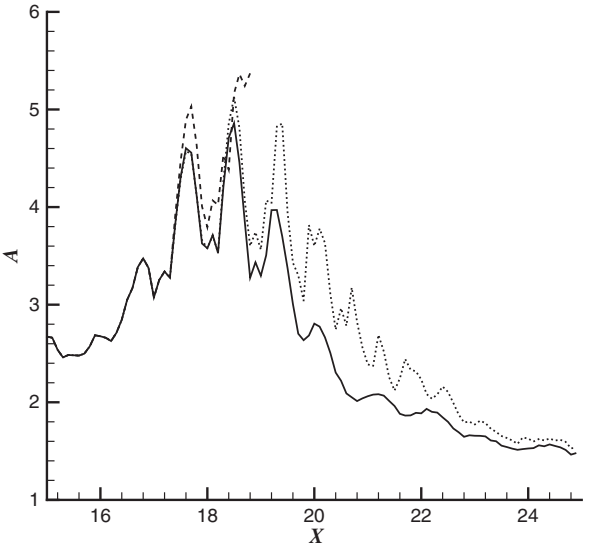

Fig. 4.14 Numerical amplification factor $A(X, U_w)$ as a function of the distance X for two values of the wind velocity within the framework of the spatio-temporal focusing: $U_w = 0$ (*solid line*) and $U_w = 6$ m/s with the threshold value of the wave slope taken to be equal to 0.4 (*dotted line*), $U_w = 6$ m/s with the threshold value of the wave slope taken to be equal to 0.3 (*dashed line*)

can be explained as follows. Without wind, the amplitude of the extreme wave is decreasing during defocusing. In the presence of wind, the modified Jeffreys mechanism that is acting locally in time and space amplifies only the highest waves and hence delays their amplitude decrease during the very beginning of the defocusing stage. The competition between the dispersive nature of the water waves and the local transfer of energy from the wind to the extreme wave event leads to a balance of these effects at the maximum of modulation. This asymmetry results in an increase in the lifetime of the steep wave event, which increases with the wind velocity. Hence, the duration of the wind effect is relatively too short to increase the amplification of the extreme wave event significantly. However, a weak increase of the amplification factor is observed in the presence of wind. The main effect of Jeffreys' sheltering mechanism is to sustain the coherence of the short group involving the steep wave event.

Figure 4.15 shows the numerical amplification factor as a function of the normalized fetch X/X_f, where X_f is the abscissa of the point of focus without wind. The experimental amplification factor is plotted for comparison as well. We can observe an excellent agreement between the numerical and experimental results. The numerical and experimental values of the abscissa of the focus point, X_f, and amplification factor, A, are almost the same.

In the presence of wind of velocity $U_w = 6$ m/s, Fig. 4.16a demonstrates that the numerical and experimental amplification factors deviate from one another beyond the focus point. For a value of the threshold wave slope fixed to be equal to 0.4, the

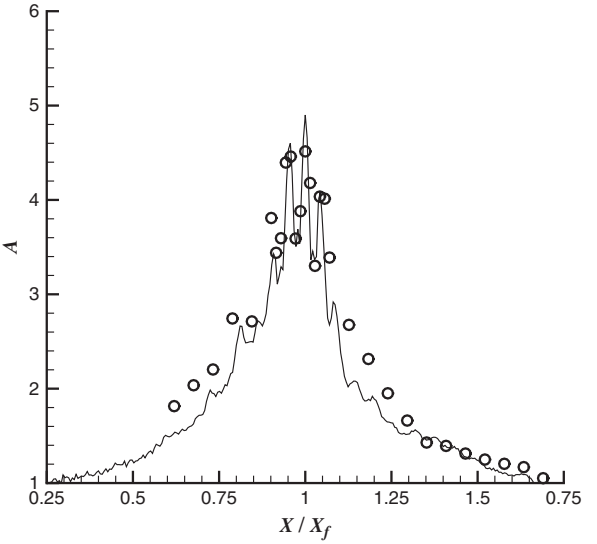

Fig. 4.15 Numerical (*solid line*) and experimental (*circles*) amplification factor $A(X/X_f, U_w)$ as a function of the normalized distance without wind within the framework of the spatio-temporal focusing

Jeffreys' sheltering mechanism is not effective enough in the present case, whereas a reduction of the threshold value to 0.30 produces the onset of breaking at the focus point.

Wind waves are generally propagating in the presence of a current. Figure 4.16b corresponds to the spatio-temporal focusing in the presence of wind and current with a value of the threshold slope taken to be equal to 0.3. The wind velocity is $U_w = 6$ m/s and a uniform following current corresponding to 2% of U_w has been introduced to have the numerical value of the focus point equal to the experimental value. Generally, the current induced by wind is equal to 3% of the wind velocity. More information about the introduction of a current in the model can be found in the paper by Touboul et al. (2007), who considered the formation of rogue waves from transient wave trains propagating on a current. The laboratory experiments of Wu and Yao (2004) should also be reviewed. The introduction of the following current prevents the onset of breaking. During extreme wave events, the wind-driven current may play a significant role in the wind-wave interaction. The combined action of the Jeffreys sheltering mechanism and wind-driven current may sustain longer extreme wave events. We can see good agreement between the numerical simulation and the experiment. The steep wave event is propagating over a longer distance (or period of time) in the numerical simulation as well as experiments.

To summarize, we can claim that within the framework of the spatio-temporal focusing (or dispersive focusing) both numerical and experimental results are in qualitative good agreement even if some quantitative differences have been observed, namely when the wind-induced current is ignored. Moreover, the importance of a following current on the evolution of the wave group has been emphasized as well.

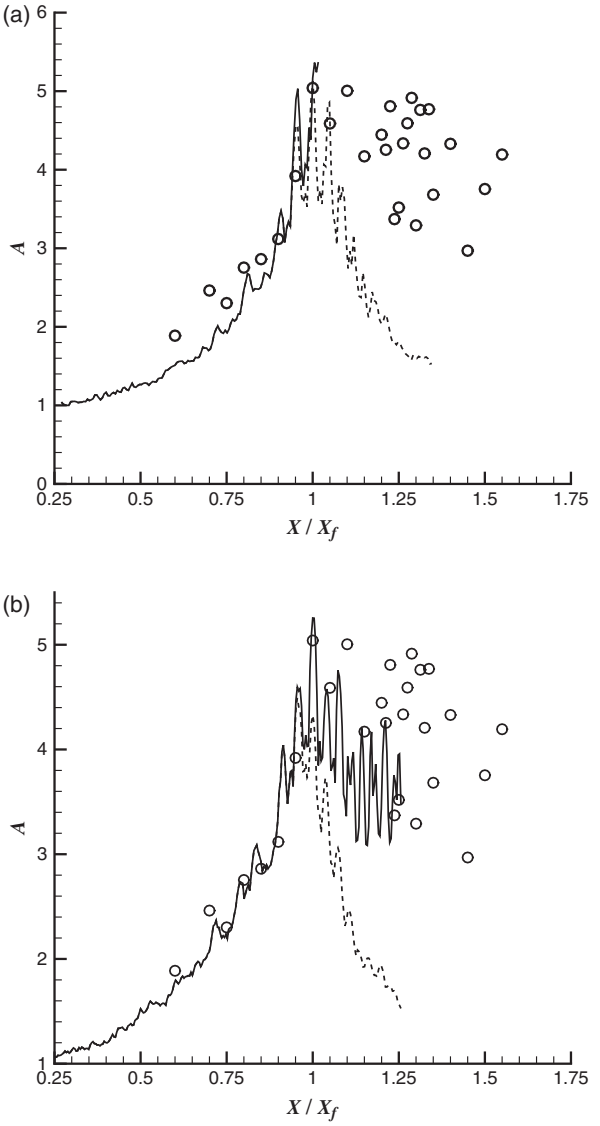

Fig. 4.16 Numerical (*solid and dashed lines*) and experimental (*circles*) amplification factor $A(X/X_f;U_w)$ as a function of the normalized distance for threshold values of the wave slope equal to 0.3 (*solid line*) and 0.4 (*dashed line*) within the framework of the spatio-temporal focusing: (**a**) with wind ($U_w = 6$ m/s), (**b**) in the presence of wind ($U_w = 6$ m/s) and following current

The results of this section have shown that extreme wave events generated by dispersive focusing behave similarly to those due to modulational instability in the presence of wind, as discussed previously. It is found that extreme wave events generated by two different mechanisms exhibit the same behavior in the presence of wind.

4.3.5 Numerical Simulation of Rogue Waves Due to Envelope-Soliton Collision

As it has been discussed in Sect. 4.2, the nonlinear wave groups, also called envelope quasi-solitons, are often a very convenient model for describing the dynamics of modulated waves. The Cauchy problem for an initial localized wave packet was considered by Clamond and Grue (2002) and Clamond et al. (2006). The evolution of a wave packet with an initial steepness of $s = 0.09$ and a bell-shaped (*sech* function) profile has been computed for more than 3,000 wave periods (see Fig. 4.17). During this period of time, three large wave events occur. At about 1,200 wave periods, the wave field consists of three separate solitary wave groups with ordered heights, the steepest being ahead. Until 3,000 wave periods (and later), the groups separate slowly, each group traveling with its characteristic speed. Figure 4.18 illustrates the difference between the weakly nonlinear models (the NLS and extended Dysthe equation) and the fully nonlinear simulation based on Clamond & Grue's scheme regarding envelope dynamics. The analytical theory of the NLS equation predicts that any symmetric envelope (with uniform wavenumber within the group) disintegrates into a finite number of solitons that propagate with the same speed, the linear group velocity, and a small oscillatory tail. For the initial condition considered, it predicts the formation of three solitons that are attached to each other. Furthermore, the corresponding envelope always remains symmetric with respect to the center of the wave group. These bound solitons describe very mild modulations of the envelope amplitude (very long period of recurrence).

The NLS equation predicts the rise of three envelope solitons from the considered initial condition, which is in agreement with the fully nonlinear solution. The shape of each well-separated solitary wave group fits the analytical NLS envelope solutions pretty well. Hence, the observed wave dynamics can be reasonably explained as nonlinear interactions between three perturbed NLS solutions. Nevertheless, it should be noted that the speed of each solitary wave group is not equal to the linear group velocity, as predicted by the NLS theory.

From a qualitative point of view, a somewhat better agreement is obtained with the extended Dysthe equation (Dysthe 1979, Trulsen and Dysthe 1996, Trulsen et al. 2000). This model predicts the early stages of the group splitting (until 300 wave periods) and the characteristic features of the evolution rather well, namely the separation into solitary wave groups and temporary frequency downshifting. However, this model fails to predict the lengthy scenario based on fully nonlinear predictions. Clamond et al. (2006) emphasize that it may be worthwhile to develop a generalization of Dysthe equations, including higher (quintic) nonlinear terms to improve the accuracy and increase the time period of validity.

The result of the fully nonlinear simulation is compared with the fitted exact solution of the NLS equation (the time periodic breather) at the instants of time 155, 156, 157, and 158 wave periods (see Fig. 4.19). This corresponds to the moment of the first steep wave event shown in Figs. 4.17 and 4.18. It is seen that the analytical solution captures some features of the solution rather well and may be used as "first approximation."

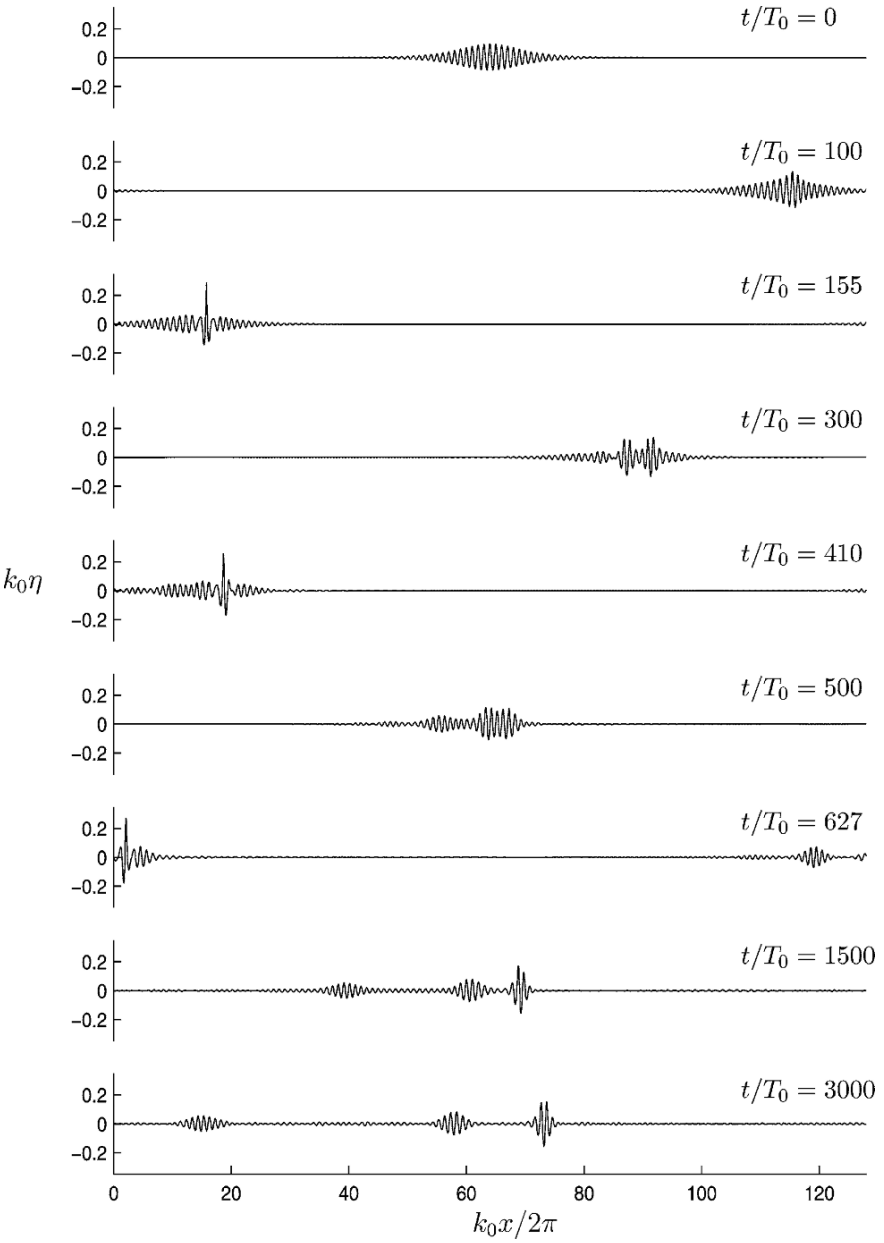

Fig. 4.17 Dynamics of a wave packet with initial *sech*-like shape. k_0 and T_0 denote the carrier wavenumber and period, respectively (see Clamond et al. 2006)

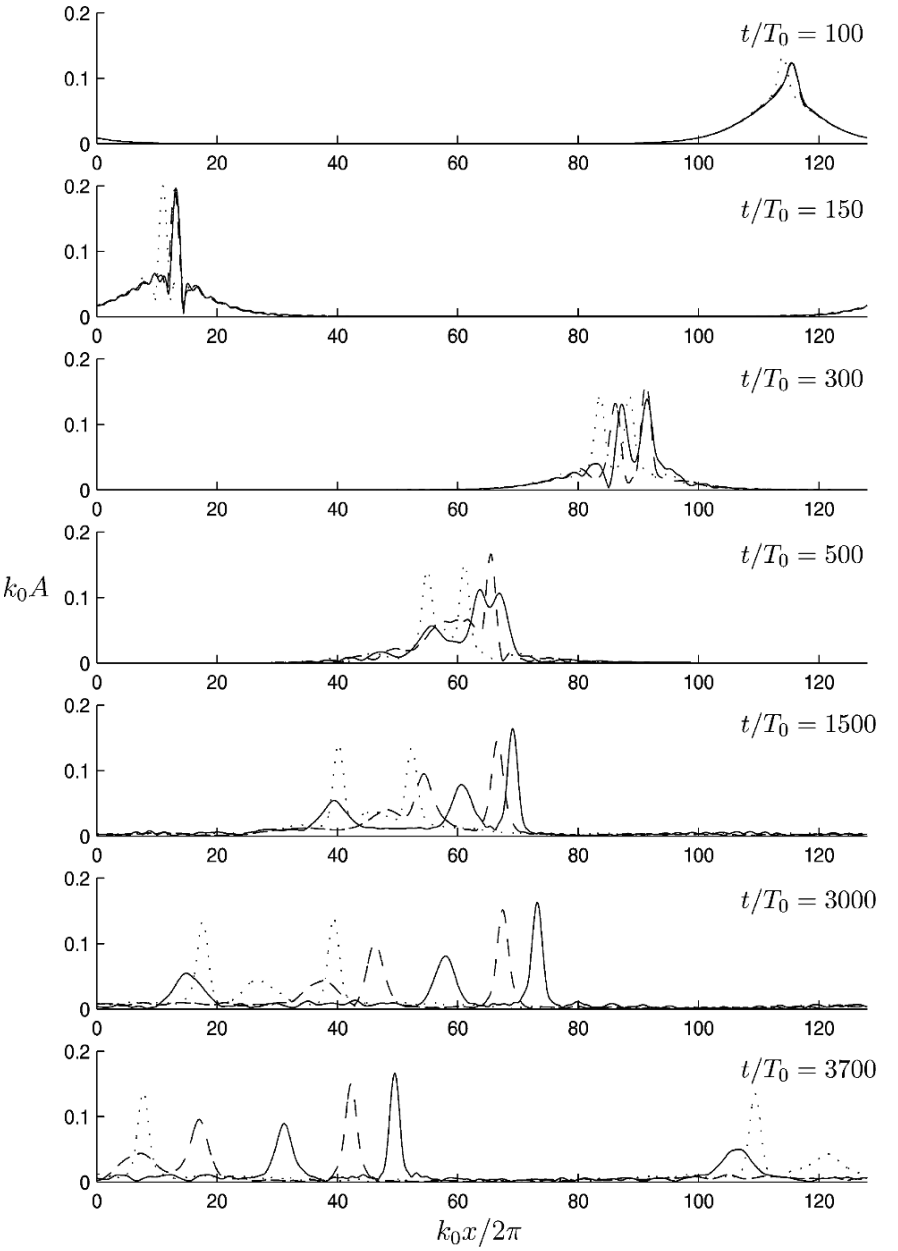

Fig. 4.18 Comparison of the envelope dynamics from Fig. 4.17 (*solid*) with the results provided by the extended Dysthe equation (*dashed*) and the NLS equation (*dots*), k_0 and T_0 denote the carrier wave number and period, respectively (see details in Clamond et al. 2006)

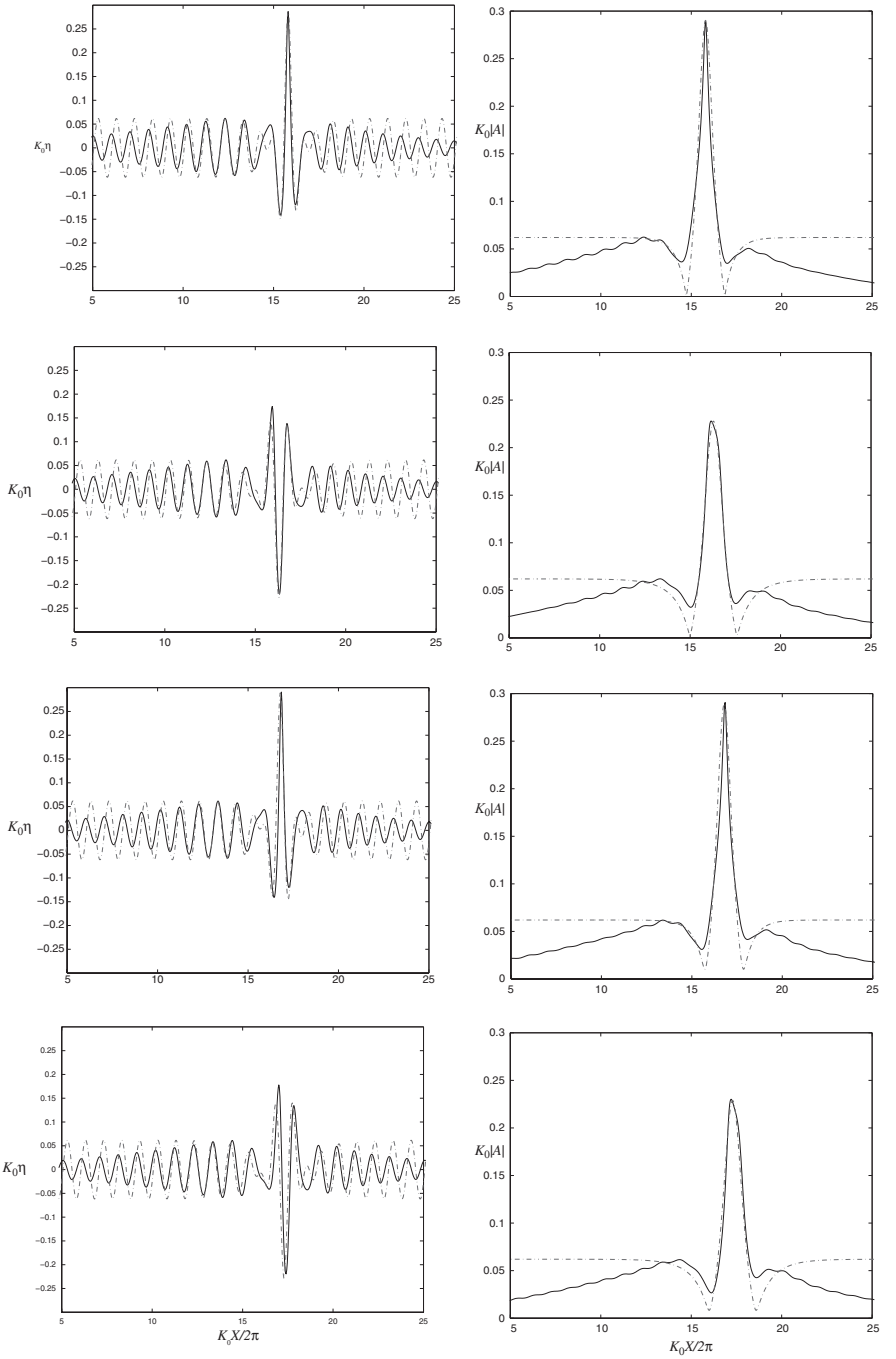

Fig. 4.19 Comparison of the fully nonlinear simulation (*solid*) and the fitted exact NLS solution (*dash*). Elevation (*panels on the left*) and envelope (*panels on the right*) of the surface elevation at $t/T_0 = 155, 156, 157, 158$ versus dimensionless coordinate. K_0 and T_0 denote the carrier wave number and period, respectivel. (see details in Clamond et al. 2006)

Evolution and interaction of strongly nonlinear envelope solitary waves is considered in Zakharov et al. (2006b). The exact solutions of the NLS equation—namely, envelope solitons—have been used to initialize the computation. Weakly nonlinear wave packets behave similarly to the solutions of the NLS equation; they may propagate without deformation and preserve their identity rather well (Fig. 4.20a). Larger

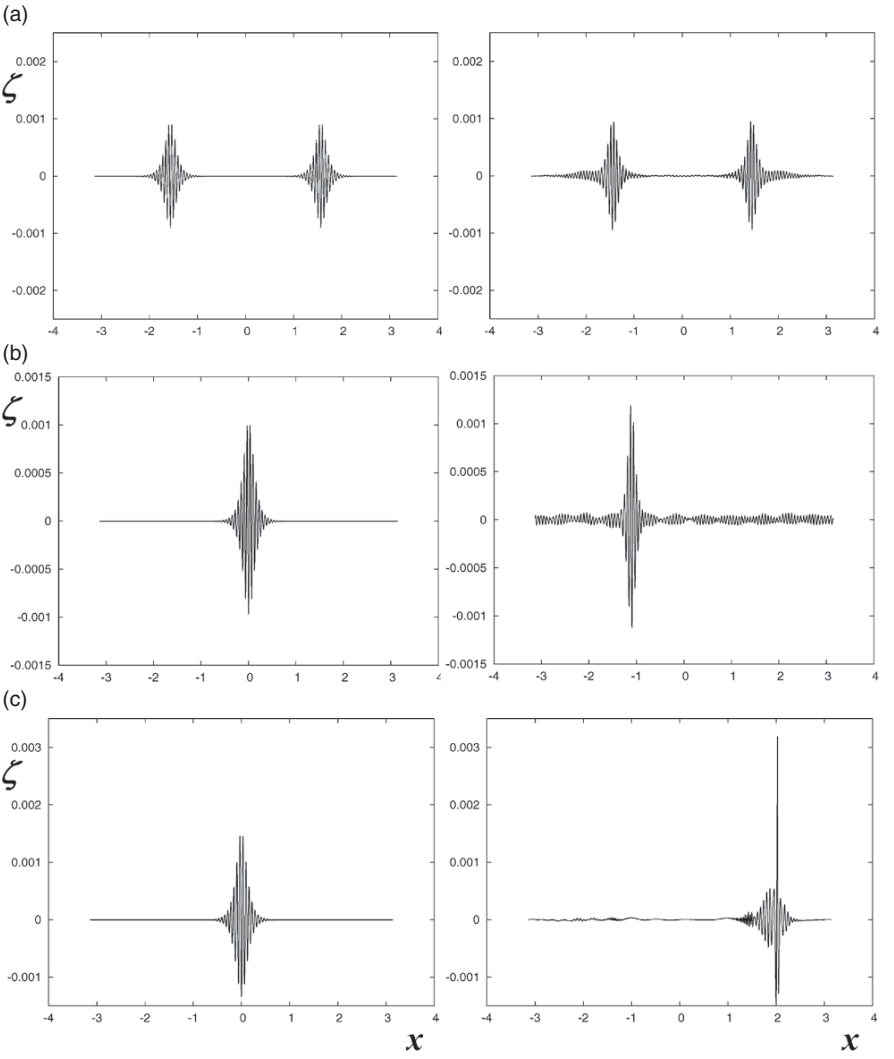

Fig. 4.20 Fully nonlinear evolution of an envelope soliton solutions of the NLS equation. Initial conditions are given in the *left panels*, the result is presented in the *right panels*. (**a**) Collision of two envelope solitons, each with steepness 0.085. (**b**) Evolution of an envelope soliton with steepness 0.1. (**c**) Evolution of an envelope soliton with initial steepness 0.14 (Zakharov et al. 2006b, reproduced with permission from Elsevier)

initial steepness results in modification of the profile of the envelope and radiation (Fig. 4.20b). The envelope approximation completely fails when the steepness is about 0.15 (Fig. 4.20c). The initial wave packet undergoes an additional compression, obviously related to strongly nonlinear effects, leading to the formation of a very high wave. This effect can be explained when the envelope solutions of a definite critical amplitude are unstable and can collapse.

4.4 Statistical Approach for Rogue Waves

It was shown by Caponi et al. (1982) and Yasuda and Mori (1997) that modulated water wave trains may evolve to chaotic states. This feature suggests the use of statistical and spectral descriptions. In looking at the sea surface, we are struck by both randomness and regularity of the wave field. Hence, the prediction of wave parameters of irregular waves may be achieved through a statistical approach.

For 1D propagation, Janssen (2003) studied the influence of the nonlinear four-wave interactions on the occurrence of large surface waves over deep water, using the Zakharov equations (Zakharov 1968, Krasitskii 1994) as a basis with both resonant and non-resonant interactions taken into account. The former interaction evolves on the characteristic time scale $(s^4\Omega)^{-1}$, whereas the latter has a much shorter characteristic time scale $(s^2\Omega)^{-1}$. At the same time, Dysthe et al. (2003) considered the stability of moderately narrow bell-shaped spectra by numerical simulation of the Dysthe equation. It was found that, regardless of the initial spectral bandwidth, the spectra evolve within the characteristic Benjamin-Feir time scale, $(s^2\Omega)^{-1}$, from a symmetric to an asymmetric shape, with a frequency downshifting of the peak. For 2D propagation, the computations of the latter authors confirm the $K^{-2/5}$ (or Ω^{-4}) power law of the spectrum in the inertial range. Using a truncated JONSWAP spectrum as initial conditions, and two kinds of angular distributions corresponding to short- and long-crested waves, respectively, Socquet-Juglard et al. (2005) found similar results and reported on the probability of the occurrence of rogue waves, too. For crest heights less than four times the standard deviation (very close to the significant wave height H_s), they showed that the distributions of surface elevation and crest height fit very well with the theoretical second-order distributions of Tayfun (1980). For larger waves (elevation higher than H_s), this is not always the case. For long-crested waves with a normalized spectral width $\Delta\Omega/\Omega$ less than the steepness s, an increase of the extreme wave events during a phase of spectral change is observed, whereas for short-crested waves, the spectral change does not seem to have much effect on the distribution of extreme wave events. To conclude this extreme wave analysis, Socquet-Juglard et al. (2005) found that the Tayfun distribution is a good approximation, even up to five standard deviations.

The key parameter controlling the importance of the nonlinear wave-wave interactions is the *Benjamin–Feir Index* (BFI) which is the ratio of the wave steepness to the spectral bandwidth. We define the BFI following Janssen (2003) as

$$I_{BF} = \sqrt{2}\frac{K\eta_{rms}}{\Delta\Omega/\Omega} = 2\sqrt{2}\frac{K\eta_{rms}}{\Delta K/K}, \tag{4.106}$$

where K and Ω are the mean wavenumber and frequency of the waves, and $\Delta\Omega/\Omega$ is the spectral bandwidth. One may find other possible definitions of the BFI at the end of this section (see also Olagnon and Magnusson 2004) for the collection of the BF indices applied for the wave record analysis. The dispersion in the deep-water case yields the relation $\Delta K/K = 2\Delta\Omega/\Omega$. The mean values and variances may be defined through spectral moments (see Sect. 2.2). The root mean-square surface displacement η_{rms} is related to the root mean-square amplitude A_{rms} via $A_{rms} = 2^{1/2}\eta_{rms}$. The wave amplitude is assumed to vary slowly compared with the carrier sinusoidal wave length. Therefore,

$$I_{BF} = \frac{KA_{rms}}{\Delta\Omega/\Omega} = 2\frac{KA_{rms}}{\Delta K/K}. \tag{4.107}$$

Following Alber (1978), the random wave field is stable when $I_{BF} < 1$ (here σ_r from Eq. (4.48) is equal to $\Delta\Omega$). In the opposite case, the BF instability is potentially possible if condition (4.39) is satisfied.

The BFI provides a convenient indicator for prediction of modulational instability. A number of recent research projects were aimed at establishing the relationship between the BFI and rogue wave-probability occurrence. Stochastic simulations of random wave fields and laboratory experiments have been performed, where the spectrum evolution and probability of extreme wave occurrence were compared against the values of the BFI (Onorato et al. 2001, 2004, 2005, 2006b; Janssen 2003; Dysthe et al. 2003; Socquet-Juglard et al. 2005). Under the assumptions of weakly non-Gaussian and narrow-band wave trains, Mori and Janssen (2006b) showed that the wave height and the maximum wave height probability distribution depend on the wave variance and kurtosis. The fourth-order statistical moment (kurtosis, κ) is a convenient parameter for measuring the non-Gaussianity of the wave field. For 1D propagation, it is found that the probability of occurrence of extreme wave events increases with kurtosis. The following support of this feature was derived by Mori and Janssen (2006b)

$$\kappa - 3 = \frac{\pi}{\sqrt{3}} I_{BF}^2 \tag{4.108}$$

(the Gaussian process corresponds to $\kappa = 3$). Hence, the kurtosis and the BFI are dependent parameters, and their growths lead to an increase of rogue wave occurrence. The relationship between the freak wave occurrence probability observed in numerical simulations and natural observations was discussed in Mori and Janssen (2006a).

A directional sea was considered in Onorato et al. (2002) within the framework of the extended Dysthe equation. Nonlinear interactions of codirectional waves lead both to an increase of the kurtosis and probability of occurrence of extreme waves, whereas for multidirectional waves the kurtosis is shown to oscillate around $\kappa \approx 3$, indicating that the probability density function for the wave amplitudes is approximately Gaussian.

Let us consider a slightly perturbed plane wave with amplitude A, mean wavenumber K, and long perturbation wavenumber defined by ΔK. According to the instability condition (4.39) for deep-water waves, the plane wave may be unstable if

$$2\sqrt{2}\frac{KA}{\Delta K/K} = \sqrt{2}\frac{KA}{\Delta\Omega/\Omega} > 1. \tag{4.109}$$

From a formal point of view, in terms of the BFI (4.107), this condition transforms into

$$\sqrt{2}I_{BF} > 1. \tag{4.110}$$

The wave modulations split the carrier into groups. The number of individual waves within such a group may be naturally defined as

$$n_x = \frac{K}{\Delta K}, \quad \text{and} \quad n_t = \frac{\Omega}{\Delta\Omega}, \tag{4.111}$$

where n_x and n_t are the numbers of individual waves observed in a snapshot and measured in one point time series, respectively. On deep water, they satisfy the condition $n_t = 2n_x$. Hence, definition (4.107) results in the dimensionless estimation

$$I_{BF} = \bar{s}n_t, \tag{4.112}$$

where $\bar{s}$ denotes the averaged steepness, $\bar{s} \equiv KA_{rms}$.

Taking into account the normalization (4.58), the "mass" integral (4.65) for one wave envelope may be written in the form

$$M \approx \pi 2\sqrt{2}KAn_x = \pi\sqrt{2}I_{BF}, \tag{4.113}$$

where the length of the envelope is estimated as $2\pi/\Delta K$. Hence, the soliton number (4.64) for a smooth pulse-like initial condition for the NLS equation is equal to

$$N_s = \left[\sqrt{2}I_{BF} + \frac{1}{2}\right]. \tag{4.114}$$

Relations (4.113) and (4.114) link the statistically defined BF index and the dynamical parameters of M and N_s. They are, roughly speaking, proportional to each other, when the 1D version of the NLS equation (4.33) is considered,

$$\frac{nonlinearity}{dispersion} \propto \frac{\Omega K^2A^2}{2} \cdot \frac{8K^2}{\Omega(\Delta K)^2} = I_{BF}^2. \tag{4.115}$$

In this sense, the BFI is an analogue to the Ursell number, which is well known for shallow-water waves (see Chap. 5). Table 4.1 collects some important values of these parameters. It is seen that for different applications, the choice of different parameters may be convenient. When dealing with deterministic waves, it is more pertinent to use the quantity $\sqrt{2}I_{BF}$ (see Osborne et al. 2005, Slunyaev 2006).

In Onorato et al. (2001), Janssen (2003), Mori and Janssen (2006b), Gramstad and Trulsen (2007), and Tanaka (2007), it is shown through numerical experiments that the growth of the BFI index indeed qualitatively changes the statistical properties of the wave fields, but the change is not so abrupt and the threshold value of the index is not so obvious. The requirement of robust definition of this parameter

Table 4.1 Key values of parameters characterizing the nonlinear effects versus dispersion

Threshold	Parameter		
	BFI, I_{BF}	M/π	N_s
Rise of envelope solitons from a pulse-like packet	$\geq 1/\sqrt{8} \approx 0.35$	$\geq 1/2$	≥ 1
Onset of the plane wave modulational instability instability	$\geq 1/\sqrt{2} \approx 0.71$	≥ 1	≥ 1
One isolated envelope soliton	$1/\sqrt{2} \approx 0.71$	1	1
Cancellation of the BF instability instability due to randomness	< 1		

on the basis of real natural measurements, where noise perturbations always exist, opens a new problem (Olagnon and Magnusson 2004, 2005). See the discussion in Sect. 4.7.2.

4.5 Laboratory Experiments of Dispersive Wave Trains with and without Wind

Within the framework of dispersive focusing, Sect. 4.3.4 refers to experimental results conducted in the large wind-wave tank of IRPHE at Marseille, Luminy (see Fig. 4.21). The facility consists of a closed loop wind tunnel positioned above a water tank 40 m long, 1 m deep, and 2.6 m wide. The wind tunnel above the water flow is 40 m long, 3.2 m wide, and 1.6 m high. The blower can produce wind velocities up to 14 m/s, and a computer-controlled wavemaker submerged under the upstream beach can generate regular or random waves in a frequency range from 0.5 Hz to 2 Hz. Particular attention has been paid to simulating a pure logarithmic mean wind-velocity profile with constant shear layer over the water surface. A trolley installed in the test section allows probes to be located at different fetches all along the facility. The fetch is defined as the distance between the probes on the trolley and the end of the upstream beach where air flow meets the water surface. The water surface elevation is measured by using capacitive wave gauges: one is located at a fixed fetch 1 m from the upstream beach, and the others are installed on a trolley to measure the water surface elevation at different fetches from the upstream

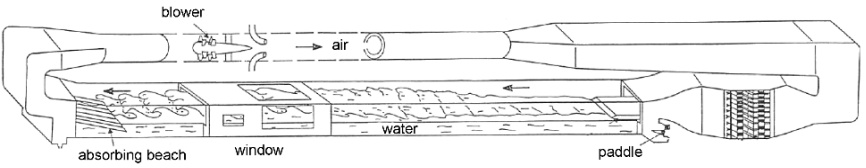

Fig. 4.21 A schematic description of the Large Air-Sea Interactions Facility, IRPHE

beach. The longitudinal and vertical air flow velocity fluctuations have been measured by means of an x-hot wire anemometer.

As in Sect. 4.3.4, extreme wave events are generated by means of a dispersive focusing mechanism with and without wind. The same initial wave train is generated and propagated without wind first, and under wind action for various values of the wind velocity afterwards. When the wind blows, the focusing wave train is generated once the wind waves have developed. For each value of the mean wind velocity U_w, the water surface elevation is measured at 1 m fetch and at different fetches between 3 m and 35 m. The wavemaker is driven by an analog electronic signal to produce this signal linearly varying with time from 1.3 Hz to 0.8 Hz in 10 s, with almost constant amplitude of the displacement. The wavemaker is totally submerged to avoid any perturbation of the air flow that could be induced by its displacement.

Figure 4.22 shows two time series of the probe located at 1 m fetch, recorded with no wind, and under a wind speed of $U_w = 6$ m/s. The probe record, corresponding to a wind velocity equal to 0 m/s, is artificially increased by 10 cm for more clarity of the figure. We see that the two signals are very similar. Some weak differences in amplitude are observed locally. Nevertheless, it is seen that no significant variations are observed, and the experiment is considered to be repeatable in the presence of wind.

More details on experiments conducted in the large wind-wave tank of IRPHE, can be found in Kharif et al. (2008). These results were anticipated in Sect. 3.3. Figure 3.11 presents the time series of the water surface elevation at different fetches for $U_w = 0$ m/s. For the sake of clarity, as it has been done for Fig. 4.22, the probe records given here are recursively increased by 10 cm. As predicted by the linear theory of free deep water waves (no wind), dispersion makes short waves propagate more slowly than long waves, and as a result, the waves focus at a given position in the wave tank leading to the occurrence of a large amplitude wave. Downstream from the point of focus, the amplitude of the group decreases rapidly (defocusing).

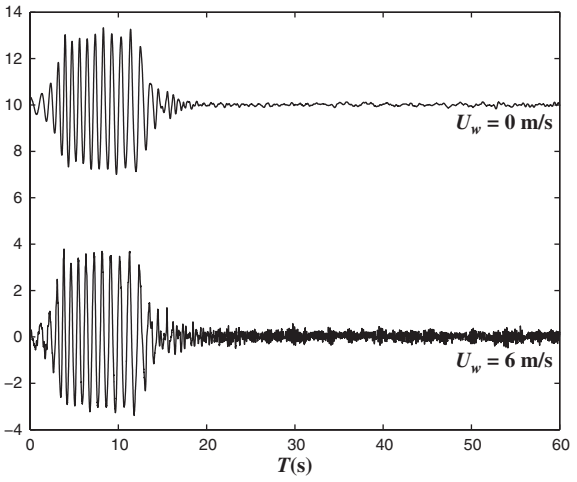

Fig. 4.22 Surface elevation (in cm) at fetch $X = 1$ m for wind speeds $U_w = 0$ and $U_w = 6$ m/s (note that for $U_w = 0$ m/s, the origin of the elevation corresponds to the value 10 cm)

Figure 3.12 shows the same time series of the water surface elevation, at several values of the fetch X, and for a wind speed $U_w = 6$ m/s. The wave groups, mechanically generated by the wavemaker, are identical to those used in the experiments without wind (see Fig. 4.22). Some differences appear in the time-space evolution of the focusing wave train. One can observe that the group of the extreme wave event is sustained longer.

Figure 4.23 gives the amplification factor as a function of the distance from the upstream beach for several values of the wind velocity, equal to 0 m/s, 4 m/s and 6 m/s. We can see that the effect of the wind is twofold: (i) it weakly increases the amplification factor; and (ii) it shifts the focus point downstream. Moreover, contrary to the case without wind, an asymmetry appears between focusing and defocusing stages. The slope of the curves corresponding to defocusing is modified. Note that before the focus point, the wind has no effect on the amplification factor. One can observe that the rogue wave criterion (I.1) is satisfied for a longer period of time. It is also interesting to emphasize that the rogue wave criterion is satisfied for a longer distance, while the wind velocity increases.

The numerical results obtained in Sect. 4.3.4 are confirmed by the experiments, at least qualitatively. A detailed physical analysis of wind-wave coupling over focusing groups may be found in Kharif et al. (2008).

Through experimentation, Baldock et al. (1996) investigated the spatio-temporal focusing of a large number of water waves at one point in space and time to produce a large transient wave group. The experiments were conducted in a 20 m long and 0.3 m wide wave flume. The facility has a maximum working depth of 0.7 m. The waves are generated by a flat bottom-hinged paddle located at one end of the wave flume. The period of the generated waves can vary from 0.4 s to 2.0 s. A total of six surface-piercing wave gauges were used to measure the surface elevation

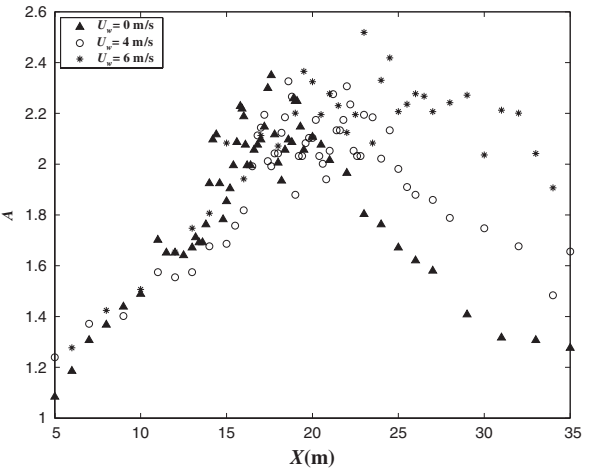

Fig. 4.23 Evolution of the amplification factor $A(X, U_w)$ as a function of the distance for several values of the wind speed

at fixed spatial locations. Baldock et al. (1996) adopted the approach developed by Rapp and Melville (1990) to create an extreme wave within the laboratory flume. They used a linear solution to determine the appropriate phasing of the various wave components. Owing to nonlinear wave-wave interactions present in the experiments, the theoretical and experimental focal points and focus times are different. To simplify the experimental procedure, they imposed that the focus point be located at a fixed distance down-stream of the paddle and the focusing time be set to zero. Measurements of the water surface elevation were compared with both linear wave theory and a second-order solution derived by Longuet-Higgins and Stewart (1960). The experimental results showed that the focusing wave mechanism produces the occurrence of an extreme wave event whose nonlinearity increases with the wave amplitude and reduces with increasing bandwidth. A comparison of the first- and second-order solutions shows that the wave-wave interactions generate a steeper envelope, in which the central wave crest is higher and narrower, whereas the adjacent wave troughs are broader and less deep. The authors suggested that the formation of a focused wave group involves a significant transfer of energy into both higher and lower harmonics.

Within the framework of 2D wave fields, Grue and Jensen (2006) reported velocity and acceleration fields in six very large wave events realized in a series of wave tank experiments. The wave slope is in the range 0.40–0.46 and exceeds the previously mentioned laboratory study of large waves (Baldock et al. 1996) by a factor of about 50%. Focusing water waves were produced in a 24.6 m long wave tank in the Hydrodynamic Laboratory at the University of Oslo. The tank width is 0.5 m and the water depth 0.72 m. The velocities and the material acceleration fields of the waves are obtained by employing an extended Particle Image Velocity (PIV) system (see Jensen et al. 2001). The velocity vector has a magnitude comparable to the wave speed in the strongest case, and is manifested in the jet that develops at the front face of the breaking waves. The nonbreaking waves present a maximal horizontal acceleration up to about $0.70\,g$ in the front face of the wave at vertical level about halfway to the crest. The overturning events present horizontal accelerations up to $1.1\,g$ and vertical accelerations up to $1.5\,g$ in the front face of the wave, at the base below the overturning jet.

Onorato et al. (2006b) conducted a series of experiments in a long water-wave flume at Marintek in Trondheim (Norway). The length of the tank is 270 m, its width is 10.5 m, and its depth is 10 m for the first 85 m, then 5 m for the rest of the flume. A horizontally double-hinged flap type wavemaker located at one end of the tank was used to generate the long-crested waves, whereas an absorbing beach is located at the end opposite from the wavemaker. Several probes were used along the tank to measure the wave surface elevation. Three experiments corresponding to three different JONSWAP spectra with different values of the Phillips parameter α and the peakedness γ (see (2.116)) were conducted. The main goal of these experiments was to give experimental support to the results of theoretical and numerical studies developed previously. According to these studies, it was suggested that the modulational instability was responsible for the occurrence of extreme wave events. The modulational instability or the Benjamin-Feir instability that was obtained for

uniform wave trains within the framework of deterministic approaches is assumed to work in random wave fields, too. Onorato et al. (2006b) showed that for long-crested water waves and large values of the Benjamin-Feir index, the second-order theory is not relevant to describe the tails of the probability density function of wave crests and wave heights. They showed that the probability of finding an extreme wave was underestimated by more than one order of magnitude if second order theory is considered, and found that the deviation was due to the modulational instability mechanism occurring for large BFI.

4.6 Three-Dimensional Rogue Waves

Until now, we have mainly paid attention to 2D aspect of the rogue wave formation. In this section, 3D aspects are discussed.

Rogue waves in the form of "walls of water" (see Fig. 1.2b) may potentially be described within the framework of 2D models (i.e., unidirectional wave propagation). At the same time, transversal effects are known to be important—for example, the NLS envelope soliton is transversally unstable. The localized "pyramidal" waves, like those in Fig. 1.2a,c, undoubtedly require consideration of the transverse wave direction. The geometrical focusing phenomenon may result from spreading waves. It is a linear mechanism of wave-energy focusing that was considered in Sect. 3.1. This primitive mechanism may be quite important in the real ocean, since papers report about higher probability of rogue wave occurrence in mixed seas.

Dispersive focusing is still efficient in 3D situations; and this kind of wave compression may be further enhanced by geometrical focusing (see Slunyaev et al. 2002). This results in more rapid and significant wave growth compared to the 2D case. If the dispersive wave train is far from the modulational instability threshold, the dispersive focusing prevails similarly to the linear case. The presence of random wave components may hide the deterministic process of rogue wave generation, but does not prevent the quasi-linear wave focusing as shown in Fig. 4.24. The rogue wave appears "from nowhere" and disappears at once.

Realistic fully nonlinear 3D simulations of directional wave focusing were conducted by Fochesato et al. (2007) (see Fig. 4.25). They found that the vertical 2D longitudinal cross section through an extreme wave crest looks quite similar to the characteristic shape frequently observed for rogue waves in the ocean: a tall and steep doubly asymmetric wave crest occurs in between two shallower troughs. The 3D wave generation yields a curved wave front before focusing occurs. A shallow circular trough forms in front of the focused wave ("hole in the sea"), followed by a deeper trough with a crescent shape. For a small time prior to breaking, the 3D shape of the focused wave appears to be almost pyramidal. By contrast, during the focusing phase, as well as the development of overturning, the transverse shape of the wave through the crest tends to have a more rounded shape. The problem of reproducing the desired 3D wave shapes in tanks was investigated by Bonnefoy et al. (2005).

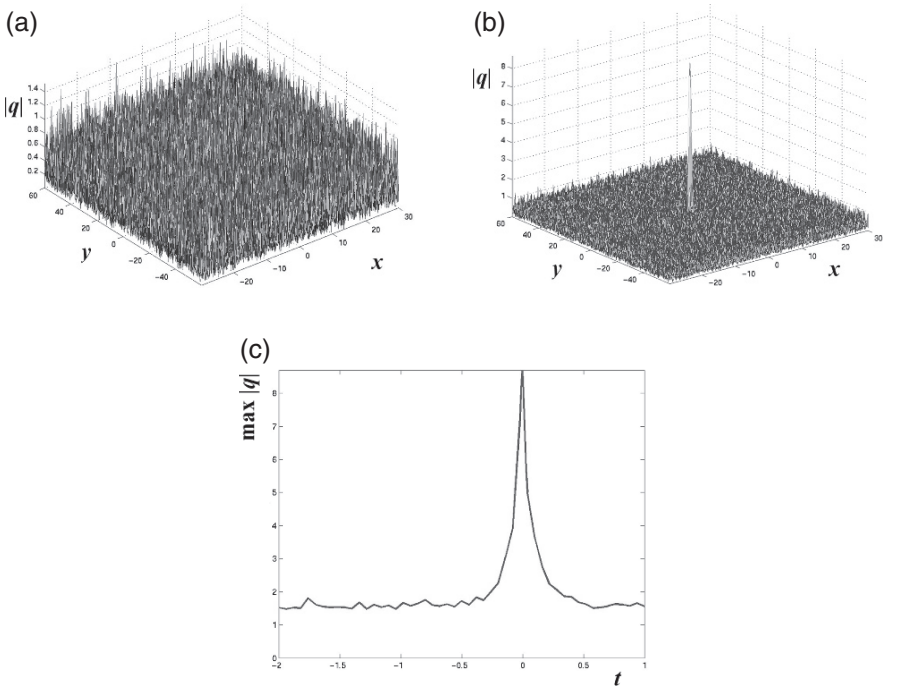

Fig. 4.24 Three-dimensional dispersive focusing of a wave train with modulated wavenumber in the presence of strong random wave components: (**a**) initial wave envelope, (**b**) moment of focusing, (**c**) record of maximum envelope amplitude versus time. Simulation within the framework of the NLS equation (see details in Pelinovsky et al. 2003)

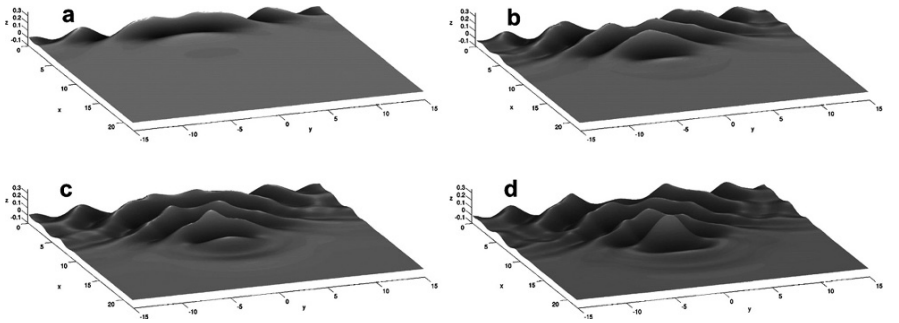

Fig. 4.25 Snapshots of 3D free surface evolution computed by Fochesato et al. (2007). The focused wave is starting to overturn in panel (**d**) (Reproduced with permission from Elsevier)

Johannessen and Swan (2001) extended the experimental investigation of Baldock et al. (1996) in 3D wave fields. They considered a laboratory study in which a large number of water waves of varying frequency and propagating in different directions, were focused at one point in space and time to generate a large wave event. Experiments were conducted in a basin located at Edinburg University. This facility has

a plan area of 24 m × 11 m and supports a constant working depth of 1.2 m. The water waves are generated by 75 numerically controlled wave paddles located along one of the longer sides of the wave tank. At the opposite end of the basin, a set of passive absorbers dissipates the incident wave energy. Different directional distributions are applied to the frequency spectra of the surface elevation. Johannessen and Swan (2001) showed that the directionality may have a profound impact effect upon the nonlinearity of a large wave event. When the sum of the wave amplitudes generated at the wave paddles is kept constant, an increase in the directional spread of the wave field results in lower maximum crest elevations. Conversely, when the generated wave amplitudes are increased until the onset of wave breaking, an increase in the directional spread allows larger extreme waves to evolve. The authors suggested that these results are due to the redistribution of the wave energy within the frequency domain. They emphasized the rapid widening of the free-wave regime in the vicinity of an extreme wave event, too.

In 2D (*XZ*) geometries, the modulational instability is strongly associated with the solitary solutions of the NLS equation (breathers or homoclinic orbits). These objects are conserved during the evolution due to the integrability property of the NLS equation. The 3D version of the NLS equation, as well as the Davey-Stewartson system[5] are nonintegrable. Therefore, the wave dynamics are more complicated for comprehension. For instance, the wave field, growing due to geometric or dispersive grouping but initially stable with respect to modulational instability, may then pass the threshold of nonlinear self-focusing and continue further enhancing due to nonlinearity. The Benjamin-Feir instability diagram (Fig. 4.1) provides a rich variety of unstable growing wave packets. Some shapes of 3D rogue waves spawned by modulational instability have been presented in the papers by Osborne et al. (2000) and Slunyaev et al. (2002), respectively. As an example, the 3D rogue wave given in Fig. 4.26d is more than seven times amplified with respect to the initial weakly modulated waves. The quasi 2D modulational instability (Fig. 4.26a,b) is followed by the strictly 3D modulational dynamics (Fig. 4.26c,d), which results in the formation of a huge wave isolated in both longitudinal and transversal directions. It is readily seen from Fig. 4.26e that the 3D rogue wave growth ($t \approx 4.1$) is more sudden and significant than the 2D dynamics ($t \approx 3$).

In water of infinite depth, it is well known that the 2D modulational instability is dominant for small to moderate initial steepness and evolves into a recurrence phenomenon (the Fermi-Pasta-Ulam recurrence) for small initial wave steepness (see Sect. 4.1.1). Another kind of disturbance suffered from 3D instabilities (see McLean 1982a,b) exists and becomes dominant for larger values of the steepness. This instability may lead to the formation of horseshoe patterns evolving into 3D spilling breakers. These three-dimensional patterns take the form of crescent-shaped perturbations riding on the basic waves. Three-dimensional horseshoe patterns were observed in experiments of Su et al. (1982) and Su (1982), Melville (1982), Kusuba and Mitsuyasu (1986, in presence of wind), and others.

[5] The DS system becomes integrable only in the shallow-water limit. In this case it does not show modulational instability.

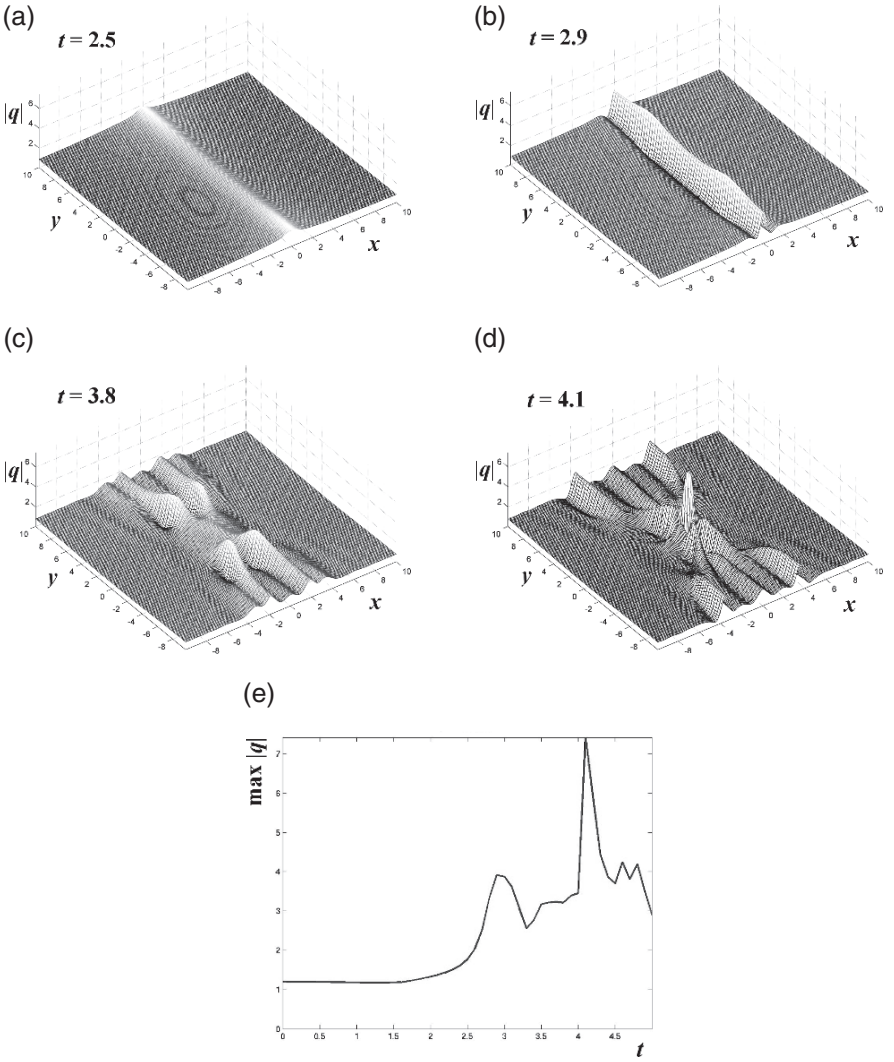

Fig. 4.26 Evolution of a weakly amplitude modulated plane wave within the framework of the NLS equation (see details in Slunyaev et al. 2002). Four snapshots of the envelope evolution (**a–d**) and the record of the maximum envelope amplitude versus time (**e**)

Generally, the two kinds of instability, namely the modulational instability and the crescent patterns that belong to class I and class II, respectively, coexist in the wave field. Depending on parameters such as the wave steepness of the initial Stokes wave and water depth, one can expect a competition to occur between the two classes of instability. Figure 4.27 illustrates the critical steepness together with the distinction between class I and class II dominances at the same depths. In the finite depth case, class II dominates in a large range of steepness and recurrence is

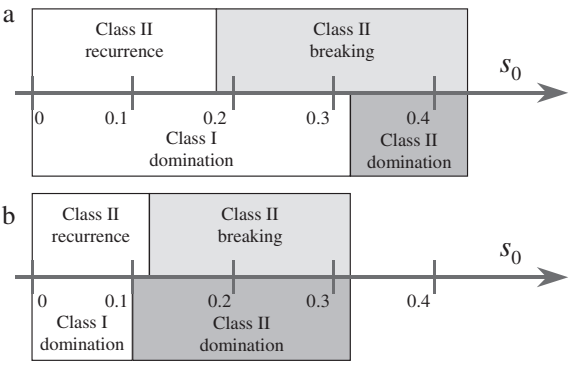

Fig. 4.27 Threshold steepnesses between class I and class II predominances and between class II recurrence and breaking: (**a**) the infinite depth case, (**b**) the finite depth case $K_0D = 1$

possible within this range. Note that for shallow water cases and relatively moderate steepness, instability of a plane Stokes wave is dominated by class II (Francius and Kharif 2006).

Numerical simulations by Fructus et al. (2005) and Kristiansen et al. (2005), taking into account both class I and class II instabilities, showed that for moderately steep waves ($s > 0.12$), their nonlinear coupling (involving the fundamental of the Stokes wave) results in breaking of the wave when in the initial condition only the modulational instability was considered. Furthermore, the breaking can occur for $s = 0.10$ when the initial unstable perturbation corresponds to the phase-locked crescent-shaped patterns. At the maximum amplitude of this instability, the modulational instability is excited followed by the breaking of the wave. For steeper waves, the strength of class II instability alone is sufficient to trigger the breaking of the wave. The nonlinear dynamics of the most unstable class II perturbation leads to breaking when $s > 0.17$ (see Fig. 4.27a).

Annenkov and Badulin (2001) selected the specific component peculiar to five-wave interactions in the frequency spectrum of the 20 min New Year Wave record. This component corresponds to class II instabilities phase-locked to the dominant component of the spectrum. In order to have a better understanding of the role of this kind of resonance in the formation of rogue waves, the authors performed numerical simulations of the Zakharov equation, which takes into account the modulational (which is a four-wave interaction) and five-wave interactions. Annenkov and Badulin (2001) showed that the cooperative effects of these interactions might be responsible for the occurrence of rogue waves and emphasize the role of oblique waves in this process.

Ruban (2007) investigated a weakly 3D evolution of modulationaly unstable wave patterns by means of fully nonlinear simulation and observed "zigzag patterns" with extreme waves in their turns formed during instability development. Recurrent dynamics of 3D wave patterns over deep and finite depth were simulated in recent papers (Kristiansen et al. 2005, Fructus et al. 2005) and are shown in Figs. 4.28 and 4.29, respectively. In the real sea, the hydrodynamic instability appears at the center of the crescent patterns when the wave steepness is above a threshold value.

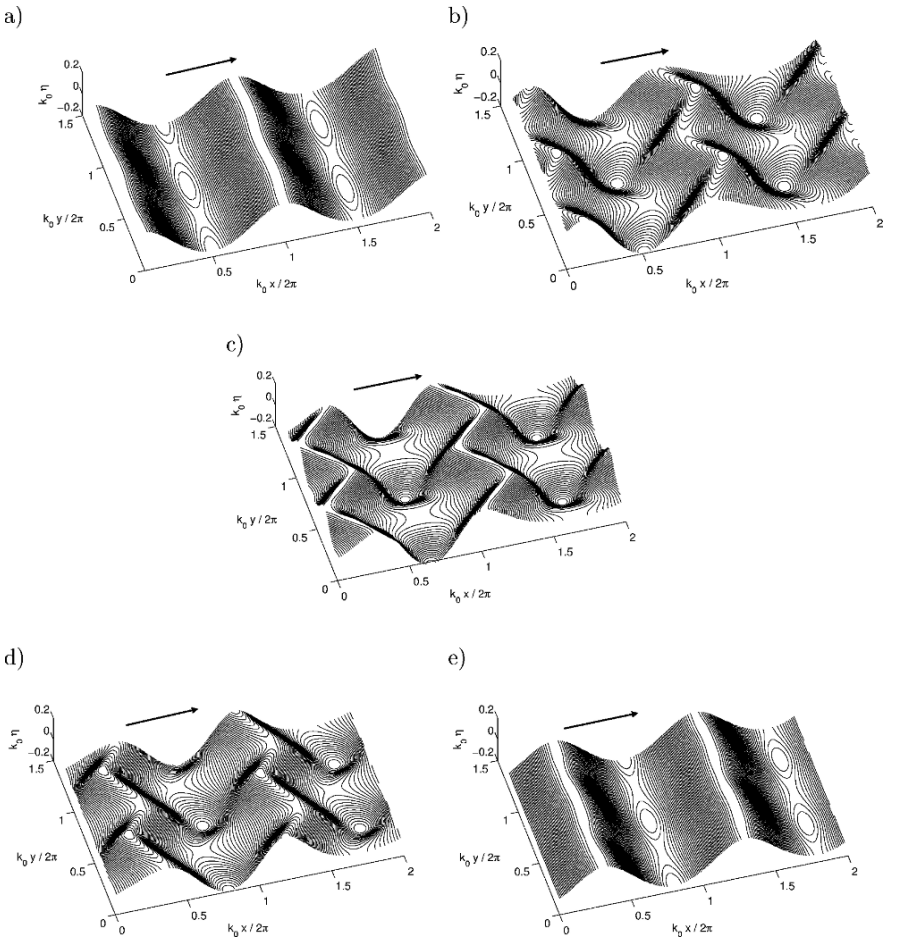

Fig. 4.28 Temporal evolution of the surface elevation during a recurrence cycle, fully nonlinear simulation of Kristiansen et al. (2005). The infinite depth case (Reproduced with permission from American Institute of Physics)

Recent findings of Gramstad and Trulsen (2007) by means of numerical simulation of the extended Dysthe equation show a conspicuous qualitative difference between the extreme wave dynamics in long- and short-crested seas. The paper reports about weak deviation of extreme waves from the Gaussian statistics when short crest lengths are concerned. On the other hand, the long crest wave statistics of freak waves is strongly non-Gaussian, and the Benjamin-Feir instability seems responsible for rogue wave formation. These results qualitatively agree with the predictions of Onorato et al. (2002, with extended Dysthe equations), Shukla et al. (2006, with coupled NLS equations) and Gibson et al. (2007) but appear to be conflicting with the studies of unstable crested waves by Onorato et al. (2006a, with coupled NLS

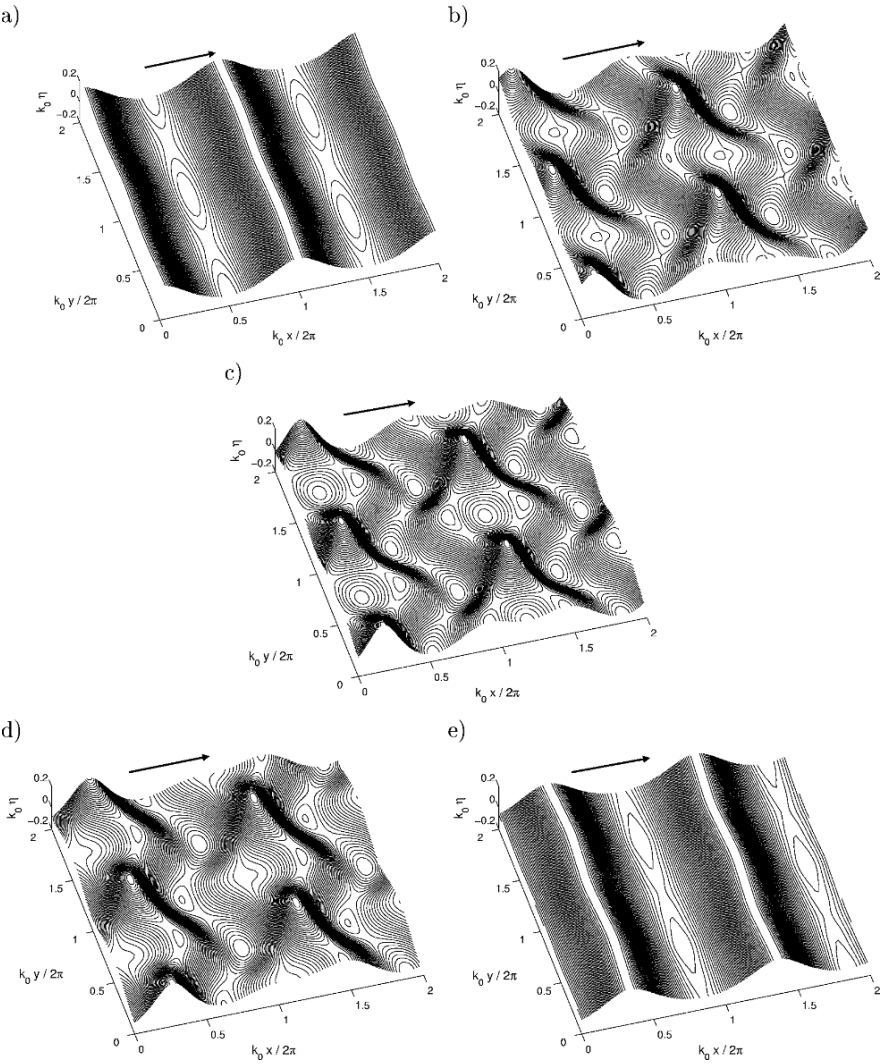

Fig. 4.29 Temporal evolution of the surface elevation during a recurrence cycle, fully nonlinear simulation of Kristiansen et al. (2005). The finite depth case $K_0D = 1$

equations), fully nonlinear simulations of Ducrozet et al. (2007), and some natural observations (Pinho et al. 2004, Scott et al. 2005).

Although the real ocean is not homogeneous nor stationary, it was suggested by Haver (2005) and Gibson et al. (2007) that in seas of short-crested waves, some long-crested sub areas may exist in principle, which provides conditions for the high probability of the rogue wave occurrence.

Using the data collected from 1995 to 1999 by Lloyd's Marine Information Service, Toffoli et al. (2004) showed that a large percentage of ship accidents due to bad

Fig. 4.30 Pyramidal waves observed by Kimmoun et al. (1999) in a laboratory tank

weather conditions occurred in crossing sea states. Crossing sea sates are characterized by two dominant spectral peaks, and may be due to the interaction between a swell and a wind-wave sea coming from a different direction. This feature was also observed in the New Year Wave record. Onorato et al. (2006a) considered a weakly nonlinear model that describes the interaction of two-wave systems in deep water with two different directions of propagation. Under the assumption of narrow-band wave fields, they derived two coupled NLS equations from the Zakharov equation. As a main result, they showed that given a single unstable plane wave, the introduction of a second plane wave traveling in a different direction can increase the instability growth rates and enlarge the instability region. From their simple model, they suggested that the modulational instability could explain the formation of rogue wave events in crossing sea states. For more details concerning the stability of short-crested gravity waves due to the nonlinear interaction between two plane waves propagating in two different directions, see the papers by Ioualalen and Kharif (1994) and Badulin et al. (1995). These numerical and theoretical investigations on short-crested waves were followed by an experimental study conducted by Kimmoun et al. (1999) who observed pyramidal waves (see Fig. 4.30).

4.7 In Situ Rogue Waves

A great deal of theoretical investigations aimed at solving the rogue-wave phenomenon has been undertaken. Although some of the suggested physical mechanisms explain the occurrence of rogue waves rather well, the natural mechanisms that spawn rogue waves observed in the real ocean still need investigation. Instru-

mental measurements are the best source of getting information about real sea wave dynamics. The state-of-art in instrumental registrations is discussed in Sect. 1.2. Many registrations correspond to the case of deep or moderately deep water, but still are made in very different conditions throughout long periods of time. This makes direct statistical analysis quite hard or impossible. Some recent results of these statistical studies are given in Sect. 4.7.2. Section 4.7.1 is devoted to the analysis of the instrumental records themselves, trying to find out most possible information from "traces" of rogue waves.

4.7.1 Nonlinear Analysis of Measured Rogue Wave Time Series

4.7.1.1 Local Parameters

Local wave parameters may be used to reveal peculiar properties of measured rogue waves within the field of usual oceanic waves. To do this, shorter overlapping time intervals are extracted from the record. This procedure is known as Gabor or "windowing" transform. To reduce possible spurious effects due to the discontinuity of the time series at the boundaries, the Hanning data mask may be applied (Massel 1996). Examples of some local parameter estimations are given in Figs. 4.31 and 4.32 for two time series measured at the North Alwyn platform in the North Sea (see details in Slunyaev et al. 2005, Slunyaev 2006). The platform conditions correspond to sufficiently deep water ($KD > 3.6$), therefore we will restrict ourselves to the infinite depth approximation.

The mean frequency Ω is obtained as the spectral moment (2.109), Ω_p. The unfavorable result of considering a shorter time series gives a worse accuracy in statistical estimations and in particular the spectrum and all spectral parameters. The carrier frequency curves are given in Figs. 4.31 and 4.32 on panels A and B (the solid white line on the background of the Fourier time-frequency spectra) for two different durations of the sampling window T_{win}. One can observe some variations during the 20-min record, which become more evident if expressed in terms of group velocity C_{gr} (see Figs. 4.31D and 4.32D). The group velocity is obtained through the linear dispersion relation, since the measurement is available in only one point. The deviation of the group velocities observed in these cases is about 50%; it leads to the energy exchange between the individual waves. This may provide the wave growth or decrease and represents the simplest case of dispersive focusing. For a simple analysis of this process, the kinematic theory (3.13) may be used accompanied by the energy balance equation (3.5) (see Chap. 3):

$$\frac{\partial C_{gr}}{\partial T} + C_{gr}\frac{\partial C_{gr}}{\partial X} = 0, \qquad \frac{\partial \eta^2}{\partial T} + \frac{\partial}{\partial X}\left(C_{gr}\eta^2\right) = 0 \tag{4.116}$$

where $\eta(X,T)$ is the surface elevation.

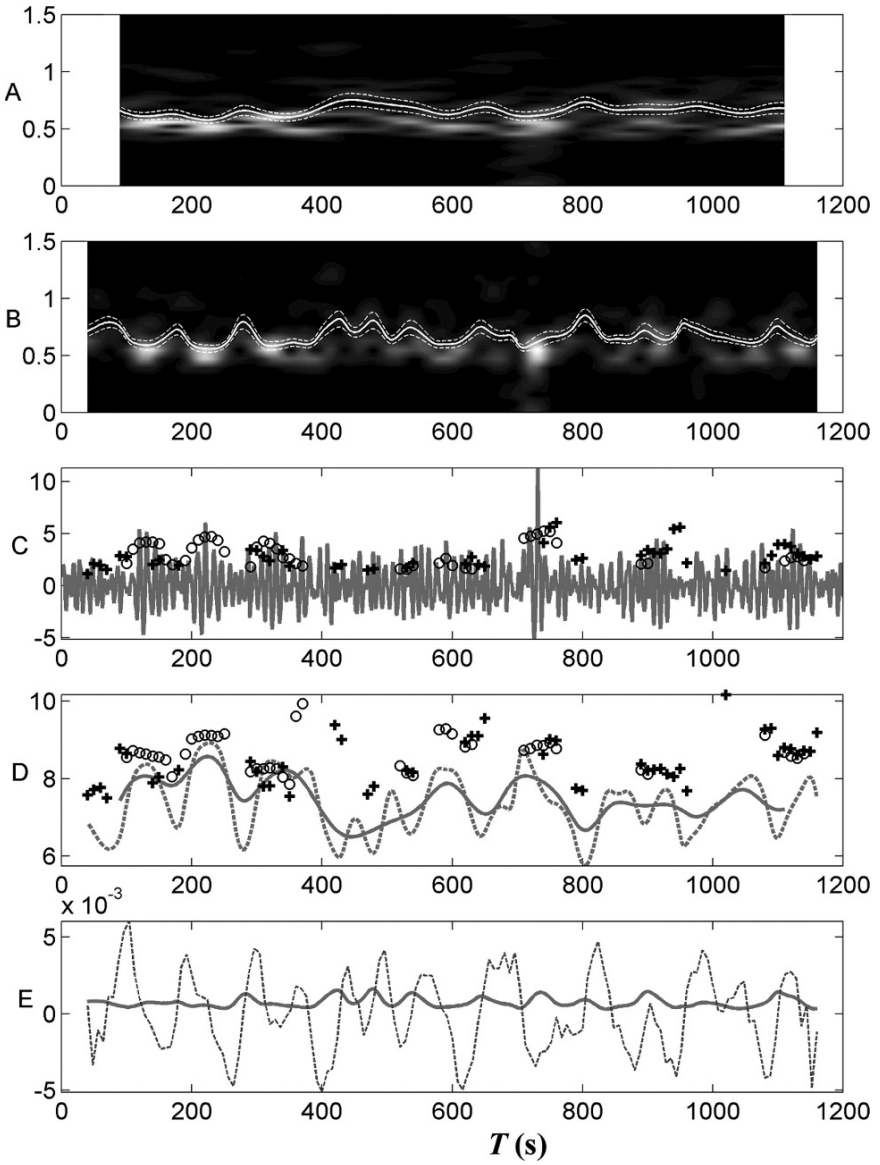

Fig. 4.31 Wave record made at the North Alwyn platform on November 18th, 1997 at 01:10. (**A**) Time-Frequency Fourier spectrum built for the sampling window of 117 s duration (about 10 wave periods); solid line shows the local mean frequency Ω, dashed lines bound the domain of Benjamin-Feir instability $\Omega \pm \Delta\Omega_{BF}$. **B**) The same as on panel A, but for the sampling window of 36 s duration (3 wave periods). **C**) Measured time series of the surface displacement (in meters). Symbols denote the determined amplitudes of solitary waves with permanent normalizing (*circles*) and flexible normalizing (*crosses*). **D**) Local group velocities (in m/s) defined for the sampling window of 117 s (*solid line*) and 36 s (*dashes*). Symbols denote the determined velocities of solitary waves: permanent normalizing (*circles*) and flexible normalizing (*crosses*). **E**) Growth rates $\sigma_{BF\,max}$ (*solid*) and σ_{dis} (*dashed*) (in s^{-1}) defined with the sampling window of 36 s

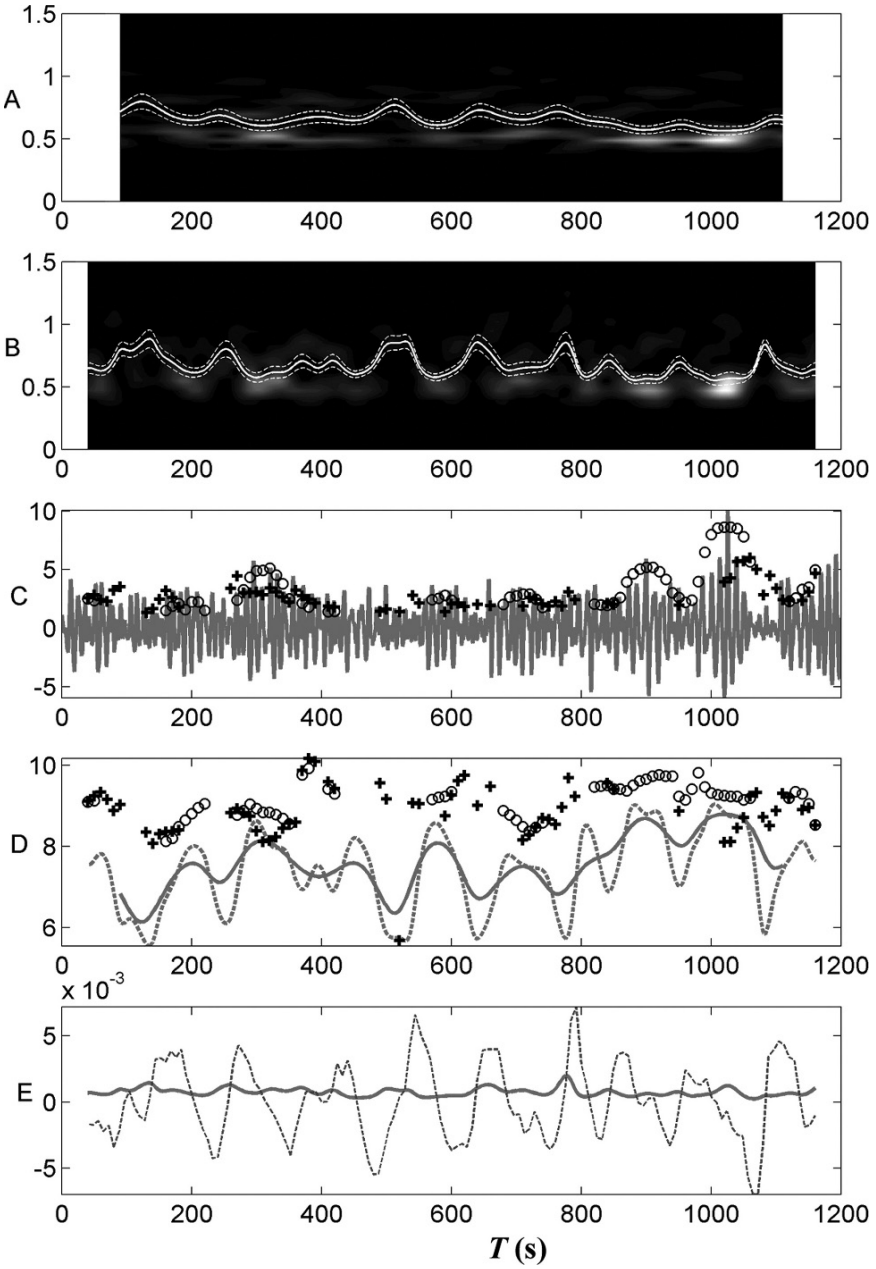

Fig. 4.32 Wave record made at North Alwyn platform on November 19th 1997 at 20:11. The legend is same as in Fig. 4.31

Then the total derivative of the energy quantity is given by:

$$\frac{d\eta^2}{dT} = 2\sigma_{dis}\eta^2, \quad \text{where} \quad \sigma_{dis} = \frac{1}{2C_{gr}}\frac{\partial C_{gr}}{\partial T}. \tag{4.117}$$

Parameter σ_{dis} expresses the exponential growth rate due to dispersive wave convergence. Waves grow when $\sigma_{dis} > 0$ and decay for $\sigma_{dis} < 0$. The dispersive growth rates computed for the time series are given in Figs. 4.31 and 4.32 (panel E, dashed lines).

4.7.1.2 Application of the IST Approach

The simple nonlinear theory is based on the NLS equation (4.35) under the extra assumption of unidirectional wave propagation. The spatial version of the dimensionless NLS equation has the form

$$iq_x + q_{tt} + 2q|q|^2 = 0, \tag{4.118}$$

where

$$t = \Omega_0 T - 2K_0 X,\ x = K_0 X,\ q = \frac{1}{\sqrt{2}} K_0 A^*, \tag{4.119}$$

and $A \equiv \eta_{01}$ is the complex envelope amplitude (see Eqs. (4.11), (4.13)). The spectral areas that are unstable with respect to long perturbations of the uniform Stokes waves may be estimated as the domain $(\Omega - \Delta\Omega_{BF}, \Omega + \Delta\Omega_{BF})$, where $\Delta\Omega_{BF}$ is defined with the help of the instability criterion (4.39) and deep-water dispersion relation as

$$2\frac{\Delta\Omega_{BF}}{\Omega} = \frac{\Delta K_{BF}}{K} < 2\sqrt{2}K\eta. \tag{4.120}$$

The unstable frequency domain $\Omega_0 \pm \Delta\Omega_{BF}$ is bounded by the dashed lines in Figs. 4.31 and 4.32 (panels A, B). The initial stage of the modulational growth is described by the exponential law with a maximum growth rate given by formula (4.41), which is, in the deep-water case,

$$\sigma_{BF_{\max}} = \frac{1}{2}\Omega K^2 \eta^2. \tag{4.121}$$

The two growth rates σ_{dis} and σ_{BFmax} (see Figs. 4.31 and 4.32, panels E) are used for rough estimates of the time scales of dispersive and nonlinear wave focusing effects. It is seen from the figures that dispersion typically works faster, while estimated modulational growth should take more than 500 s.

The nonlinearity of individual waves is characterized by the steepness, although the strength of self-focusing is characterized by another nonlinear parameter, which is the soliton number or the BFI (see Sects. 4.2 and 4.4). The "dynamical" definition of BFI (4.112) includes the number of individual waves observed in the wave group n_t. The number of waves within a packet is actually a convenient dimensionless parameter, and is often used for estimations.

Since the modulational instability occurrence is related to the homoclinic orbits, "unstable modes," or envelope solitons (see Sect. 4.2), a more accurate way to estimate the features of the modulational instability may be suggested by employing the concept of the envelope soliton. The envelope soliton of the NLS equation may be considered as the first approximation for oceanic solitary wave groups. Results reported in Sect. 4.3.5 concerning the steep NLS soliton-like envelopes, justify the adequacy of the quasi-soliton concept even in strongly nonlinear cases. For the equation in the form (4.118), the envelope soliton solution (4.60) is rewritten as

$$q_{es}(x,t) = A_{es} \frac{\exp\left(\dfrac{i(t-t_0)}{2V_{es}} - ix\left(\dfrac{1}{4V_{es}^2} - A_{es}^2\right) + i\theta_0\right)}{\cosh\dfrac{A_{es}}{V_{es}}\left(x - x_0 - V_{es}(t-t_0)\right)}, \tag{4.122}$$

where the parameters t_0 and θ_0 are explicitly introduced, which are the time shift at position $x = 0$, and the initial phase. In Eq. (4.122), A_{es} and V_{es} are a dimensionless amplitude and velocity of the envelope soliton, respectively. The physical parameters, the amplitude of the wave packet A_{wp}, and its velocity V_{wp} are expressed as

$$A_{wp} = \frac{\sqrt{2}}{K_0} A_{es}, \quad V_{wp} = \frac{\Omega_0}{K_0\left(2 + V_{es}^{-1}\right)}. \tag{4.123}$$

The applicability of the NLS theory (spectral narrowness) requires the quantity $|V_{es}^{-1}|$ being small.

When envelope solitons interact with other waves, the dynamics of the wave field may become complex. The possibility of detecting hidden solitons in time series may provide an effective tool in understanding and predicting nonlinear wave dynamics. This can be done with the help of the Inverse Scattering Technique (see Sect. 4.2.1). The spectrum of the scattering problem is time independent, and its discrete part corresponds to envelope solitons. Let us consider the scattering problem (4.59) for the infinite line; then the soliton parameters are simply related to the spectrum as follows

$$A_{es} = 2\,\mathrm{Re}\lambda \quad \text{and} \quad V_{es}^{-1} = 4\,\mathrm{Im}\lambda \tag{4.124}$$

instead of (4.67). The complete solution of the inverse scattering problem for function $q(x = 0,\ t)$—i.e. determination of t_0 and θ_0—requires knowledge of the eigenmodes. The parameter t_0, which defines the position of the envelope soliton in the time series, may be well localized if short overlapping extracts from the time series are considered (employing the windowing transform). Thus, the direct scattering problem is solved in a sliding sampling window of length t_{win} that identifies the position t_0 of solitons. If wave groups of large amplitude are of interest, the window t_{win} is bounded owing to the conservation of the mass parameter M_{es} (4.69) for the envelope solitons (i.e., steep solitons are narrow).

It is necessary to define the carrier wave frequency when considering the NLS equation (4.118). Panels A in Figs. 4.31 and 4.32 show its variation. Therefore, to follow the variation of the frequency, a short window should be used. On the

other hand, it is more difficult to obtain a reliable estimate of this value within a short window, preserving only few wave periods. The number of envelope solitons is governed by the mass parameter, as Eq. (4.64). In the case of the spatial version of the NLS equation (4.118), the following estimate may be done

$$N_s \propto K_0 \Omega_0 \propto \Omega_0^3, \tag{4.125}$$

where the deep-water dispersion relation is used. Therefore, accurate determination of the carrier wave frequency may be crucial for this method.

The soliton amplitudes that have been obtained with the help of this approach are plotted as circles and crosses on panel C of Figs. 4.31 and 4.32. The corresponding soliton velocities are given on panel D. The mean frequency is defined via two methods. First, it is defined as the spectral moment Ω_p (2.109) of the whole 20-min record ("permanent normalization"), and second, as the spectral moment of each short extract ("flexible normalization"). These cases correspond to circles and crosses in the figures. It is evidently seen that sometimes the results are rather different. After having a look at the curves of the group velocity (panel D), it becomes clear that a soliton vanishes if the mean group velocity increases. The effect of non-uniformity on modulated wave packets was considered by Duin (1999) with the same qualitative conclusion: the BF instability is depressed when the local group velocity increases and is intensified when C_{gr} becomes smaller.

Only the first (steeper) solitons defined in extracts are shown in the figures. Other solitons are usually much smaller and assumed not to be very trustworthy. Although the found solitons can often be seen by eye, they interact nonlinearly with other waves, and in other conditions may be hidden by the surrounding waves.

The idea to seek solitons in a time series was, evidently, first realized by Osborne and Petti (1994) for the shallow-water case, when the waves were described within the framework of the Korteweg-de Vries equation. Recently, a similar technique has been used for the study of freak waves over deep water within the NLS approach (Osborne et al. 2005, Islas and Schober 2005, Schober and Calini 2008). In contrast to the previous description, they suggest the use of periodic domains and the determination of the eigenmodes (full reconstruction of unstable modes). This makes the approach more difficult when employing the theta-functions, whereas applying the infinite line scattering problem formulation admits the description of wave groups with the help of breathing solutions considered in Sect. 4.2.3.

To estimate the contribution of the solitary part in the observed freak waves, let us assume a rogue wave is the result of the interaction of an envelope soliton with a plane wave. Then the "solitary part" is defined as A_{wp}/A_{fr}, where A_{wp} is the detected amplitude of the soliton (4.123), and A_{fr} is the Hilbert envelope amplitude including the freak wave obtained directly from the time series. The contribution of the background waves is estimated as $H_s/(2A_{fr})$. According to the analysis provided in Sect. 4.2.3, these contributions linearly supplement each other as Eq. (4.75). They are represented by the solid and hatched areas in Fig. 4.33, respectively. Eleven analyzed rogue waves measured at oil platforms in the North Sea are used in the figure. The rest (the empty areas) estimates the effects that are not taken into account. It may be noticed that the first two contributions (the solitary part and the significant background) may often completely explain the registered wave amplitude; this obvi-

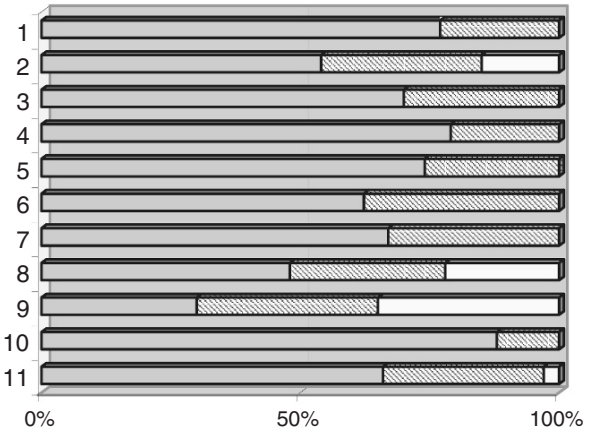

Fig. 4.33 "Solitary parts" A_s (*solid*) and $H_s/2$ (*hatched*) of the freak wave amplitudes for 10 records from the North Alwyn platform and the New Year Wave

ously proves the important role of the nonlinear modulation effect in the freak-wave occurrence.

The application of the IST method to the analysis of water wave groups may be improved by use of the Creamer et al. (1989) transform that takes into account the nonlinear bound corrections that are not described by the NLS envelope equation. Higher-order integrable (or nearly integrable) versions of the envelope equation may be employed to describe more accurately the envelope solitary solutions (Schober and Calini 2008).

In the present analysis, we have employed the window Fourier transform to determine the wave frequency. Wavelets provide an alternative improved way to estimate the mean wave scale. They have been used by various authors: among them we cite Mori et al. (2002), Chien et al. (2002), Paprota et al. (2003), Scott et al. (2005). These studies present different occurrences of rogue waves in wavelet planes. Chien et al. (2002) distinguish freak waves generated by wind waves (unimodal spectrum with strong grouping phenomenon) and bimodal waves caused by interaction of two wave systems (say, wind waves and swell). There also exist a large amount of multimodal waves that have many energetic areas in the wavelet spectrum. Although the wavelet analysis may catch the transient change of wave parameters better than the Fourier transform, the wavelet spectra are more difficult to interpret. The shapes of the prototype functions ("mother wavelets") are often very similar (or identical) to the NLS envelope soliton, hence the application of the IST analysis in combination with the exact theory may prove to be very efficient.

The three-dimensionality of rogue waves can help to identify their origin, as is discussed in Sect. 4.6. Although the development of air-, ship- and satellite-borne SAR measurements and the associated methods of analysis are very promising (see Rosenthal 2005), until now there have been very few results concerning 3D observations. It needs further improvement and justification to enable regular measurements and analysis (see Dysthe et al. 2008).

4.7.2 Statistics from Registrations of Natural Rogue Waves

Most available long-run instrumental registrations are made over relatively deep-water areas (see Fig. 1.3). Although the number of measured rogue waves is in the hundreds, these waves are measured under very different conditions and obviously do not satisfy the stationary random process requirement. That is why the results of their statistical analysis are often dubious. This doubt is indirectly confirmed by conflicting conclusions of different investigations about the probability of highest waves registered by gauges. Rogue waves are found to occur much more frequently than is foreseen by the Rayleigh distribution function in studies (Mori 2004, Pinho et al. 2004, Stansell 2004, Liu and MacHutchon 2006). This distribution, however, fits natural data reported quite well in Mori et al. (2002). The freak wave phenomenon is rarer than it follows from the Rayleigh distribution function according to Chien et al. 2002, Paprota et al. 2003, both for relatively shallow water). Stansell (2004) has undertaken a careful analysis of the records from the viewpoint of statistical stationarity, and reported on about 300 times more frequent occurrence of the highest measured wave ($AI = 3.19$) than it could be expected from the Reyleigh statistics. Similar estimates may be found in the paper by Mori and Janssen (2006a). Although some theoretical relations are suggested by the authors to describe the results, the general disagreement between the results about the rogue-wave probability obviously makes the conclusions about the quantitative rogue-wave probability estimation premature. Thus, the present database of rogue waves cannot answer the question about the true probability of rogue waves. The more or less accepted opinion about the statistical description of observed extreme waves is as follows: the high-order statistical models in general are able to describe many huge waves, although a population exists of "true rogue waves" that do not satisfy the classical statistical description.

It has already been discussed that the scientific community tries to fill in the lack of in situ data by numerical data obtained from computational runs. To do this, it is necessary to ensure that the dynamics described by the computer models are similar to real ocean dynamics. The main result achieved through the numerical simulations of irregular surface waves consists of an increase of the rogue wave probability when the Benjamin-Feir index grows. Hence, this parameter has been considered as a possible good indicator of high probability of freak-wave occurrence. Therefore, the first question that should be answered is: does the probability of extreme sea-waves exhibit a dependence on the BFI? The answer is actually not straightforward. The BFI seems to be a promising parameter for evaluating the danger of extreme sea waves. As it was demonstrated by numerical simulation, a strong correlation exists between high wave probability and BFI. Nevertheless, its practical use seems to be still not fully operational. The BFI is a complex parameter, roughly speaking, reflecting the typical wave height (or corresponding dimensionless parameter, "steepness") and spectral bandwidth (or number of waves in a group, which is the inverse value) (see Sect. 4.4). Surprisingly, it is found that the probability of occurrence of freak waves is only weakly dependent on the significant wave height, significant wave steepness, and spectral bandwidth (Stansell 2004, Olagnon and Prevosto 2005, Olagnon and Prevosto 2005). Furthermore, Melville et al. (2005)

remark that the threshold in the abnormality index, *AI*, does not correspond to equivalent thresholds in either the skewness or excess kurtosis.

In order to confirm the adequacy of a selected parameter to be used in warnings of risk occurrence, it is necessary to ensure that it is sensitive to the presence of rogue waves, and that it can be robustly computed. Olagnon and Magnusson (2004, 2005) note that the BF indices (defined in Olagnon and Magnusson 2004 in different ways) and the peakedness factor of the JONSWAP spectrum exhibit particularly poor robustness. High natural variability of the BF index might be a consequence of the difficulty to obtain stable estimators when considering short in situ records.

The investigation of the robustness of some popular statistical parameters (wave height, crest height, period, steepness, kurtosis, BFI, parameters of the spectral shape) performed by Olagnon and Magnusson (2004) reports that only the kurtosis exhibits a sufficient correlation with normalized crest height to allow considering it as a parameter to be monitored. However, the kurtosis is directly influenced by the presence of extreme waves. We should emphasize here that from the theoretical point of view the kurtosis and the BFI are related through Eq. (4.108).

From a practical viewpoint, a parameter must vary on a characteristic time scale significantly larger than the wave period. Otherwise, the variation of the parameter will merely be a detector of the rogue wave and cannot be used for forecasting. Olagnon and Prevosto (2005) report that the change of the kurtosis value registered at the instant of a high wave occurrence can be satisfactorily explained by the high wave alone, and that no further relationship can be found at larger time scales. If the maximum wave is removed from the kurtosis computation, and kurtosis is estimated from the remaining of the record, no further correlation between the kurtosis and the maximum wave height can be seen. Therefore, Olagnon and Prevosto (2005) conclude that the Benjamin-Feir instability is very local and is not reflected by statistics at the time scale of a sea state. The deviations that they could observe for some spectral parameters close to occurrences of extreme waves were well within the natural range of variability. They could not identify any special feature on the time-histories of the BFI that might have some chance of being related to rogue wave occurrence.

A possible explanation of the discrepancy between numerical studies and natural observations may be due to the typically unidirectional wave propagation (long-crested waves) studied in the majority of the numerical computations, while the natural sea waves are essentially short-crested. The evidence of two qualitatively different sea wave regimes (long- and short-crested) that result in very different statistics is formulated in recent papers (Haver 2005, Gramstad and Trulsen 2007, Dysthe et al. 2008) (see Sect. 4.6), and is becoming supported by theoretical studies and numerical simulations as well. These studies will obviously guide the focus of future research.

List of Notations

A	amplification factor
A	wave amplitude
A_{br}	amplitude of the breather

A_{es}	amplitude of the envelope soliton
A_{pw}	amplitude of the plane wave
A_{wp}	dimensional amplitude of the wave packet
AI	abnormality index
C_{gr}	group velocity
C_{LW}	long wave velocity
C_{ph}	phase velocity
d	dimensionless water depth
$\tilde{d}$	depth parameter
D	water depth
D/DT	material derivative
g	acceleration due to gravity
H	wave height
H_s	significant wave height
I_{BF}	Benjamin-Feir index
$\mathbf{k} = (p,q)$	dimensionless wave vector
$\mathbf{K} = (K_X, K_Y)$	wave vector
K	wavenumber
M	mass integral
M	order of perturbation series in the HOSM approach
$\mathbf{n}$	unit vector normal to the boundary
n_t, n_x	number of individual wave in the time series or wave snapshot
N_s	soliton number
p	dimensionless pressure
p_a	dimensionless atmosphere pressure
P	pressure
P_a	atmosphere pressure
$q(x,t)$	dimensionless envelope amplitude in the NLS equation
s	wave steepness
t	dimensionless time
T	time
T_{br}	period of the breather
T_f	focusing time
U_w	wind velocity
V_{br}	velocity of the breather
V_{es}	velocity of the envelope soliton
V_{wp}	dimensional velocity of the wave packet
(x, y, z)	dimensionless coordinates
(X, Y, Z)	coordinates
X_f	focusing length
$\phi(X, Y, Z, T)$	velocity potential
$\eta(X, Y, T)$	surface elevation
$\varphi(x, y, z, t)$	dimensionless velocity potential
κ	kurtosis
λ	eigenvalue of the associated scattering problem
ρ_a	atmosphere density

σ	growth rate
σ	standard deviation, σ^2 is the variance
Ω	cyclic wave frequency
Ω_p	mean wave frequency
$\zeta(x, y, t)$	dimensionless surface displacement
$\partial\Omega_{FS}$	free surface
$\partial\Omega_{SB}$	solid boundaries
∇	gradient operator

List of Acronyms

BF	Benjamin-Feir
BFI	Benjamin-Feir Index
BIEM	Boundary Integral Equation Method
DS	Davey-Stewartson system
HOSM	High Order Spectral Method
NLS	Nonlinear Schrödinger equation
SWE	Steep Wave Event

References

Ablowitz MJ, Hammack J, Henderson D, Schober CM (2000) Modulated periodic Stokes waves in deep water. Phys Rev Lett 84:887–890

Ablowitz MJ, Hammack J, Henderson D, Schober CM (2001) Long-time dynamics of the modulational instability of deep water waves. Phys D 152–153:416–433

Ablowitz MJ, Herbst BM (1990) On homoclinic structure and numerically induced chaos for the Nonlinear Schrödinger equation. SIAM J Appl Math 50:339–351

Ablowitz MJ, Kaup DJ, Newell AC, Segur H (1974) The inverse scattering transform – Fourier analysis for nonlinear problems. Stud Appl Math 53:249–315

Ablowitz MJ, Segur H (1979) On the evolution of packets of water waves. J Fluid Mech 92:691–715

Akhmediev NN, Ankiewicz A (1997) Solitons. Nonlinear pulses and beams. Chapman & Hall, Florida

Akhmediev NN, Eleonskii VM, Kulagin NE (1985) Generation of periodic trains of picosecond pulses in an optical fiber: exact solutions. Sov Phys J Exp Theor Phys 62:894–899

Akhmediev NN, Eleonskii VM, Kulagin NE (1987) Exact first-order solutions of the nonlinear Schrödinger equation. Theor Math Phys (USSR) 72:809–818

Alber IE (1978) The effects of randomness on the stability of two-dimensional surface wavetrain. Proc Roy Soc Lond A 363:525–546

Alber IE, Saffman PG (1978) Stability of random nonlinear water waves with finite bandwidth spectra. TRW Def and Space Syst Group Rep No 31326-6035-RU-00bv

Annenkov SYu, Badulin SI (2001) Multi-wave resonances and formation of high-amplitude waves in the ocean. In: Olagnon M, Athanassoulis GA (eds) Rogue Waves 2000, Ifremer, France, pp 205–213

Badulin SI, Shrira VI, Kharif C, Ioualalen M (1995) On two approaches to the problem of instability of short-crested water waves. J Fluid Mech 303:297–326

Baldock TE, Swan C, Taylor PH (1996) A laboratory study of nonlinear surface waves on water. Phil Trans Roy Soc Lond A 354:649–676
Banner ML, Song J (2002) On determining the onset and strength of breaking for deep water waves. Part II: Influence of wind forcing and surface shear. J Phys Oceanogr 32:2559–2570
Banner ML, Tian X (1998) On the determination of the onset of breaking for modulating surface gravity water waves. J Fluid Mech 367:107–137
Bateman WJD, Swan C, Taylor PH (2001) On the efficient numerical simulation of directionally spread surface water waves. J Comput Phys 174:277–305
Benjamin TB, Feir JE (1967) The desintegration of wave trains on deep water. Part 1. Theory. J Fluid Mech 27:417–430
Benney DJ, Roskes GJ (1969) Wave instabilities. Stud Appl Math 48:377–385
Bliven LF, Huang NE, Long SR (1986) Experimental study of the influence of wind on Benjamin-Feir sideband instability. J Fluid Mech 162:237–260
Bonnefoy F, de Reilhac PR, Le Touzé D, Ferrant P (2005) Numerical and physical experiments of wave focusing in short-crested seas. In: Proc. 14th Aha Huliko'a Winter Workshop, Honolulu, Hawaii, 2005
Burzlaff J (1988) The soliton number of optical soliton bound states for two special families of input pulses. J Phys A: Math Gen 21:561–566
Calini A, Schober CM (2002) Homoclinic chaos increases the likelihood of rogue wave formation. Phys Lett A 298:335–349
Caponi EA, Saffman PG, Yuen HC (1982) Instability and confined chaos in a nonlinear dispersive wave system. Phys Fluids 25:2159–2166
Chien H, Kao C-C, Chuang LZH (2002) On the characteristics of observed coastal freak waves. Coast Eng J 44:301–319
Clamond D, Francius M, Grue J, Kharif C (2006) Long time interaction of envelope solitons and freak wave formations. Eur J Mech B/Fluids 25:536–553
Clamond D, Grue J (2001) A fast method for fully nonlinear water-wave computations. J Fluid Mech 447:337–355
Clamond D, Grue J (2002) Interaction between envelope solitons as a model for freak wave formations. Pt. 1: Long time interaction. C R Mecanique 330:575–580
Clarke S, Grimshaw R, Miller P, Pelinovsky E, Talipova T (2000) On the generation of solitons and breathers in the modified Korteweg – de Vries equation. Chaos 10:383–392
Crawford DR, Saffman PG, Yuen HC (1980) Evolution of a random inhomogeneous field of nonlinear deep-water gravity waves. Wave Motion 2:1–16
Creamer DB, Henyey F, Schult R, Wright J (1989) Improved linear representation of ocean surface waves. J Fluid Mech 205:135–161
Davey A, Stewartson K (1974) On the three-dimensional packets of surface waves. Proc Roy Soc Lond A 338:101–110
Desaix M, Anderson D, Lisak M, Quiroga-Teixeiro ML (1996) Variationally obtained approximate eigenvalues of the Zakharov-Shabat scattering problem for real potentials. Phys Lett A 212:332–338
Dhar AK, Das KP (1991) Fourth-order nonlinear evolution equation for two Stokes wave trains in deep water. Phys Fluids A 3(12):3021–3026
Dias F, Kharif C (1999) Nonlinear gravity and capillary-gravity waves. Annu Rev Fluid Mech 31:301–346
Dold JW (1992) An efficient surface-integral algorithm applied to unsteady gravity waves. J Comput Phys 193:90–115
Dold JW, Peregrine DH, (1986) Water wave modulation. In: Proc 20th Int Conf Coast Eng, ASCE, Taipei 1:163–175
Dommermuth D, Yue DKP (1987) A high-order spectral method for the study of nonlinear gravity waves. J Fluid Mech 184:267–288
Drazin PG, Johnson RS (1989) Solitons: an Introduction. Cambridge University Press, Cambridge
Ducrozet G, Bonnefoy F, Le Touzé D, Ferrant P (2007) 3-D HOS simulations of extreme waves in open seas. Nat Hazards Earth Syst Sci 7:109–122

Duin CA van (1999) The effect of non-uniformity of modulated wavepackets on the mechanism of Benjamin – Feir instability. J Fluid Mech 399:237–249
Dyachenko AI, Zakharov VE (2005) Modulation instability of stokes wave –> freak wave. J Exp Theor Phys Lett 81:255–259
Dysthe K, Krogstad HE, Müller P (2008) Oceanic rogue waves. Annu Rev Fluid Mech 40:287–310
Dysthe KB (1979) Note on a modification to the nonlinear Schrödinger equation for application to deep water waves. Proc Roy Soc London A 369:105–114
Dysthe KB, Trulsen K (1999) Note on breather type solutions of the NLS as a model for freak-waves. Physica Scripta T82:48–52
Dysthe KB, Trulsen K, Krogstad HE, Socquet-Juglard H (2003) Evolution of a narrow-band spectrum of random surface gravity waves. J Fluid Mech 478:1–10
Engelbrecht JK, Fridman VE, Pelinovski EN (1988) Nonlinear evolution equations. Jeffrey A (ed). Longman, London
Fochesato C, Grilli S, Dias F (2007) Numerical modeling of extreme rogue waves generated by directional energy focusing. Wave Motion 44:395–416
Francius M, Kharif C (2006) Three-dimensional instabilities of periodic gravity waves in shallow water. J Fluid Mech 561:417–437
Fructus D, Kharif C, Francius M, Kristiansen Ø, Clamond D, Grue J (2005) Dynamics of crescent water wave patterns. J Fluid Mech 537:155–186
Gibson RS, Swan C, Tromans PS (2007) Fully nonlinear statistics of wave crest elevation calculated using a spectral response surface method: Application to unidirectional sea states. J Phys Oceanogr 37:3–15
Gramstad O, Trulsen K (2007) Influence of crest and group length on the occurrence of freak waves. J Fluid Mech 582:463–472
Grue J, Jensen A (2006) Experimental velocities and accelerations in very steep wave events in deep water. Eur J Mech B/Fluids 25:554–564
Hasimoto H, Ono H (1972) Nonlinear modulation of gravity waves. J Phys Soc Japan 33:805–811
Haver S (2005) Freak waves: a suggested definition and possible consequences for marine structures. In: Olagnon M, Prevosto M (eds) Rogue Waves 2004, Ifremer, France
Henderson KL, Peregrine DH, Dold JW (1999) Unsteady water wave modulations: Fully nonlinear solutions and comparison with the nonlinear Schrödinger equation. Wave Motion 29:341–361
Ioualalen M, Kharif C (1994) On the subharmonic instabilities of steady three-dimensional deep water waves. J Fluid Mech 262:265–291
Islas AL, Schober CM (2005) Predicting rogue waves in random oceanic sea states. Phys Fluids 17:031701-1–4
Janssen PAEM (2003) Nonlinear four-wave interactions and freak waves. J Phys Oceanogr 33:863–884
Jeffreys H (1925) On the formation of wave by wind. Proc Roy Soc A 107:189–206
Jensen A, Sveen JK, Grue J, Richon JB, Gray C (2001) Accelerations in water waves by extended particle image velocimetry. Exp in Fluids 30:500–510
Johannessen TB, Swan C (2001) A laboratory study of the focusing of transient and directionally spread surface water waves. Proc Roy Soc Lond A 457:971–1006
Johnson RS (1977) On the modulation of water waves in the neighbourhood of kh $\approx$ 1.363. Proc Roy Soc Lond A 357:131–141
Johnson RS (1997) A modern introduction to the mathematical theory of water waves. Cambridge Univ Press
Kakutani T, Michihiro K (1983) Marginal state of modulational instability – Note on Benjamin – Feir instability. J Phys Soc Japan 52:4129–4137
Kaup DJ, Malomed BA (1995) Variational principle for the Zakharov-Shabat equations. Phys D 84:319–328
Kawata T, Inoue H (1978) Inverse scattering method for the nonlinear evolution equations under nonvanishing conditions. J Phys Soc Japan 44:1722–1729
Kharif C, Ramamonjiarisoa A (1988) Deep water gravity waves instabilities at large steepness. Phys Fluids 31:1286–1288

Kharif C, Pelinovsky E, Talipova T, Slunyaev A (2001) Focusing of nonlinear wave groups in deep water. J Exp Theor Phys Lett 73:170–175
Kharif C, Pelinovsky E (2006) Freak waves phenomenon: physical mechanisms and modelling. In: Grue J, Trulsen K (eds) Waves in geophysical fluids: Tsunamis, Rogue waves, Internal waves and Internal tides. CISM Courses and Lectures No. 489. Springer Wein, New York
Kharif C, Giovanangeli JP, Touboul J et al (2008) Influence of wind on extreme wave events: experimental and numerical approaches. J Fluid Mech 594:209–247
Kimmoun O, Branger H, Kharif C (1999) On short-crested waves: experimental and analytical investigations. Eur J Mech B/Fluids 18:889–930
Krasitskii VP (1994) On reduced equations in the Hamiltonian theory of weakly nonlinear surface waves. J Fluid Mech 272:1–30
Krein MG (1955) Foundations of the theory of λ-zones of stability of a canonical system of linear differential equations with periodic coefficients. Am Math Soc Trans Ser 2 120:1–70
Kristiansen Ø, Fructus D, Clamond D, Grue J (2005) Simulations of crescent water wave patterns on finite depth. Phys Fluids 17:064101-1–15
Kusuba T, Mitsuyasu M (1986) Nonlinear instability and evolution of steep water waves under wind action. Rep Res Inst Appl Mech Kyushu Univ 33:33–64
Kuznetsov EA (1977) To the question of solitons in parametrically unstable plasma. Dokl USSR 236:575–577. (In Russian)
Landau LD, Lifshitz EM (1980) Course of theoretical physics. Volume 3: Quantum mechanics (non-relativistic theory). Pergamon Press Ltd, Hungary
Li JC, Hui WH, Donelan MA (1987) Effects of velocity shear on the stability of surface deep water wave trains. In: Nonlinear Water Waves (IUTAM Symp). Springer Verlag, Heidelberg, 213–220
Lighthill MJ (1965) Contributions to the theory of waves in nonlinear dispersive systems. J Inst Math Appl 1:269–306
Liu PC, MacHutchon KR (2006) Are there different kinds of rogue waves? In Proc 25th Int Conf OMAE 2006, Hamburg, Germany, 2006, OMAE2006-92619:1-6
Longuet-Higgins M (1978a) The instabilities of gravity waves of finite amplitude in deep water. I. Superharmonics. Proc Roy Soc Lond Ser A 360:471–488
Longuet-Higgins M (1978b) The instabilities of gravity waves of finite amplitude in deep water. II. Subharmonics. Proc Roy Soc Lond Ser A 360:489–505
Longuet-Higgins MS (1985) Bifurcation in gravity waves. J Fluid Mech 151:457–475
Longuet-Higgins MS, Stewart RW (1960) Changes in the form of short gravity waves on long waves and tidal currents. J Fluid Mech 8:565–583
Ma Y-Ch (1979) The perturbed plane-wave solutions of the cubic Schrödinger equation. Stud Appl Math 60:43–58
MacKay RS, Saffman PG (1986) Stability of water waves. Proc Roy Soc Lond A 406:115–125
Massel SR (1996) Ocean surface waves: their physics and prediction. World Scientific Publishing Co Pte Ltd, Singapore
McLean JW (1982a) Instabilities of finite amplitude water waves. J Fluid Mech 114:315–330
McLean JW (1982b) Instabilities of finite-amplitude gravity waves on water of finite depth. J Fluid Mech 114:331–341
McLean JW, Ma YC, Martin DU et al (1981) Three-dimensional instability of finite-amplitude water waves. Phys Rev Lett 46:817–820
Melville WK, Romero L, Kleiss JM (2005) Extreme wave events in the Gulf of Tehuantepec. In: Proc. 14th Aha Huliko'a Winter Workshop, Honolulu, Hawaii, 2005
Melville WK (1982) The instability and breaking of deep-water waves. J Fluid Mech 115:165–185
Mori N, Liu PC, Yasuda T (2002) Analysis of freak wave measurements in the Sea of Japan. Ocean Eng 29:1399–1414
Mori N (2004) Occurrence probability of a freak wave in a nonlinear wave field. Ocean Eng 31:165–175
Mori N, Janssen PAEM (2006a) Freak wave prediction from directional spectra. In: Proc 30th Int Conf Coast Eng, ASCE, pp 714–725

Mori N, Janssen PAEM (2006b) On kurtosis and occurrence probability of freak waves. J Phys Oceanogr 36:1471–1483
Nakamura A, Hirota R (1985) A new example of explode-decay solitary waves in one dimension. J Phys Soc Japan 54:491–499
Newell AC (1981) Solitons in mathematics and physics. Univ Arizona: Soc Ind Appl Math
Novikov S, Manakov SV, Pitaevskii LP, Zakharov VE (1984) Theory of Solitons: the Inverse Scattering Method. Consult Bureau, New York
Olagnon M, Magnusson AK (2004) Sensitivity study of sea state parameters in correlation to extreme wave occurrences. In: Proc. 14th Int Offshore and Polar Eng Conf ISOPE, Toulon, France, 2004, pp 18–25
Olagnon M, Magnusson AK (2005) Spectral parameters to characterize the risk of rogue waves occurrence in a sea state. In: Olagnon M, Prevosto M (eds) Rogue Waves 2004, Ifremer, France
Olagnon M, Prevosto M (2005) Are rogue waves beyond conventional predictions? In: Olagnon M, Prevosto M (eds) Rogue Waves 2004, Ifremer, France
Onorato M, Osborne AR, Serio M (2002) Extreme wave events in directional, random oceanic sea states. Phys Fluids 14:L25–28
Onorato M, Osborne AR, Serio M, Bertone S (2001) Freak waves in random oceanic sea states. Phys Rev Lett 86:5831–5834
Onorato M, Osborne AR, Serio M, Cavaleri L (2005) Modulational instability and non-Gaussian statistics in experimental random water-wave trains. Phys Fluids 17:078101-1–4
Onorato M, Osborne AR, Serio M et al (2004) Observation of strongly non-Gaussian statistics for random sea surface gravity waves in wave flume experiments. Phys Rev E 70:067302-1–4
Onorato M, Osborne AR, Serio M (2006a) Modulational instability in crossing sea states: A possible mechanism for the formation of freak waves. Phys Rev Lett 96: 014503-1–4
Onorato M, Osborne AR, Serio M et al (2006b) Extreme waves, modulational instability and second order theory: wave flume experiments on irregular waves. Eur J Mech B / Fluids 25:586–601
Osborne AR, Onorato M, Serio M (2000) The nonlinear dynamics of rogue waves and holes in deep water gravity wave trains. Phys Lett A 275:386–393
Osborne AR, Onorato M, Serio M (2005) Nonlinear Fourier analysis of deep-water, random surface waves: Theoretical formulation and experimental observations of rogue waves. In: Proc 14th Aha Huliko'a Winter Workshop, Honolulu, Hawaii, 2005
Osborne AR, Petti M (1994) Laboratory-generated, shallow-water surface waves: Analysis using the periodic, inverse scattering transform. Phys Fluids 6:1727–1744
Paprota M, Przewlócki J, Sulisz W, Swerpel BE (2003) Extreme waves and wave events in the Baltic Sea. In: Rogue Waves: Forecast and Impact on Marine Structures. GKSS Research Center, Geesthacht, Germany
Pelinovsky EN, Slunyaev AV, Talipova TG, Kharif C (2003) Nonlinear parabolic equation and extreme waves on the sea surface. Radiophysics and Quantum Electronics 46:451–463
Peregrine DH (1983) Water waves, nonlinear Schrödinger equations and their solutions. J Austral Math Soc Ser B 25:16–43
Pinho de UF, Liu PC, Ribeiro CEP (2004) Freak waves at Campos Basin, Brazil. Geofizika 21:53–67
Rapp RJ, Melville WK (1990) Laboratory measurements of deep water breaking waves. Phil Trans Roy Soc Lond A 331:735–800
Rosenthal W (2005) Results of the MAXWAVE project. In: Proc. 14th Aha Huliko'a Winter Workshop, Honolulu, Hawaii, 2005. http://www.soest.hawaii.edu/PubServices/2005pdfs/Rosenthal.pdf. Accessed 14 March 2008
Roskes GJ (1976) Some nonlinear multiphase interactions. Stud Appl Math 55:231–238
Ruban VP (2007) Nonlinear stage of the Benjamin–Feir instability: three-dimensional coherent structures and rogue waves. Phys Rev Lett 99:044502-1–4
Satsuma J, Yajima N (1974) Initial value problems of one-dimensional self-modulation of nonlinear waves in dispersive media. Suppl Progr Theor Phys 55:284–306
Schober CM, Calini A (2008) Extreme Ocean Waves Rogue waves in higher order nonlinear Schrödinger models. In: Pelinovsky E, Kharif C (eds) Springer

Scott N, Hara T, Hwang PA, Walsh EJ (2005) Directionality and crest length statistics of steep waves in open ocean waters. J Atmos Ocean Tech 22:272–281

Sedletsky Yu (2006) A new type of modulation instability of Stokes waves in the framework of an extended NSE system with mean flow. J Phys A: Math Gen 39:L529–L537

Sedletsky YuV (2003) The fourth-order nonlinear Schrödinger equation for the envelope of Stokes waves on the surface of a finite-depth fluid. J Exp Theor Phys 97:180–193

Segur H, Henderson D, Carter J et al (2005) Stabilizing the Benjamin – Feir instability. J Fluid Mech 539:229–271

Shukla PK, Kourakis I, Eliasson B et al (2006) Instability and evolution of nonlinearly interacting water waves. Phys Rev Lett 97:094501-1–4

Skandrani C, Kharif C, Poitevin J (1996) Nonlinear evolution of water surface waves: The frequency down-shift phenomenon. Contemp Math 200:157–171

Slunyaev A, Kharif C, Pelinovsky E, Talipova T (2002) Nonlinear wave focusing on water of finite depth. Phys D 173:77–96

Slunyaev A (2006) Nonlinear analysis and simulations of measured freak wave time series. Eur J Mech B / Fluids 25:621–635

Slunyaev A, Pelinovsky E, Guedes Soares C (2005) Modeling freak waves from the North Sea. Appl Ocean Res 27:12–22

Slunyaev AV (2001) The initial problem for the modified Korteweg – de Vries equation on a pedestal: birth of solitons and breathers. Proc Ac Eng Sc Russ Fed 2:166–175. (In Russian)

Slunyaev AV (2005) A high-order nonlinear envelope equation for gravity waves in finite-depth water. J Exp Theor Phys 101:926–941

Socquet-Juglard H, Dysthe KB, Trulsen K, Krogstad HE, Liu J (2005) Probability distributions of surface gravity waves during spectral changes. J Fluid Mech 542:195–216

Stansell P (2004) Distributions of freak wave heights measured in the North Sea. Appl Ocean Res 26:35–48

Stiassnie M (1984) Note on the modified nonlinear Schrödinger equation for deep water waves. Wave Motion 6:431–433

Stiassnie M, Shemer L (1984) On medications of the Zakharov equation for surface gravity waves. J Fluid Mech 143:47–67

Su MY (1982) Three-dimensional deep-water waves. Part 1. Experimental measurement of skew and symmetric wave patterns. J Fluid Mech 124:73–108

Su MY, Bergin M, Marler P, Myrick R (1982) Experiments on nonlinear instabilities and evolution of steep gravity-wave trains. J Fluid Mech 124:45–72

Tajiri M, Watanabe Y (1998) Breather solutions to the focusing nonlinear Schrödinger equation, Phys Rev E 57:3510–3519

Tanaka M (2007) Numerical study on the occurrence probability of freak waves in two- and three-dimensional quasi-stationary wave fields. Electronic Preprint.

Tayfun M (1980) Narrow–band nonlinear sea waves. J Geophys Res 85 C3:1548–1552

Toffoli A, Lefèvre JM, Monbaliu J, Bitner-Gregersen E (2004) Dangerous sea-states for marine operations. In: Proc. 14th Int Offshore and Polar Eng Conf ISOPE, Toulon, France, 2004, pp 85–92

Touboul J, Giovanangeli JP, Kharif C, Pelinovsky E (2006) Freak waves under the action of wind: Experiments and simulations. Eur J Mech B/Fluids 25:662–676

Touboul J, Pelinovsky E, Kharif C (2007) Nonlinear focusing wave groups on current. J Korean Soc Coastal and Ocean Eng 9:222–227

Trulsen K (2006) Weakly nonlinear and stochastic properties of ocean wave fields: application to an extreme wave event. In: Grue J, Trulsen K (eds) Waves in geophysical fluids: Tsunamis, Rogue waves, Internal waves and Internal tides. CISM Courses and Lectures No. 489. Springer Wein, New York

Trulsen K, Dysthe KB (1996) A modified nonlinear Schrödinger equation for broader bandwidth gravity waves on deep water. Wave Motion 24:281–289

Trulsen K, Kliakhandler I, Dysthe KB, Velarde MG (2000) On weakly nonlinear modulation of waves on deep water. Phys Fluids 12:2432–2437

Voronovich VV, Shrira VI, Thomas G (2008) Can bottom friction suppress 'freak wave' formation? J Fluid Mech 604:263–296

Waseda T, Tulin MP (1999) Experimental study of the stability of deepwater wave trains including wind effects. J Fluid Mech 401:55–84

West BJ, Brueckner KA, Janda RS et al (1987) A new numerical method for surface hydrodynamics. J Geophys Res 92:11803–11824

Whitham GB (1967) Variational methods and applications to water waves. Proc Roy Soc Lond A 229:6–25

Wu CH, Yao A (2004) Laboratory measurements of limiting freak waves on currents. J Geophys Res 109:C12002-1–18

Yasuda T, Mori N (1997) Roles of sideband instability and mode coupling in forming a water-wave chaos. Wave Motion 26:163–185

Zabusky NJ, Kruskal MD (1965) Interaction of solutions in a collisionless plasma and recurrence of initial states. Phys Rev Lett 15:240–243

Zakharov V (1968) Stability of periodic waves of finite amplitude on a surface of deep fluid. J Appl Mech Tech Phys 2:190–194

Zakharov VE, Dias F, Pushkarov AN (2006a) One-dimensional wave turbulence. Phys Rep 398:1–65

Zakharov VE, Dyachenko AI, Prokofiev AO (2006b) Freak waves as nonlinear stage of Stokes wave modulation instability. Eur J Mech B / Fluids 25:677–692

Zakharov VE, Shabat AB (1972) Exact theory of two-dimensional self-focussing and one-dimensional self-modulation of waves in nonlinear media. Sov Phys J Exp Theor Phys 34:62–69